THE INFLUENCE OF MICRO-POROSITY ON DRAINAGE RELATIVE PERMEABILITY USING DIGITAL CORE ANALYSIS

by
SAEID NOROUZI APOURVARI
Msc. Reservoir Engineering
Bsc. Production Engineering

A thesis submitted in fulfilment
of the requirements for the degree of
Doctor of Philosophy
in
Petroleum Engineering

School of Petroleum Engineering
The University of New South Wales
2015

PUBLICATIONS AND PRESENTATIONS ARISING FROM THIS THESIS

[1] Saeid Norouzi Apourvari and Christoph H. Arns; An assessment of the influence of micro-porosity for effective permeability using local flux analysis on tomographic images, submitted to *SPEJ*.

[2] Saeid Norouzi Apourvari and Christoph H. Arns; The effect of microporosity on relative permeability: an image-based numerical approach, to be submitted to *Advances in Water Resources* .

[3] Saeid Norouzi Apourvari and Christoph H. Arns; Multi-scale numerical method for image-based permeability computation, *Future Energy Conference*, Sydney, Australia, 3-5 November 2014.

[4] Saeid Norouzi Apourvari and Christoph H. Arns; An assessment of the influence of micro-porosity for effective permeability using local flux analysis on tomographic images, *7th International Petroleum Technology Conference*, Doha, Qatar, January 2014, IPTC-17443.

[5] Saeid Norouzi A. and C. H. Arns; Micro-porosity contribution to permeability in dual-scale porous media from tomographic images, *5th International Conference on Porous Media*, Prague, May 2013.

[6] Saeid Norouzi A. and C. H. Arns; Multiscale permeability calculation using macroscopic lattice Boltzmann method, poster presentation, Digital Core Consortium, Canberra, Australia, November 2013.

[7] Saeid Norouzi A. and C. H. Arns; Brinkman approach to multi-scale permeability calculation, poster presentation, Digital Core Consortium, Canberra, Australia, November 2012.

ABSTRACT

High resolution images acquired from X-ray micro-tomography provide 3D pore geometry on which flow and transport properties can be computed. However, these images exhibit limited resolution in particular if field of view needs to be optimised at the same time. Constrained by the image resolution, the pore space is partitioned into macro-pores (resolvable porosity) and micro-pores, which are below the image resolution. The importance of micro-pores in fluid flow and solute transport has often been ignored. In this study, we quantify and couple the effect of sub-resolution pores into larger pores for different porous media with varying amount of micro- to macro-porosity. Both single phase and two-phase flow is considered.

Gaussian random fields (GRF) and particle based models are combined to generate heterogeneous model structures. The effect of micro-porosity on fluid flow is first examined through a critical length analysis and then confirmed using a flux analysis technique on the fully resolved pore space. Unified Brinkman equation is then solved to facilitate the coupling of Stokes and Darcy equations in the macro-phase and homogenised micro-phase.

For single phase flow in 3D model structures, the results highlight the significance of micro-pores on the fluid flow especially when macro-pores are just above the percolation threshold. The agreement between fine solution and upscaled solution, in which micro-porous region is homogenised and coupled with macro-pores, is excellent. For two-phase flow simulations, a pore morphology based approach is implemented to simulate the drainage process and to obtain fluid distributions. While the effect of micro-porosity on the effective permeability of the wetting phase is more evident at lower saturations, the error associated with its exclusion is still significant at high wetting phase saturations. The results also prove that the proposed upscaling approach is superior compared to upscaling through the Laplace equation.

Apart from the application for carbonates, which are well-known for their micro-porosity signatures, the approach proposed here might be applicable for image-based computation of permeability in unconventional reservoir rocks where multiple length scales coexist.

ACKNOWLEDGEMENTS

This study was undertaken at the School of Petroleum Engineering, the University of New South Wales (UNSW), Sydney, Australia. I am indebted to all staff and faculty members for having provided a stimulating working environment.

Foremost, I would like to express my sincere gratitude to my supervisor, Prof. Christoph H. Arns, for his continuous support of my research, for his patience, motivation, enthusiasm, and immense knowledge. I could not have imagined having a better advisor and mentor for my PhD study.

During the course of my PhD, I had opportunities to meet and contact many wonderful people and discuss my research questions with them including Martin J. Blunt, Jacob Bear, W. Brent Lindquist, Dorthe Wildenschild, P. M. Adler, Maša Prodanović and many more who I met them at the Interpore conference in Prague. My sincere thanks also goes to Timothy Senden, Adrian Sheppard, Mohammad Saadatfar, Jill Middleton and Ajay Limaye at the Australian National University and Mark Knackstedt and Pal-Eric Øren at FEI Lithicon. I am also thankful to Ji-Youn Arns for putting me through the Linux, Goncalo Silva for his valuable comments on lattice Boltzmann methods and Stuart D. C. Walsh for his help on grey lattice Boltzmann method.

I would like to acknowledge the member companies of the Digital Core Consortium for helping me to stay connected with the the oil and gas industry. National Computing Infrastructure (NCI) with its helpful staffs is highly appreciated for generous allocation of computational time, data stoarge and support.

My sincere thanks goes to all my friends for supporting me and my family during the last four years. YOU ARE GREAT! I would also like to thank my fellow PhD students and friends at the school of petroleum engineering. Thank you for helping me!

Most importantly, I am very very thankful to my wife for her unconditional love, continous support and for all sacrifies she did. Without your help, it was not

possible for me to do it. Thanks for everything Raziyeh. I would also like to thank my family back in Iran, my parents who are my angels and my true role models, my siblings and their family who always inspired me and my parents and my siblings in-law who always supported me. YOU ARE AWSOME!

DEDICATION

I wish to dedicate this work
to my parents and my wife;
for their guidance, support,
and unconditional love,
and to my beloved son, Sina.

CONTENTS

TABLES

Table

FIGURES

Figure

CHAPTER 1

INTRODUCTION

Fluid flow in porous media at various spatial and temporal scales is of great interest among different disciplines such as petroleum, civil and environmental engineering. Ground water remediation and nuclear waste disposal in civil and environmental engineering are two examples, which are very sensitive to the precise understanding of multiphase flow. In petroleum engineering, having a sound understanding of fluid flow will result in a more accurate estimation of recovery as a major parameter in reservoir management and development.

It is generally accepted that the era of "easy oil" is finished. Giant conventional oil and gas fields are mature now and new discovered green fields no longer meet the energy demands required of them. This requires us to improve our understanding of the processes involved in extracting the remaining hydrocarbons. On the other hand, unconventional resources such as shale gas and coal seam gas, are becoming more important; however, the cost and the technology associated with them is higher compared to those in conventional reservoirs. In both cases, implementing state of the art EOR/IOR techniques in mature field or relying on unconventional resources to meet the world's energy demand in the near future, we need to enhance our notion about reservoir characterisation and fluid flow in the subsurface structures.

Describing the flow of a fluid in porous media with tortuous and complicated pore geometry is not straightforward. The difficulty is twofold for multiphase flow when multiple fluids flow simultaneously in the pore space. Apart from morphological and topological properties of the pore space, the volume fraction and more importantly the distribution of all phases in the pore space affect multiphase flow processes. Heterogeneity of natural porous media makes the problem even more complicated. The existence of heterogeneities spanning over multiple length scales results in significant challenges for transforming data between different scales. Based on pore scale modeling techniques, this thesis proposes a multiscale approach and aims to combine the information of two-phase flow at two different length scales.

1.1 Pore scale imaging and modeling

Based on detailed information of the pore space geometry, pore scale models provide an excellent opportunity for studying fluid flow processes in fundamental ways. Despite the large computational effort required for characterising a realistic pore space, discrete models have many advantages. In the relatively new context of "digital core laboratory" [13, 95], they offer an important tool to compute flow and transport properties of rock samples on which conventional laboratory analysis is difficult, if not impossible, to perform. Not only can laboratory experiments be simulated numerically, the wide range of parameter choice in these models enables us to do sensitivity analysis at a lower cost for designing appropriate production scenarios.

Recent progresses in the field of imaging and visualisation techniques has spurred much attention among experimentalists as well as modellers. Methods for two dimensional representation of porous media such as scanning electron microscopy (SEM), micromodels and light transmission method (LTM) were predominantly used for years [165, 181, 131, 130]. Since connectivity of the pore space can not be captured in these 2D methods, three dimensional techniques were found to be more desirable for obtaining realistic information on physical processes in porous media. Photoluminescent volumetric imaging (PVI), laser scanning confocal microscopy (LSCM), magnetic resonance imaging (MRI) and X-ray computed tomography (CT) are some techniques which have been applied for 3D characterisation of porous media [129, 62, 206, 128]. Recently, microcomputed tomography (μ–CT) imaging, has been established as the major technique to map the microstructure of porous media in 3D. This method has been used to capture the pore space geometry and to quantify processes at the pore level including: pore space structure and connectivity [112], multiphase flow [17, 45, 193, 102], morphological properties of rocks [15] and image-based computation of petrophysical properties [14]. These days, acquiring high resolution images of porous media with resolution of a few micrometer is routine and the main challenge is to develop pore scale models to take advantage of the information contained in these images.

The dramatic advances in computational capabilities have offered us new opportunities in development of pore scale modeling tools. Generally, there are two ways to compute transport properties from 3D images: direct numerical simulation methods on the images and pore network (PN) models. In direct modeling, the voxelated image, which is already discretised into Cartesian grids, is used for flow and transport simulation. In pore network modeling, however, a topologically representative network with idealised properties is first derived from the image and

flow properties are then computed on that network. Semi-analytical computation of flow and transport through network models made them computationally attractive for the study of capillary-controlled displacement [36]. However, the number of approximations required to describe pore space geometry limits their applicability. In addition, extraction of representative networks from complex porous media is not straightforward. Direct methods include lattice Boltzmann method (LBM), smoothed particle hydrodynamics (SPH), level set, volume of fluids and density functional modeling. LBM is the most popular one for computing single and multiphase flow [60, 173, 174, 116, 134]. This is a particle-based model in which fluid is represented by packets of particles distributed on computational grids. In each time step, particles are streamed and collided and the average of their distribution function translates into macroscopic properties. It has been shown that LBM could approximate the governing Navier-Stokes equations [43].

The fundamental approach in this thesis considers X-ray microtomography as a pore scale imaging technique and LBM as a direct numerical simulation method for pore scale modeling. The next section provides a detailed description of the problems and difficulties associated with each of these techniques and the approach followed in the thesis to address these problems.

1.2 Problem statement

High resolution images acquired from X-ray micro-tomography provide us with 3D pore geometry on which petrophysical and morphological properties could be calculated [200, 13]. However, these images exhibit a limited resolution; particularly if the field of view needs to be optimised at the same time. X-ray source focal-spot size, magnification and imaging system performance are the main factors controlling the system resolution [37]. Constrained by the system resolution, pore space is partitioned into macropores (resolvable pores), and micropores which are smaller than the resolution of the image. While a resolution of a few micrometers could resolve the whole pore space of some sandstones and carbonates, many carbonates and in particular unconventional reservoir rocks, such as tight sand and shales, exhibit a huge amount of microporosity. Ignoring this fraction of pore space could introduce significant errors to resultant transport properties computed on the images of these types of rocks [36].

Fig. 1.1 shows an analysis carried out on an image of a carbonate rock to elaborate more on this issue. In this case, the voxel size is 4.5 μm and at this resolution, the microporosity analysis performed on 3-phase segmented image (Fig. 1.1a) [147] reveals that of 28% total porosity, macroporosity is 12% whereas micro-

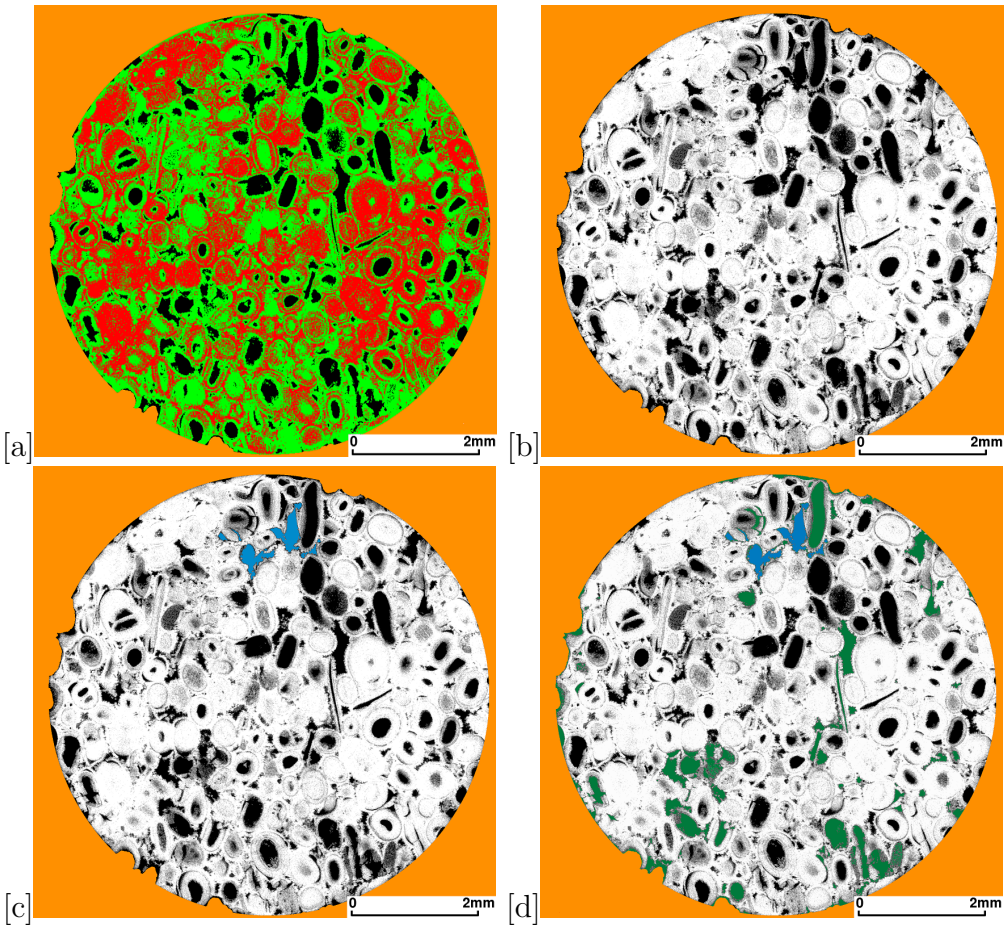

Figure 1.1: Processed image of a Savonnier carbonate: [a] 3-phase segmentation; macropore is in black, solid phase is in red and light green is the intermediate phase. [b] Microporosity analysis; macropore (black), micropore (grey) and solid (white); [c] colour mapping of the connected macropres (blue) via connected cluster of macropores; [d] colour mapping of the micro-connected macropores (green).

porosity is 16% (Fig. 1.1b). Macropores are shown in black, solid is in white and the microporosity is shown in grey. Microporosity comprises more than 50% of the total porosity. More interestingly, based on connectivity analysis (Fig. 1.2) [147], only 8% of macropores are connected via connected clusters of macropores while including the upper quartile of the microporous voxels will increase the connectivity of macropores to 60% . The colour mapping of the resultant connectivity analysis is shown in Fig. 1.1c and Fig. 1.1d. These figures clearly highlight the potential significance of microporosity incorporation in enhancing the interconnectivity of the pores and consequently the calculation of the effective flow properties.

Carbonates are characterised as rocks with varying amount of microporosity, ranging from less than 10% to more than 50% of the total porosity [94]. So, it is worth investigating the effect of microporosity on permeability as a macroscopic flow property. Although some efforts have been made to relate pore types and inter-

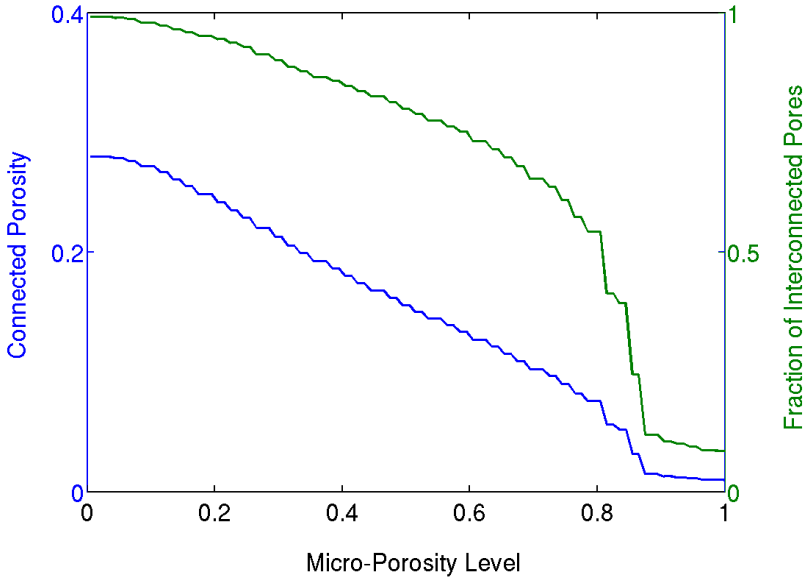

Figure 1.2: Connectivity analysis performed on Savvonier carbonate. The X-axis shows the microporosity level in which 1 and 0 corresponds to macropore and solid phase, respectively. (A voxel with microporosity level of 0.8, for instance, corresponds to a voxel with 80% porosity.)

connectivity to petrophysical and multiphase flow properties [98, 13], quantifying microporosity signatures and their effect on absolute and relative permeability is still an open question. The importance of microporosity on fluid flow has been acknowledged in early works on image data [194] and also in the most recent studies [36, 96], but mostly qualitatively. While quantitative analysis of the significance of microporosity on the single and two phase flow properties has recently been done in multiple research groups [81, 124, 145], it is worth more research.

While quantifying the role of micropores on the average behavior of fluid flow is not straightforward, the bigger challenge is the integration of micropores and macropores. Coupling pores at different length scales requires a numerical scheme which integrates this information, but remains computationally practical. This defines the common problem of upscaling which has been addressed in reservoir engineering for transforming data from core scale to the reservoir scale, but rarely for pore scale to core scale. Multiscale approaches, such as coupled Darcy-Stokes method [6, 7, 77] and Brinkman-Stokes method [70, 143, 150, 164], have recently been used for modeling fluid flow through heterogeneous reservoirs where multiple length scales coexist. In these methods, the Darcy equation in the porous matrix region is coupled with the Stokes equation in fractures. In contrast to these reservoir scale studies, here we focus on the pore scale fluid flow in very heterogeneous porous media.

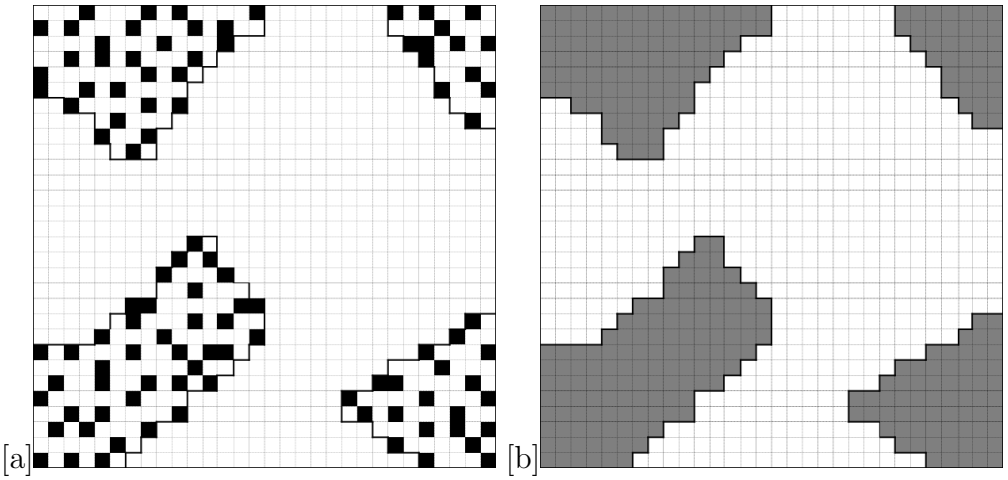

Figure 1.3: A conceptual model of a pore space at two different resolutions: [a] High resolution in which an explicit representation of all pores and solid pixels is shown. [b] Low resolution which depicts microporous region in grey pixels and macropores in white.

By implementing dual-scale network models, some researchers proposed models which include both macro- and micropore networks [22, 26, 80, 122, 125, 81]. Macropore network constructed based on resolved pores is coupled to the network of sub-resolution pores. Although promising, dual scale network models suffer from the same limitations as conventional network models do.

Here, a multiscale numerical approach is proposed in which the Darcy equation is coupled with Stokes equation via the lattice Boltzmann method. Microporous region is assumed homogeneous and Darcy equation holds, while macropores are treated as free-flow region where Stokes equation is valid. Computational simplicity, easy handling of irregular boundary conditions, capability to simulating complex fluid flow and its parallel computing [185] have made LBM as a suitable choice for pore scale modeling. However, making use of all these advantages of LBM in simulating fluid flow requires a detailed representation of porous media where pore and solid phases are explicitly resolved; a condition which may not be satisfied at least for some pixels/voxels in some rocks. Through a conceptual model, Fig. 1.3 highlights this problem by showing a model at two different resolutions. At high resolution (Fig. 1.3a) all pores are resolved whereas decreasing the resolution make the pores within the microporous region unresolved (Fig. 1.3b). This thesis aims to address this problem by developing LBM models which are capable of handling not only fluid and solid nodes but also grey nodes, where grey nodes correspond to microporosity in this context.

1.3 Thesis objectives

The general objective of this thesis is to improve our understanding of fluid flow in heterogeneous porous media. From many useful pore scale modeling techniques, this study focuses on LBM and in particular Macroscopic Lattice Boltzmann Method (MLBM) [64, 83, 115, 182] for upscaling relative permeability curves from the pore scale.

This dissertation seeks to address the following questions: (1) what is the merit of pore scale modeling and image-based fluid flow simulation, (2) how significant is the effect of microporosity on the effective permeability for single phase and two-phase flow systems, (3) how to couple the effect of micropores with an explicit representation of macropores, and (4) could LBM be used for transforming data between different scales. To answer these questions, the following specific research objectives are pursued:

- to build dual-scale porous media with combinations of Gaussian Random Field (GRF) and Boolean models,
- to quantify the effect of microporosity on the effective permeability using a characteristic length scale and through permeability calculations using LBM.
- to develop a MLBM code for coupling an average effect of micropores with macropores,
- to implement a pore-morphology-based approach for numerically simulating drainage process and partially saturating the model structures,
- to implement MLBM for upscaling wetting phase relative permeability curves.

1.4 Organisation of the thesis

This thesis is organised in six chapters including this chapter. The next chapter describes 3D structures, which are used for numerical experiments in this thesis. Both experimental imaging and numerical simulation of porous media are considered. For the experimental part, high resolution X-ray micro-CT images acquired in the CT lab at the Australian National University (ANU) are used. Using parallel image processing software, these tomographic images are segmented before being used for fluid flow simulations. For simulated porous media, a range of model structures including particle (Boolean) models, Gaussian random structures and combinations

of both is used. While pure particle models are used for simulating homogeneous porous media, the combination of Gaussian random models and Boolean models are implemented for generating more heterogeneous model structures.

Chapter 3 includes single phase flow simulations and quantification of the effect of microporosity on the fluid flow. Lattice Boltzmann method (LBM), as a robust pore scale modeling technique, is explained and used for simulating fluid flow in heterogeneous model structures. The significance of microporosity on the effective permeability is shown through permeability calculations on 2D heterogeneous model structures. For 3D model structures, this effect is first shown using the concept of characteristic length, as a good estimator of permeability, and then confirmed by applying a flux tracking technique.

Chapter 4 extends the methodology presented in chapter 3 to two phase flow simulation. The most important part in two phase flow simulation is the saturation distribution; the way that multiple fluids are distributed in the pore space. We use capillary drainage transform for simulating the drainage process in the porous media by which a non-wetting phase displaces a wetting phase. The simulations are carried out on more than hundred simulated model structures. Similar to single phase flow in 3D structures, characteristic length is used to examine the significance of wetting phase in micropores, before calculating permeability on some selected porous media.

Chapter 5 includes the upscaling scenarios for single phase and two-phase flow systems. While LBM is used as a "true solution" in which both micropores and macropores are resolved, MLBM is proposed for coupling an average effect of micropores with an explicit representation of macropores. The amount of momentum reduction in microporous region is controlled by a momentum sink parameter, which is a function of permeability of that region and the fluid viscosity. For upscaling single phase flow, the permeability calculated on pure micropore models is used to compute the momentum sink parameter assigned to microporous regions of dual scale porous media. For two-phase flow, $k_{rw} - S_w$ relationship calculated on pure micropore model is used to calculate the effective permeability of wetting phase at each saturation and its corresponding momentum sink parameter. In addition, the capability of the Laplace equation for upscaling the effective permeability of the wetting phase is also examined. The results are compared with those obtained from MLBM.

Chapter 6 concludes this thesis and presents some recommendations for further investigation.

1.5 Programming issues

We use lattice Boltzmann method for simulating fluid flow on the pore space of segmented images. All 2D and 3D LB simulations are written in Fortran 90. Two-dimensional simulations are based on single-CPU programs and are run on a Z600 HP workstation with 2 Quad Core processors and 16 gigabytes (GB) of RAM.

Due to the high computational demand of the LBM, implementing it on representative sample volume and in 3D requires parallel computing for achieving appropriate computing times and for fulfilling the memory requirements. An in-house, parallel and single phase LBM code is first used for LBM simulations and later is modified for MLBM simulations. It applies Message Passing Interface (MPI) standard library for parallelisation. All 3D simulations are run on the Raijin supercomputer, located at the Australian National University (ANU) in Canberra. It has 57472 cores (Intel Xeon Sandy Bridge Technology, 2.6 GHz) in 3592 computer nodes and approximately 160 terabytes (TB) of main memory.

Matlab and Drishti [110] are the main tools for presenting, analysing and visualising the simulation results.

CHAPTER 2

EXPERIMENTAL AND SIMULATED POROUS MEDIA

An accurate characterisation of pore morphology and topology is a keystone to every pore scale modeling technique. The geometrical properties of a porous medium, i.e. the shape, size, the volume of pores and the way that they are connected to each other, affect its macroscopic properties. Classifying the porous media as biological, geological and artificial [1], the level of complexity in describing the pore geometry of these materials is different. In general, the description of artificial porous media is straightforward, while it is often much more complicated for geological and biological ones.

Biological porous media including bones, tissues and membranes have been the subject of recent studies in the field of medicine [89], but are out of the scope of this thesis. Geological porous media including, e.g. sandstone and carbonate are of great interest to petroleum engineers. These are the dominant rock types in hydrocarbon reservoirs. Compared to sandstone, carbonates are more heterogeneous and consequently more difficult for pore scale modeling studies. The existence of heterogeneities which span over multiple length scales and while mostly uncorrelated, make the description of pore geometry very difficult. While unimodal pore size distribution of sandstones make them ideal for image-based calculation of petrophysical properties, the bimodal or multi-modal distribution of pore size in carbonates poses many challenges. Artificial porous media and in particular sphere packs, however, are relatively simple to characterise and have been vastly used in the analytical, theoretical and numerical studies of porous media.

In this thesis we use both geological and artificial porous media for better understanding of pore scale processes. Experimental X-ray images of two relatively homogeneous sedimentary rocks constitute geological porous media. In addition, two classes of model structures and combinations of those are utilised to generate heterogeneous artificial porous media with varying micro- to macro-porosity ratios.

2.1 Experimental imaging data

Experimental description of pore morphology started from the early 1980's with serial sectioning. In this method, a dyed glue is injected into the pore space and then the sample is cut into numbers of 2D thin sections [210]. Using optical or electron microscope, the colorful photographs of these sections are then captured and digitised for further analysis. Although it is possible to obtain a 3D representation of pore geometry by reconstructing series of 2D images, it is a very difficult and tedious task [111]. A more advanced technique which is somehow equivalent to this method is the recent combination of Focused Ion Beam and Scanning Electron Microscopy (FIBSEM) for imaging material below the micron scale [68]. This technique provides images with resolution down to a few nanometer but suffers from the small field of view (FOV). Moreover, it is a destructive method.

An alternative method to characterize the internal structure of a porous medium in 3D while keeping the sample intact for further studies is nuclear magnetic resonance (NMR) imaging. This technique was first used in radiology, as a medical imaging tool, to investigate the anatomy and function of the body and has recently been implemented for describing the pore morphology and topology of geological porous media [19]. Apart from the capability of structural description, NMR has also been used for measuring flow fields in sphere packs [113] and fractured media [42, 101].

Following [61], who introduced synchrotron computed microtomography (CMT) and laboratory μ–CT to produce high resolution 3D images, X-ray microtomography has been implemented by many disciplines including civil engineering, material science and petroleum industry. In synchrotron based tomography a monochromatic beam of X-ray is generated and passed through the rock sample whereas in laboratory CMT the X-ray beam is polychromatic. Monochromatic radiation facilitates energy specific imaging with enhanced contrast of phases [200]. Polychromatic radiation, however, consists of beamlines with a range of wavelengths. Despite imaging artifacts introduced from spreading of polychromatic beam in laboratory CMT (e.g. beam hardening [200]), it has some advantages which have made it as now-standard approach to image pore space of rock samples. In laboratory CMT, no central synchrotron facilities are required. Moreover, no constraint on image capturing time results in improvement of signal to noise ratio [36].

X-ray μ-CT scanners provide high resolution 3D pore geometry on which petrophysical and morphological properties could be calculated [200, 13]. They consist of three main parts: X-ray source, a rotation stage and a detective camera (see Fig. 2.1). The X-ray generated by source is radiated towards the sample,

positioned on the rotation stage. While it passes through the specimen, X-ray beam is attenuated depending on the density of the material contained in the sample. The attenuated X-ray is then captured by a detective camera at the far end of the setup. The rotation stage could rotate the mounted sample stepwised by 360 degree while 2D image is captured at each step.

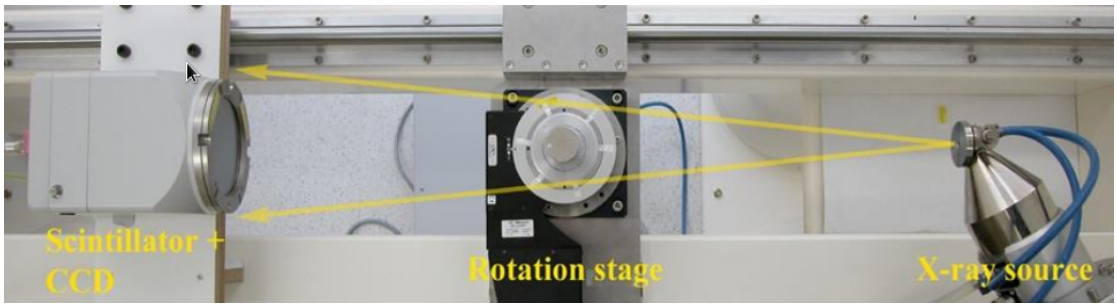

Figure 2.1: The main parts of a CT scanner (top view). The X-ray beam generated by X-ray source is passed through the sample mounted on the rotation stage and then captured by the detective device which consists of a scintillator and a charged coupled device (CCD) camera [146].

3D tomogram generated by this technology is essentially a result of reconstruction of many 2D radiographs taken from the sample at different levels and rotational angle. Each 3D tomographic image or tomogram consists of volumetric elements called voxel, which stores the X-ray attenuation of the materials contained by that voxel. The X-ray attenuation and consequently the grayness of each voxel depends on the density and composition of the imaged material. Image processing techniques need to be applied on the gray scale image to remove the noise and sharpen the boundaries before differentiating it into the constituting phases.

In this thesis we consider images of two sandstone samples, Fontainbleau sandstone and Bentheimer sandstone, acquired by laboratory μ–CT scanner at the Australian National University [163], which were the subject of a recent study on resistivity index [204].

2.1.1 Fontainebleau sandstone

Classified as a clastic sedimentary rock, Fontainebleau (FB) sandstone is considered as a benchmark for clean and homogeneous rocks in the petroleum industry containing very little clay material (less than 1.5%). A cylindrical core of FB sandstone, 4.7 mm in diameter and 4.6 mm in length was imaged using X-ray μ–CT at 3.6 μm resolution. Fig. 2.2 shows a 2D slice of 3D gray scale tomogram and also shown a slice of segmented image obtained after standard image processing steps on raw image [175]. A literature survey on studies of FB shows the scale dependency

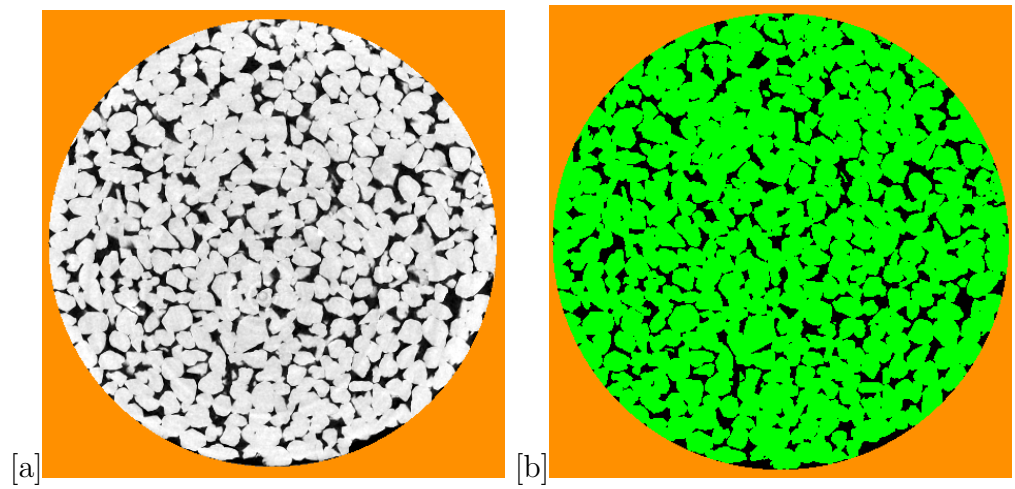

Figure 2.2: Pore scale image of FB sandstone. [a] A 2D slice of 3D tomogram after noise removal and image enhancements. [b] 2D slice of 3D segmented image in which grains are in green and pore space in in black (voxel size = 3.6 μm).

of its petrophysical properties especially permeability. [183] calculated permeability on five sub-volumes of different sizes (0.085 mm^3 – 0.59 mm^3) at a resolution of 10 μm. A large variability in the results was observed. Porosity-permeability relationship was investigated using eight sub-volumes of sizes 0.59 mm^3 at a resolution of 7.5 μm and the results showed a variation of 10% in porosity and a factor of two in permeability [17]. By estimating and minimizing several sources of errors, [10] succeeded to accurately predict transport properties from sub-volumes of FB sandstone of sizes 0.32 mm^3 at a resolution of 5.7 μm. The same sample size was later used for investigating cross-property correlations and permeability estimation of FB sandstone [9]. In addition, a two-point volume to volume correlation function calculated on the pore space of a sub-volume of FB showed that a sample of size 0.32 mm^3 can be considered representative for calculating petrophysical properties [12].

In this study, a sub-volume of 400^3 voxels, representing a volume of 2.99 mm^3 with 17% porosity was selected for validating the homogenisation of an upscaling method described in chapter 5.

2.1.2 Bentheimer sandstone

Bentheimer sandstone is also considered as a benchmark, homogeneous sedimentary rocks which contains about 1.5 % clay minerals. A 2048×2048×1828 voxels image of a cylindrical core plug with diameter 5 mm and length 5 mm was acquired at resolution 2.9 μm (see Fig. 2.3a). Due to the presence of clay in the sample, three-phase segmentation procedure was followed to differentiate the gray scale raw

[a] 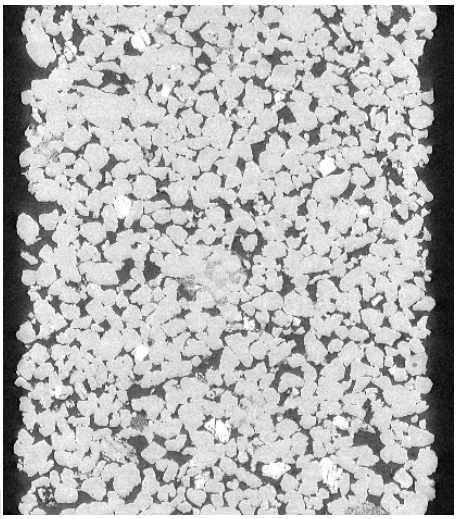 [b] 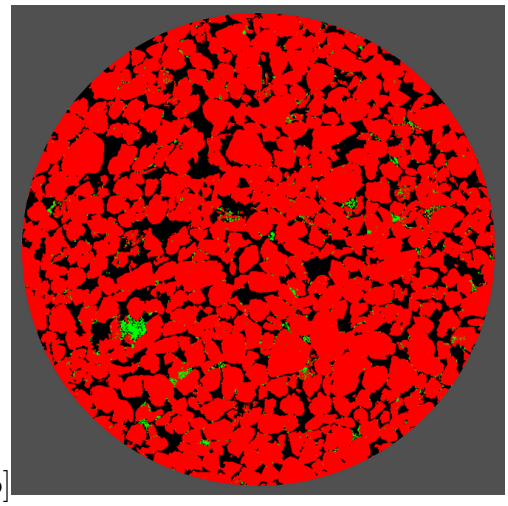

Figure 2.3: Pore scale image of Bentheimer sandstone. [a] A 2D side-view slice of 3D tomogram. [b] 2D slice of 3D image, segmented in three phases: solid is shown in red, clay in green and pore space is in black (voxel size = 2.9 μm).

image into three phases. Fig. 2.3b shows a 2D slice of the segmented image in which solid is in red, clay is in green and pore space is in black. A sub-volume of 400^3 voxels, representing a volume of 1.54 mm^3 with porosity 0.21, was selected for further investigations.

2.2 Model structures

Todays model composites are widely used for investigating the effects of microstructures on the macroscopic properties. Given a digital representation of their microstructure, many properties (e.g. permeability [2], conductivity [10, 27] and elastic moduli [15]) of model composites could be calculated. Here, we consider in particular permeability and relative permeability for multi-scale media.

Based on the densification process utilised, two basic classes of model composites and their intersections are introduced. These models form the main data base for the numerical experiments in the following chapters. The first class is generated by taking level-cuts through Gaussian random fields [15]. Structures developing from spinodal decomposition, amorphous composites and some rocks could be represented by this class. The second class, which is one of the simplest and most traceable models in stochastic geometry [184], is generated by a Poisson densification process, where particles or grains with different shapes and sizes are placed on the lattice in an independent random process [15]. Particulate models of this kind have been utilised in many cases, including ceramic powders [155], wood fiber composites [197], and sedimentary rocks [168, 118]. In addition, to make dual-scale

porosity media, which are appropriate to test the algorithms applied in this study, different combinations of Gaussian models and Boolean models are devised.

2.2.1 Gaussian models

The Gaussian models are created by level-cuts of a superposition of random plane waves [29, 188]. Although they were originally developed to describe the morphologies associated with spinodal decomposition [40], later their application extended to describe the structure of bicontinuous microemulsions [28], polymer blends [97] and foams [156]. To build a Gaussian model, first we need to generate a Gaussian random field (GRF's) and then by setting level-cuts, two-phase model composite is generated. There are two methods of generating isotropic GRF's. Each one has specific advantages. The first method develops a random field in a cube of side length T using a Fourier summation [154]:

$$y(\mathbf{r}) = \sum_{l=-N}^{N} \sum_{m=-N}^{N} \sum_{n=-N}^{N} c_{lmn} e^{i\mathbf{k}_{lmn}.\mathbf{r}} \,, \tag{2.1}$$

where $\mathbf{k}_{lmn} = (2\pi/T)(l\mathbf{i} + m\mathbf{j} + n\mathbf{k})$. Random variables $c_{lmn} = a_{lmn} + ib_{lmn}$ (a_{lmn} and b_{lmn} real) determine the statistics of the field. Requiring y to be real gives $c_{lmn} = \bar{c}_{-l,-m,-n}$ and that $\langle y \rangle = 0$, which results in $c_{000} = 0$. Discretisation requires $c_{lmn} = 0$ for $k_{lmn} = |\mathbf{k}_{lmn}| \geq 2\pi N/T$. To generate a Gaussian field the coefficients c_{lmn} are taken as random independent variables with Gaussian distributions such that $\langle a_{lmn} \rangle = \langle b_{lmn} \rangle = 0$, and $\langle a_{lmn}^2 \rangle = \langle b_{lmn}^2 \rangle = \frac{1}{2}\rho(k_{lmn})(2\pi/T)^3$. The function $\rho(k)$ is a spectral density. For a random field defined in this manner, the field-field correlation function can be written as [154]:

$$g(r) \equiv \langle y(\mathbf{r_1}) y(\mathbf{r_2}) \rangle = \int_0^\infty 4\pi k^2 \rho(k) \frac{sinkr}{kr} dk \,, \tag{2.2}$$

where $\rho(k)$ is chosen so that g(0) = 1. This definition could be evaluated by fast Fourier transform and is applicable if periodic structure is desirable [15]. However, when the spikes in the spectral density have to be resolved an alternative approach has been suggested in which random field is generated using the "random wave" form:

$$y(\mathbf{r}) = \left(\frac{2}{N}\right)^{1/2} \sum_{i=1}^{N} cos(\mathbf{k_i}\hat{\mathbf{k}}_\mathbf{i}.\mathbf{r} + \phi_\mathbf{i}) \,. \tag{2.3}$$

Here ϕ_i is a uniform deviate on [0, 2π), and $\hat{\mathbf{k}}_\mathbf{i}$ is uniformly distributed on a unit sphere. The magnitudes of the wave vectors k_i are distributed on the [0, ∞) with spectral density $\rho(k)$ related to $g(r)$ by a Fourier transform. In this case the fields

are not periodic, but N can be chosen arbitrarily large over a specified k range.The field-field correlation function employed is [120, 188]:

$$g(r) = \frac{e^{-r/\xi} - (r_c/\xi)e^{-r/r_c}}{1-(r_c/\xi)} \frac{sin2\pi r/d}{2\pi r/d} \ , \tag{2.4}$$

characterised by a correlation length ξ, domain scale d, and a cut-off scale r_c. The corresponding Fourier transform is given by:

$$\rho(k) = \frac{\pi^{-2}(\xi - r_c)^{-1}\xi^4 d^4}{[d^2 + \xi^2(kd-2\pi)^2][d^2+\xi^2(kd+2\pi)^2]} - \frac{\pi^{-2}(\xi - r_c)^{-1} r_c^4 d^4}{[d^2 + r_c^2(kd-2\pi)^2][d^2+r_c^2(kd+2\pi)^2]} \ . \tag{2.5}$$

Model composites can be defined by taking level-cuts through the same random wave at levels α and β. The regions in space where $\alpha \leq y(\mathbf{r}) \leq \beta$ is considered as phase 1, and the remaining regions [$y(\mathbf{r}) < \alpha$ and $y(\mathbf{r}) > \beta$] are defined as phase 2. This is called the "two-level cut" random field of Berk [28] which is an extension to Cahn's approach [40]. The one-level cut field is recovered by setting $\alpha = -\beta$ [151, 158, 188]. Based on the macroscopic volume fractions of the two phases, the positions of the level cuts can be found numerically by a bisection algorithm [15] on the digitised structure. The freedom in choosing the position of the level cuts (for a particular volume fraction) allows one to model a variety of microstructures [157]. Fig. 2.4 shows three correlated GRF models which have been cut once but at different levels. Cutting GRF at one level, generates two phase structure which later will be filled with different particle model.

2.2.2 Boolean models

Although relatively simple, Boolean models are flexible and often used to describe the morphology of complex materials [192]. One of the simplest examples of a Boolean model has been mentioned by [184] in which points are scattered in the plane according to a stationary Poisson process of intensity λ. A disc of fixed radius r is placed on each of these points and finally the union of these discs form a Boolean model. Identical overlapping spheres (IOS) model is another example of Boolean model which is used in theoretical and numerical analysis [191, 190]. Arns employed a range of Boolean models with different grain shapes and mixtures of grains [15]. Here, to generate bi-modal porosity medium, grain shapes of spheroids and spheres are considered.

The coordinate system of the particle $\sum_p = \{\mathcal{O}_p, \mathbf{x_p}, \mathbf{y_p}, \mathbf{z_p}\}$, a local coordinate system $\sum_l = \{\mathcal{O}_l, \mathbf{x_l}, \mathbf{y_l}, \mathbf{z_l}\}$ and the lattice coordinate system $\sum = \{\mathcal{O}, \mathbf{x}, \mathbf{y}, \mathbf{z}\}$

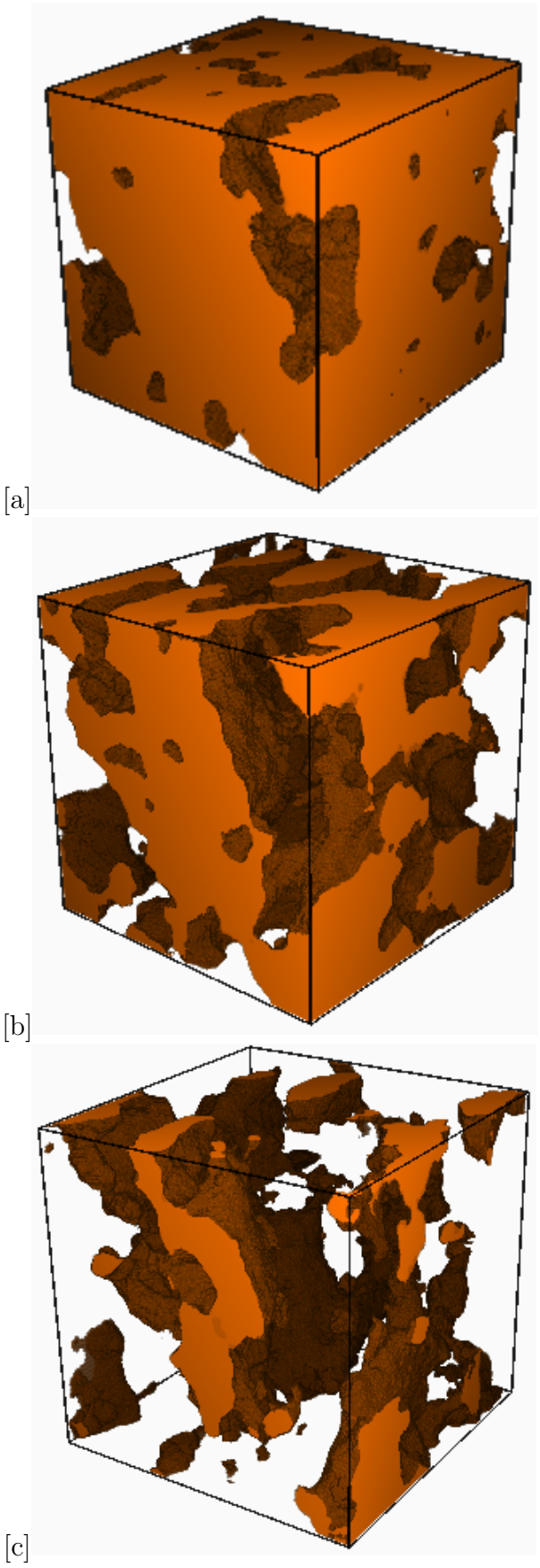

Figure 2.4: The interface of one-level cut GRF models at fraction [a] 0.2, [b] 0.5 and [c] 0.8. Models are discretised on 400^3 lattices. (Visualised by Drishti [110])

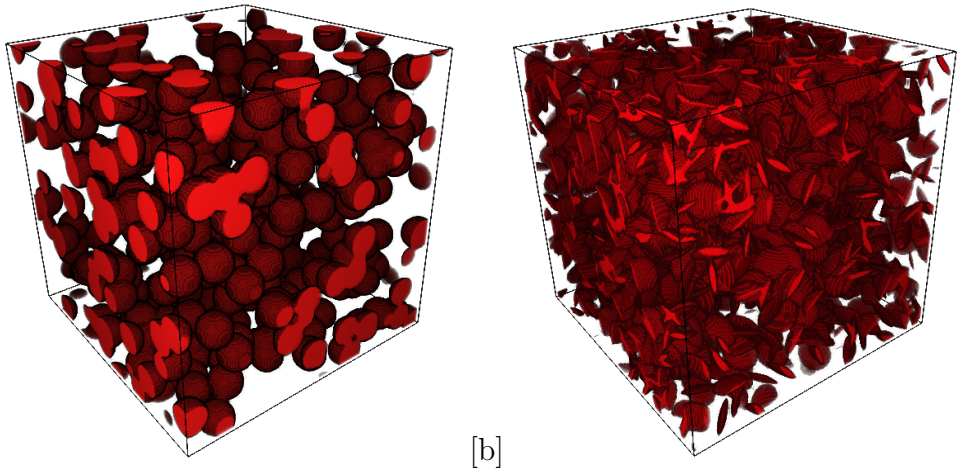

[a] [b]

Figure 2.5: The interface of Boolean models. [a] overlapping spheres of radius $r = 6$. [b] overlapping spheroids with an half-axis of $r = 4$. The volume fraction of particles phase is 0.7 and models are discretised on 200^3 lattices.

are three cartesian coordinate systems which characterize the orientation and position of grains on the lattice. The local coordinate system has the same origin as the particle coordinate system ($\mathcal{O}_p = \mathcal{O}_l$) but being rotated against $\sum_p$ by an angle α around a rotational axis $\mathbf{g}$ through the origin. Specific selections of α and $\mathbf{g}$ will result in transformation of the local coordinate system to the lattice coordinate system ($\mathbf{x_l}||\mathbf{x}$, $\mathbf{y_l}||\mathbf{y}$, $\mathbf{z_l}||\mathbf{z}$). Taking a vector of particles and characterising each particle by its size, shape, rotational freedom and probability to be placed (based on its Poisson density), complex mixtures of grains could be generated in a parallel manner. Fig. 2.5 shows an example of Boolean models with various particle shape and density.

To have a more realistic porous medium which mimics the behavior of bimodal porosity systems, we use the Gaussian random field approach to generate two distinct phases, after which each phase is filled with grains of different shapes, e.g. spheroids and spheres.

2.2.3 Dual-scale porosity models

Model structures constructed based on some statistical information of geological porous media has been implemented for understanding the physics of flow processes. However, most of these models are available for sandstones [154, 205, 132]. In carbonates, the variation of permeability over 2 to 3 orders of magnitude at fixed porosity [53] and its bimodal or multi-modal pore size distribution introduces many challenges for developing such models. By smoothing random binary images using Gaussian and Laplacian-Gaussian function, [47] succeeded to model Vicor

glass and crystalline dolomite. Structural and transport properties of these models were then calculated and an excellent agreement with experimental data was obtained. Statistical reconstruction for generating porous media with bimodal pore size distribution is another methodology which has been used by some researchers. Based on a technique developed by Adler and his co-workers [2], [126] constructed dual scale porous media for investigating macroscopic conductivity, and later single and two-phase permeabilities [127] of vugular porous media. More recently, [34] proposed a stochastic geometrical model for the diagenesis of carbonate rocks. Being a continuum model, the pore scale microstructure is represented at arbitrary resolution.

Although we do not model carbonates here, of particular interest are model composites with bimodal pore size distribution. These models form the database for investigating the effect of micro-porosity on the effective permeability. As mentioned earlier, combinations of Gaussian random fields and Boolean models are used for making model structures with varying amount of micro-to-macro porosity. First a periodic random field with Gaussian distribution is generated. The GRF, which is correlated using a field-field correlation function, then cut at one level to generate a two-phase medium, in which two independent Boolean processes generate the small scale structures (Fig. 2.6). Since two Boolean models are independent, one could easily control the porosity and length scale associated to them individually and by doing that the amount of micro- to macro-porosity and the connectivity of each phase is set. It should be noted that to eliminate anisotropic effect, spherical particles were used for generating both Boolean models.

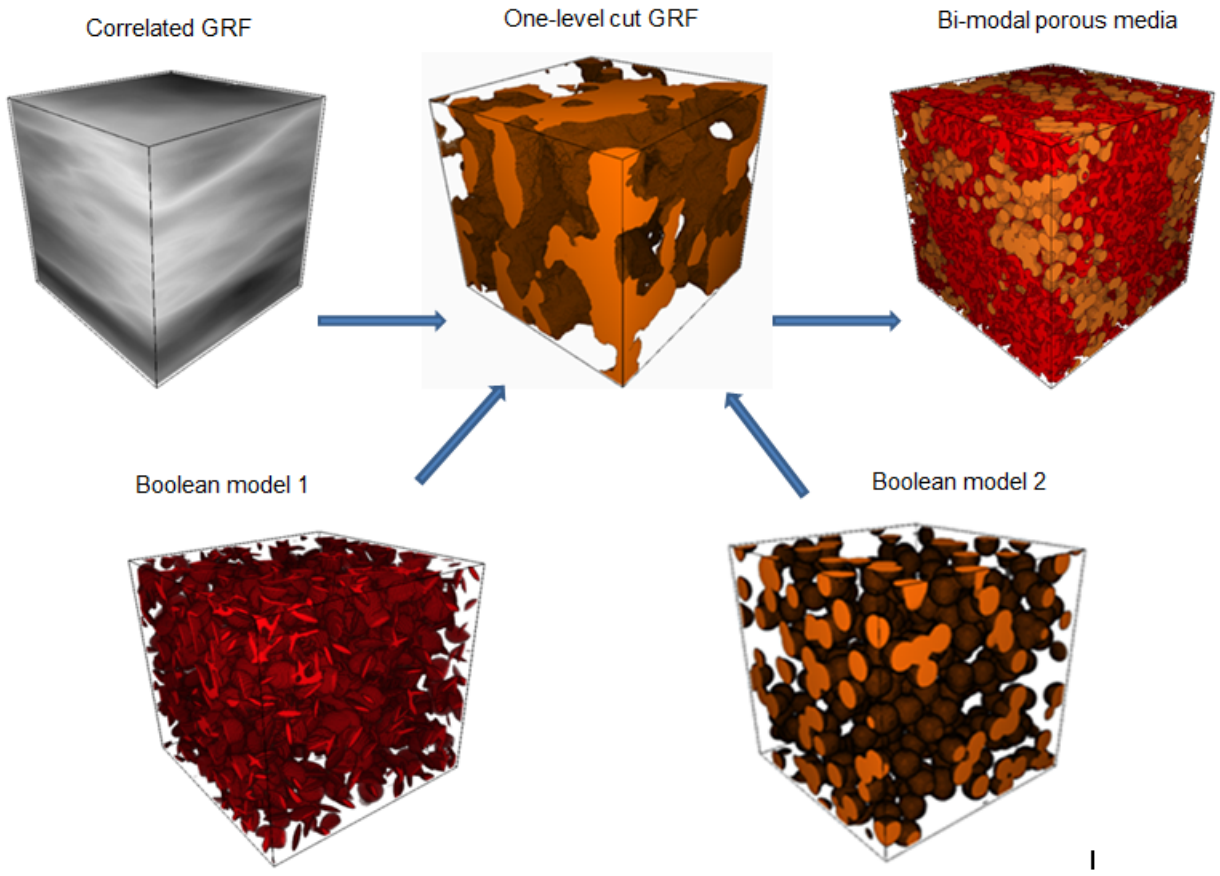

Figure 2.6: Schematic for generating the dual-scale porosity media. While the large scale heterogeneity is controlled by GRF model, the small scale structural and petrophysical properties are dictated by Boolean models.

CHAPTER 3

PORE SCALE MODELING: SINGLE PHASE FLOW

This chapter briefly describes the challenges for fluid flow simulation in heterogeneous porous media and highlights the capability of the pore scale modeling techniques to address those problems. The lattice Boltzmann method used in this thesis is explained and implemented to show the significance of micro-porosity on the effective permeability of some 2D, dual-scale porosity models. The concept of the characteristic length, as a good estimator of permeability, is then introduced before being used for analysing the effect of microporosity on single phase fluid flow in 3D heterogeneous model structures. It is also shown through permeability calculations and flux tracking analyses on some selected heterogeneous model structures.

3.1 Heterogeneity and fluid flow in porous media

Investigating fluid flow in a porous medium without considering the length scales involved is meaningless. While there are some porous media which exhibit homogeneity, natural porous media are often heterogeneous, that is, their effective properties depend on the size of the sample. This scale dependency of many properties of a porous medium requires us to be aware of the suitability of the volume of the medium on which a property is calculated [23]. Moreover, it reminds us that any proper characterisation of a porous medium must have a length scale associated with it [162].

Depending on a phenomenon that occurs in a porous medium, the scale of interest may vary from a molecular level on the order of $10^{-11} - 10^{-9}m$ to a mega level on the order of 10^2 km for some regional applications [135]. Describing heterogeneities of a natural porous medium at mainly four distinct length scales, the following classification was proposed by [73]:

- Microscopic heterogeneities are of the order of 10^{-5} to 10^{-3} m and correspond to the scale of individual pores and grains.

- Macroscopic heterogeneities occur at the core to log scale and are of the order of 10^{-2} to 10^{0} m.
- Megascopic heterogeneities characterise the entire field scale and are of the order of 10 to 10^{3} m.
- Gigascopic heterogeneities are relevant to the regional scale description of processes and are of the order of $10^{3} - 10^{5}$ m or larger.

While there is no standard classification for heterogeneity, scales as mentioned above could span over many orders of magnitude.

Hydrocarbon reservoirs are one of the best examples of heterogeneous porous media. An early approach to the solution of multiphase flow in reservoir engineering was based on one-dimensional flow and for homogeneous porous medium. The principal assertion in that formulation was based on a simple extension of single phase Darcys law to two-phase flow through the use of constitutive relations (relative permeability and capillary pressure). Later, with progresses in experimental techniques and numerical simulators, reservoirs were approximated as layered systems, with up to 10 geological layers, where each layer was still generally uniform in its physical properties. Characterising a reservoir as a homogeneous medium changed drastically with the recognition of reservoir heterogeneities, with different spatial correlation characteristics in all directions, and with scale dependent properties. Currently, reservoir description is based on multi-scale processes ranging from the pore scale to the field scale. While the pore scale is appropriate for formulating the fundamental governing equations, the core scale is a common scale in the laboratory where rock properties are measured to populate detailed geological models and the field scale is the relevant scale for production and reservoir simulation. The multiscale nature of heterogeneities in the subsurface reservoirs results in many challenges for fluid flow simulation. There are two main approaches for flow and displacement of multiple fluids in porous media: continuum models and discrete or pore scale models [162, 135].

3.1.1 Continuum-based models

Continuum-based models represent the classical approach to the solution of fluid flow equations in porous media. Based on the assumption that the physical law that governs the flow and transport at the microscale are well understood, one can write the macroscopic differential equations for mass, momentum and energy. By applying appropriate initial and boundary conditions in conjunction with constitutive relations, the governing equations can be solved for velocity and pressure

field. Due to their convenience, continuum-based models have been widely used in many disciplines but they have some limitations.

An empirical extension of Darcys law supplemented with capillary pressure and relative permeability relations is one of the continuum-based theories of multiphase flow in porous media that has been proven insufficient to account fully for the physics of the flow at different scales [51]. While the governing physical laws for fluid transport at the microscopic level are well understood the solution of principal equations for a complex geometry such as porous media with irregular interfaces is practically and economically impossible for the domain sizes required [162]. So, a length scale much larger than the dimension of individual pores or fractures is essential. An accurate macroscopic description of fluid flow through porous media depends on the precise constitutive relations, such as capillary pressure and relative permeability curves. Undoubtedly, the most reliable method for determining these relations are laboratory measurements performed on reservoir cores. However, retrieval of sufficient number of reservoir cores is not economically efficient and is limited to sometimes less than ten samples per reservoir [38]. Apart from that, conducting laboratory experiments for measuring relative permeability and capillary pressure in multiphase systems is very difficult [76, 138]. In addition, the assumption of well-known underlying pore scale processes is often violated for many multiphase systems [135]. The complexity of pore scale processes involved in chemical EOR, for instance, introduces many uncertainties to measurements performed at the laboratory scale and seems to be impossible to quantify without considering pore scale studies.

3.1.2 Discrete models

An alternative or complementary technique to derive transport properties of rocks is to start describing phenomena at the microscopic or pore scale level and extend it to macroscopic and even larger scales. These models, which are the focus of this thesis, are particularly useful when the connectivity of the pore space is important [162].

Being applied at the pore scale, discrete models are ideal for evaluating the assumptions related to continuum-based models for some complex multiphase systems in which pore scale processes control the macroscopic phenomena. The results from pore scale processes can then be incorporated into constitutive theories to achieve a more accurate description of processes happening at the larger scale of interest [135].

Recent progress in the field of imaging and characterisation of porous materials has spurred an explosion of interest in pore scale modeling techniques. Different

numerical pore-scale methods have been developed for computation of constitutive relations from the underlying microstructure, including smoothed particle hydrodynamics (SPH), volume of fluids, pore network models (NM) and lattice Boltzmann method (LBM). Among them, the last two methods have received more attention within recent years. The premise of the network model is that the complex pore space can be represented by an equivalent network of interconnected pores. This idealisation of porous media reduces the amount of required data and the computational cost, but may have considerable effects on the predicted results due to the abstractions needed to describe the complex pore space. A combination of microstructure images with network modeling has alleviated this problem to some extent and recently some successful applications have been reported [141, 35]. The lattice Boltzmann method is an efficient computational fluid dynamic approach and an appropriate choice for handling complex boundaries such as those in porous media. Furthermore, the simplicity of coding and parallel computing of LBM made this model one of the most popular methods in implementing computational fluid dynamics at the pore scale. In this thesis, we use LBM for simulating fluid flow directly on the voxelated images.

3.2 Lattice Boltzmann method

3.2.1 Background

The lattice Boltzmann method originates from the lattice gas automata (LGA), which inherits the fundamentals of molecular dynamics. The first lattice gas (LG) model for solving Navier-Stokes (NS) equations was proposed by [65] and later named as FHP model. These authors, for the first time, realised the importance of the lattice symmetry for recovering NS equations and constructed their model on an equilateral triangular lattice (Fig. 3.1).

Based on lattice gas automata (LGA), the FHP model [65] suffers from some limitations. Statistical noise, a need for a remapping scheme to make the triangular lattice amenable to numerical computations, and non-Galilean invariance are some major drawbacks of the FHP model [187]. Subsequently, some lattice Boltzmann models were proposed as an alternative to LG models, which were noise-free and Galilean invariant [148, 149]. Utilising multi-scale techniques, these models could obtain the exact NS equation at the second order of approximation under the stability conditions of Mach number and the viscosity.

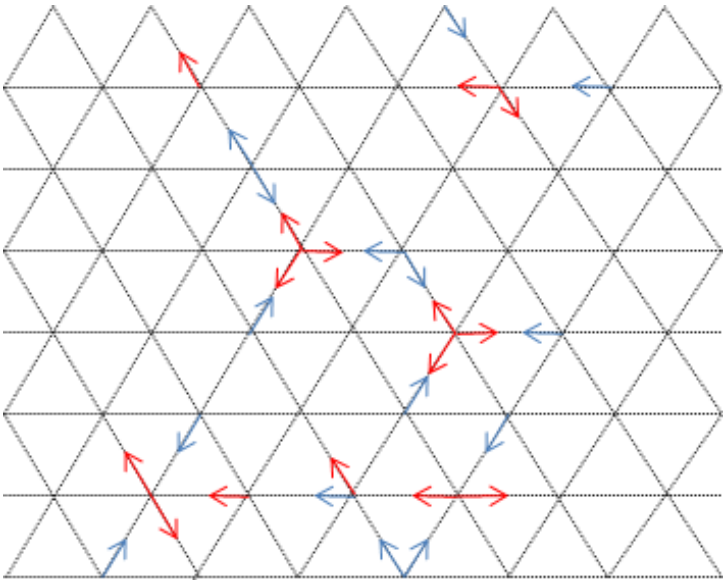

Figure 3.1: Triangular lattice with hexagonal symmetry. Particles at time t and $t+1$ are marked by blue and red arrows, respectively. (reproduction from [65])

3.2.2 Mathematical description

LBM is a way of applying the Boltzmann transport equation to simulate fluid flow on discrete grids. Instead of addressing the fluid flow at the macroscopic continuum level as in the Navier-Stokes equations, the Boltzmann transport equation expresses fluid motion in terms of the probabilistic motion of the individual particles. These particles (or effectively, particle number density) are moved under the various macroscopic forces and microscopic interparticle interaction forces. The lattice Boltzmann method solves discrete Boltzmann equation for the particle distribution function, $f_\alpha(\mathbf{x}, t)$, where macroscopic fluid flow quantities such as density and velocity are obtained through moment sums [187]:

$$\rho(\mathbf{x}, t) = \sum_{\alpha=1}^{b} f_\alpha(\mathbf{x}, t) \ , \tag{3.1}$$

$$\mathbf{u}(\mathbf{x}, t) = \frac{1}{\rho(\mathbf{x}, t)} \sum_{\alpha=1}^{b} \mathbf{c}_\alpha f_\alpha(\mathbf{x}, t) \ . \tag{3.2}$$

$\rho(\mathbf{x}, t)$ and $\mathbf{u}(\mathbf{x}, t)$ are fluid density and velocity, respectively. $\mathbf{c}_\alpha$ is the microscopic velocity in α-direction and b is the number of velocity components. A two-step process consisting of a collision coupled with a streaming phase governs the particle distribution in each time step. During the collision step mass and momentum are redistributed while in the streaming phase distributions at a lattice position $\mathbf{x}$, stream along links to the nearest neighbor sites located at the position $(\mathbf{x}+\mathbf{c}_\alpha)$ [185].

The particle distribution function $f_\alpha(\mathbf{x}, t)$ is governed by the discrete Boltzmann equation given by:

$$f_\alpha(\mathbf{x} + \mathbf{c}_\alpha, t + 1) = f_\alpha(\mathbf{x}, t) + \Omega_{c,\alpha}(\mathbf{x}, t) \ , \tag{3.3}$$

where $\Omega_{c,\alpha}$ is the collision operator which represents the rate of change of f_α resulting from collision. The Bhatnager-Gross-Krook (BGK) approximation [31], as the simplest LBM, employs a linear form collision operator in which the distribution function is expanded about its equilibrium value:

$$\Omega_{c,\alpha} = -\frac{f_\alpha(\mathbf{x}, t) - f_\alpha^{eq}(\mathbf{x}, t)}{\tau} \ . \tag{3.4}$$

Here, f_α^{eq} is the equilibrium distribution function and τ is the relaxation time controlling the rate of approach to equilibrium. There are different types of lattices for lattice Boltzmann method. In this study we use $D2Q9$ and $D3Q19$ [148] configurations for $2D$ and $3D$ simulations, respectively (Fig. 3.2). In $D3Q19$, for instance, the velocities make connection with the 18 nearest neighbours in addition to allowing a population at rest and given by:

$$\mathbf{c}_\alpha = \mathbf{c}\mathbf{e}_\alpha = \begin{cases} (0,0,0)c & \alpha = 0 \\ (\pm 1,0,0)c, (0,\pm 1,0)c, (0,0,\pm 1)c & \alpha = 1, ..., 6 \\ (\pm 1,\pm 1,0)c, (\pm 1,0,\pm 1)c, (0,\pm 1,\pm 1)c & \alpha = 7, ..., 18 \end{cases} \tag{3.5}$$

where $c = \frac{\Delta x}{\Delta t}$ is the basic velocity on the lattice ($1\ lu.ts^{-1}$ in the simplest implementation). The equilibrium distribution function is given by:

$$\begin{aligned} f_\alpha^{eq} =& w_\alpha \rho \left[1 + 3\frac{c_\alpha.\mathbf{u}}{c^2} + \frac{9}{2}\frac{(c_\alpha.\mathbf{u})^2}{c^4} - \frac{3}{2}\frac{\mathbf{u^2}}{c^2} \right] \qquad \alpha = 1, ..., 18 \\ f_\alpha^{eq} =& w_\alpha \rho \left[1 - \frac{3}{2}\frac{\mathbf{u^2}}{c^2} \right] \qquad \alpha = 0 \end{aligned} \tag{3.6}$$

where $w_0 = \frac{1}{3}$, $w_{1,...,6} = \frac{1}{18}$ and $w_{7,...,18} = \frac{1}{36}$. Using the Chapman-Enskog expansion, Eqns. 3.1 - 3.6 recover the Navier- Stokes equation to the second order of accuracy [185], with the kinematic viscosity given by:

$$\nu = \frac{2\tau - 1}{6} \ . \tag{3.7}$$

Note that to have a positive viscosity, τ should be greater than 1/2. The value of $\tau = 1$ is the safest and leads to $\nu = 1/6\ lu^2 ts^{-1}$.

3.2.3 Boundary conditions

The key issue in all numerical computations is boundary and initial conditions. There are different classes of boundary conditions (BC) including: periodic,

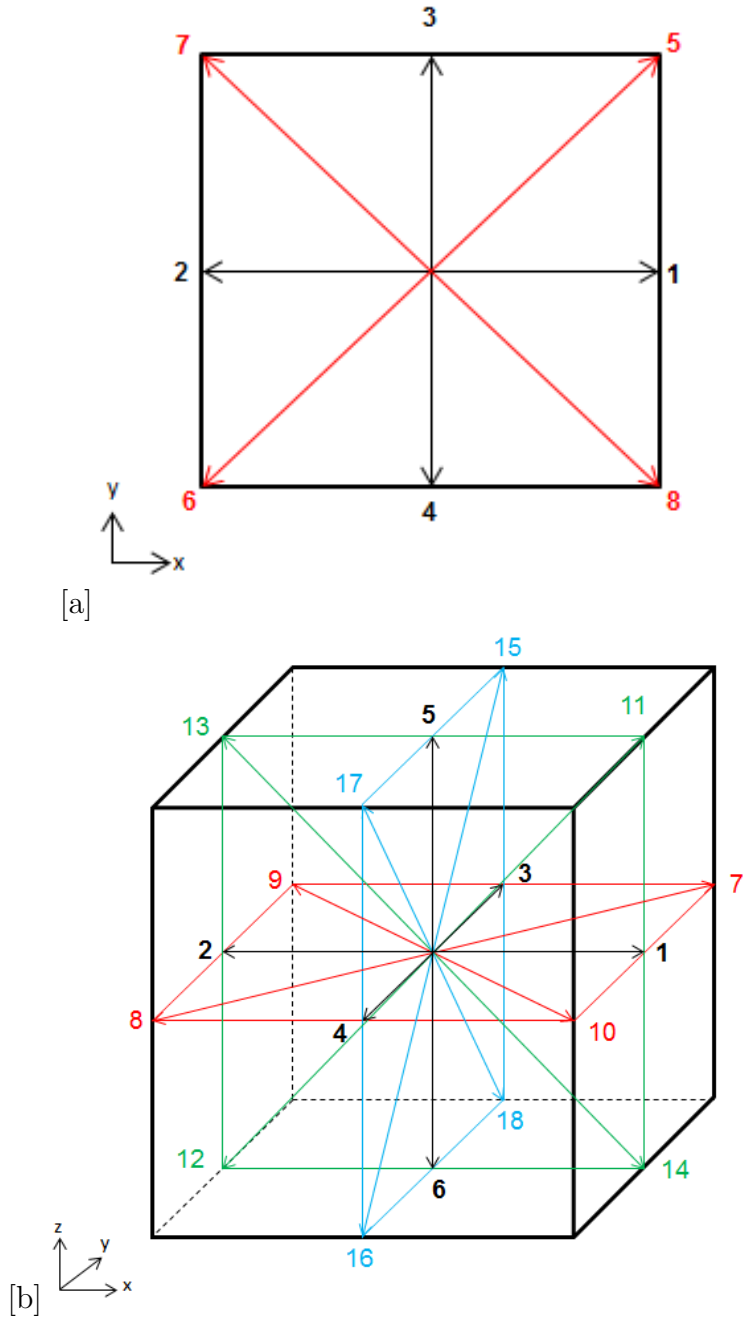

Figure 3.2: Lattice configuration with arrows indicating the direction of microscopic velocity components. [a] D2Q9, two dimensional with 9 velocity components including the rest particle at the centre. [b] D3Q19, three dimensional with 19 velocity components.

no-slip, free-slip, frictional-slip, sliding walls and open inlet/outlet boundary [185]. While the macroscopic properties such as density and velocity of the fluid nodes are calculated by the summation of the microscopic distribution function (see Eqn.3.1 and Eqn.3.2), they are given at the boundary nodes and need to be transformed into the missing distribution functions. Velocity and pressure boundary condition are two of those which have been implemented differently by various authors. Here, no-slip, periodic and mirror boundary conditions which were used vastly in our simulations are explained. Velocity and pressure boundary conditions are introduced afterwards followed by the description of the gravitational body force, as a constant driving force in our simulations.

3.2.3.1 No-slip boundary condition

The most often used boundary condition in LB fluid flow simulations is the no-slip boundary condition. Undoubtedly, successful application of LBM in simulation of fluid flow in complex geometries such as porous media is partly due to the ease of handling of solid boundaries through the bounce back scheme. The basic yet intuitive idea behind the bounce back scheme is that the incoming particle densities, or distribution functions, at wall nodes are reflected back to the original fluid nodes from which they were propagated. This results in impermeable wall and no-slip at the wall. The trivial implementation of this condition allows one to simply introduce obstacles into the fluid domain.

The computationally efficient implementation of the bounce back scheme has been one of the major research interests in LB application. There are two main approaches for implementing bounce back scheme: Full-way bounce back and half-way bounce back. In full-way bounce back, the reflection of particles at the solid nodes takes place during the collision step. Fig. 3.3 shows a 2D, simple representation of this approach in which "Ω" and "$\partial\Omega$" specifies the fluid domain and the boundary, respectively. For the sake of abstractness, only one distribution function has been shown in this figure. As can be seen, the distribution function is streamed from the fluid node to the neighboring solid node, its direction reversed during the collision step and finally streamed back to the original fluid node. While straightforward to implement, this approach has been proven to be first-order accurate in time and space [136].

By locating the no-slip boundary approximately half-way between the solid and fluid nodes, second-order accuracy is obtained [46], but the exact position depends on fluid viscosity. An astonishing improvement was suggested by Ziegler [209], who proposed a mid-grid implementation of bounce back scheme. By applying the collision operator at the wall node the effect of viscosity and changing velocity

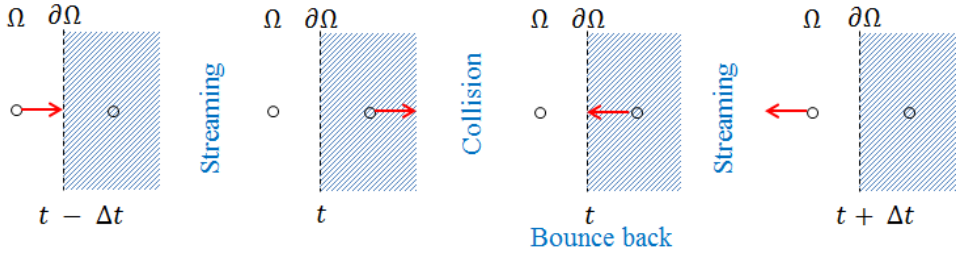

Figure 3.3: Full_way bounce back boundary condition. The inversion of the distribution functions takes place during the collision step.

throughout the calculation domain was applied correctly. The suggested technique in this article returns the wall location to the first row of nodes resulting more accurate near-wall velocity than Cornubert et al. approach [46]. In this approach, named as half-way bounce back, the inversion of particle density takes place during the streaming step (Fig. 3.4). In contrast to full-way bounce back, in this approach the reflection of particle velocity happens at the solid wall located mid-way between the fluid node and the solid node. This simple and slightly different post-processing procedure could make the bounce back scheme second order accurate [209]. In this study, we implement the no-slip boundary condition through the half-way bounce back scheme.

3.2.3.2 Periodic boundary condition

Periodic boundary condition is one of the simplest boundary conditions and often used to simulate a large system by modeling a small part of it. To implement a periodic boundary condition in the flow direction for a fluid flowing from the left to the right in a pipe, for instance, the left boundary nodes are attached to the nodes on the right boundary and are treated as neighboring nodes. In such a case, one could imagine that the fluid that leaves the pipe from the outlet on the right

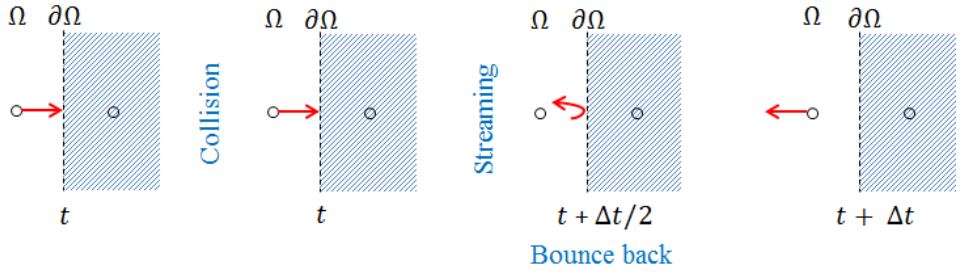

Figure 3.4: Half_way bounce back boundary condition. The inversion of particle velocities takes place during the streaming step.

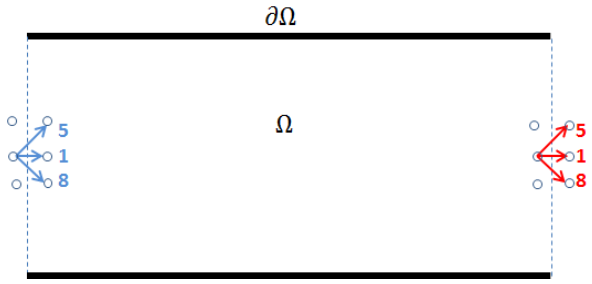

Figure 3.5: Periodic boundary condition. The post-collision distribution functions of particles on the outlet boundary are translated into the post-streaming distribution functions of particles on the inlet boundary.

could reenter into the domain from the inlet on the left. In LBM, this condition is implemented by considering the post-collision distribution functions of particles on the outlet boundary and shifting them to the post-streaming distribution functions of particles on the inlet (see Fig. 3.5). In other words, the post-collision distribution functions of the nodes on the outlet boundary are copied onto the nodes on the inlet boundary as if the propagation step was carried out. Although a very useful condition, periodic boundary conditions should be used carefully. Implementing it for the structures similar to one shown in Fig 3.6, which are periodic by themselves, does not need any more treatment.

For non-periodic structures, however, two approaches might be followed. One may still use the periodic boundary condition by adding some fluid jackets in the

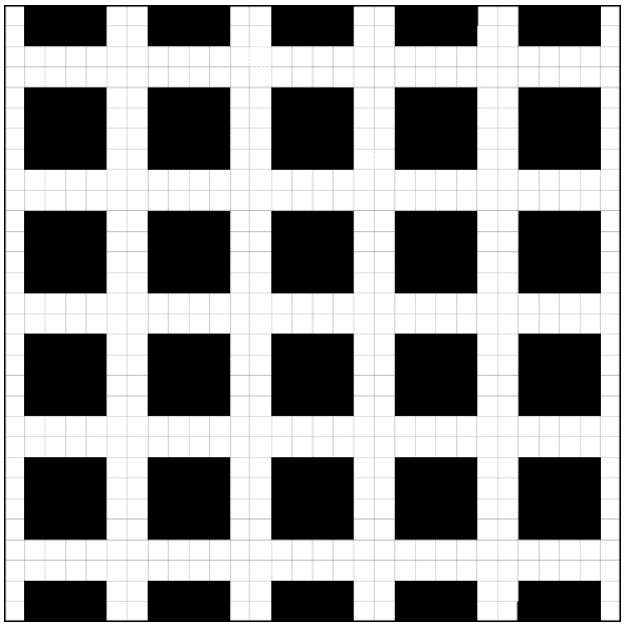

Figure 3.6: An interface of a periodic structure as an ideal example for implementing periodic boundary condition.

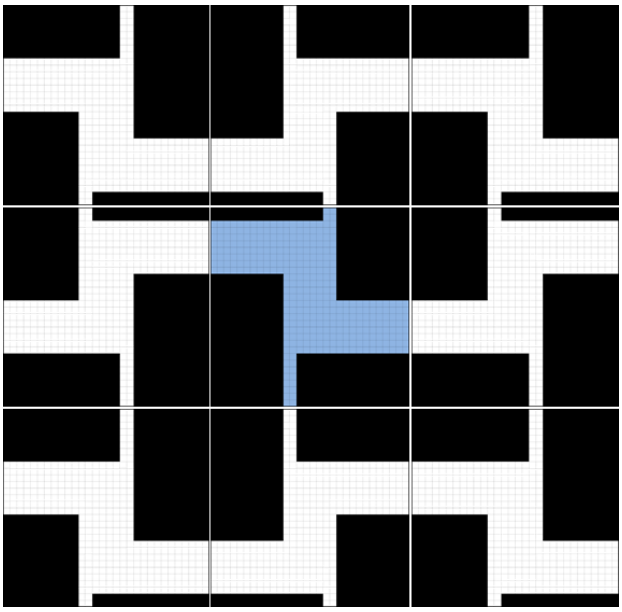

Figure 3.7: A schematic representation of mirror boundary condition. The main structure, shown in blue, is mirrored along its boundaries.

inlet and outlet boundaries. Fluid jackets are essentially free flow regions and serve as boundary layers. In the second approach, the main structure is mirrored along its boundaries. This allows the continuity of the pore space to be preserved. Figure 3.7 shows an implementation of mirror boundary condition which makes an infinite computational domain. For the sake of better representation, the pore space of the main structure has been shaded in blue.

3.2.3.3 Velocity boundary condition

This condition constrains the flux at the boundaries where a constant velocity vector is specified and the macroscopic density is computed on the basis of conditions inside the domain. The pressure is then computed from the macroscopic density via an equation of state [187]. Fig. 3.8 shows a simple example in which solid black

Figure 3.8: Schematic representation of known (shown in blue) and unknown (red) particle distribution functions for implementing constant velocity and constant pressure boundary condition.

lines are walls and dashed lines depict the inlet and outlet boundaries. As can be seen, for the left boundary, the distribution functions f_1, f_5 and f_8 are unknown, while for the nodes on the right boundary, f_2, f_6 and f_7 are not known. Suppose the boundary condition is that horizontal velocity $u = u_0$ and vertical velocity $v = 0$. For the nodes on the left boundary, for instance, f_3, f_4, f_7, f_2 and f_6 are coming from the nodes in the domain and are already known. Four equations are needed to calculate three unknown particle distribution functions f_1, f_5, f_8 and density. The formula for the macroscopic density is one equation:

$$\rho = \sum_{\alpha} f_\alpha = f_0 + f_1 + f_2 + f_3 + f_4 + f_5 + f_6 + f_7 + f_8 \ . \tag{3.8}$$

The contribution of particle distribution functions into the macroscopic velocity in x and y directions, provides two equations:

$$\rho u_0 = f_1 + f_5 + f_8 - f_2 - f_6 - f_7 \ , \tag{3.9}$$

and

$$0 = f_3 + f_5 + f_7 - f_6 - f_4 - f_8 \ . \tag{3.10}$$

The fourth equation, as proposed by [211], can be written by assuming the bounce-back condition in the direction normal to the boundary:

$$f_1 - f_1^{eq} = f_2 - f_2^{eq} \ . \tag{3.11}$$

Solving this system of four equations will leave us with four unknowns. An analogue procedure is followed for all boundaries. Fig. 3.9 shows an example of fluid flow in a slit of width $\mathrm{L}_y = 22lu$ using constant velocity boundary conditions.

3.2.3.4 Pressure boundary condition

In contrast to the velocity boundary condition, the pressure (Dirichlet) boundary condition constrains the pressure at the boundaries. Using an equation of state which relates the pressure to the density, the density is specified at the boundaries from which velocity is computed [187]. For a single component D2Q9, for instance, the pressure is related to the density by:

$$P = c_s^2 \rho = \rho/3 \ , \tag{3.12}$$

where $c_s = 1/\sqrt{3}$ is the physical speed of sound and ρ is the macroscopic density. Similar to velocity boundary condition, the distribution function at the boundary needs to be determined properly. For left boundary nodes, for example, after streaming three particle distribution functions f_2, f_5 and f_8 are pointing from the

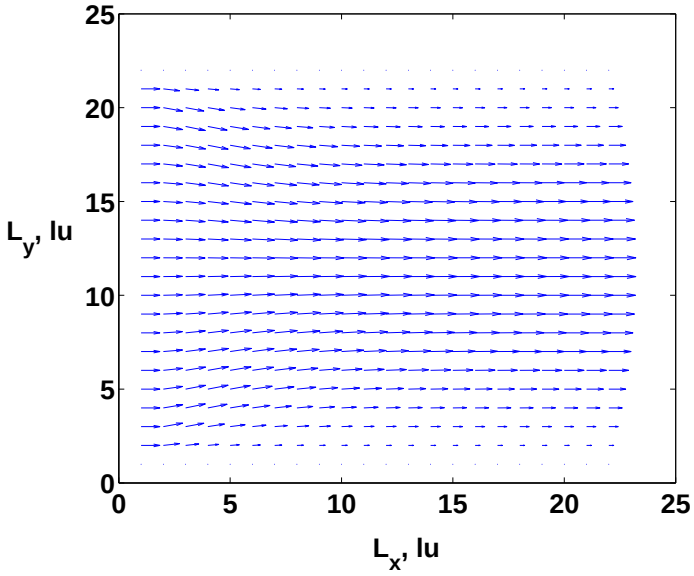

Figure 3.9: Local velocity components in a slit of width 22 lu by implementing velocity boundary condition The effect of entry length effect is evident.

boundary into the domain and remain unknown. Including unknown velocity, we have four unknowns and need four equations to determine these. Suppose the boundary condition of $\rho = \rho_0$ we will have:

$$\rho_0 = \sum_{\alpha} f_\alpha = f_0 + f_1 + f_2 + f_3 + f_4 + f_5 + f_6 + f_7 + f_8 \ . \tag{3.13}$$

as the first equation. The formula for the macroscopic velocity gives two more equations. Here, the velocity in horizontal direction is u, which is unknown and needs to be calculated, while the velocity in the vertical direction, v, is assumed as zero.

$$\rho_0 u = f_1 + f_5 + f_8 - f_2 - f_6 - f_7 \ , \tag{3.14}$$

and

$$0 = f_3 + f_5 + f_7 - f_6 - f_4 - f_8 \ . \tag{3.15}$$

The fourth equation is given by assuming the bounceback boundary condition in the direction normal to the boundary [211]:

$$f_1 - f_1^{eq} = f_2 - f_2^{eq} \ . \tag{3.16}$$

This will close the system of equations that can be solved for three unknown distribution functions and velocity. Figure 3.10, shows the velocity components for a fluid flowing in a slit of width 22 lu under a constant pressure boundary condition.

While using velocity boundary condition could be potentially useful for investigating the entry length effect, its implementation with simple LBM could raise

some difficulties. Using constant velocity at the boundaries in the simple compressible model will cause the system to not conserve the mass. A combination of pressure boundary condition and velocity boundary condition may alleviate this problem, but the velocity and density at the inlet and outlet must be different [187]. In addition, since there is no direct mapping between the macroscopic evolution of the flow velocity and particle distribution function in LBM, implementing velocity and pressure boundary condition is not straightforward [106]. For example, to implement velocity boundary condition, one has to translate the velocity into the particle distribution functions at the boundaries. While macroscopic velocity and density are easily calculated from particle distribution functions (see Eqn.3.1 and Eqn.3.2), the reverse procedure is more complex.

3.2.3.5 Gravitational body force

An alternative and more simple approach for introducing a force to make a fluid flow is applying a gravity force as a driving force. The lattice Boltzmann equation with a force term is given by [72]:

$$f_\alpha(x + c_\alpha, t + 1) = f_\alpha(x, t) + \Omega_{c,\alpha}(x, t) + F_\alpha \ . \tag{3.17}$$

The following formulation for the forcing term, F_α, were proposed by two groups independently [119, 39, 105] and were adapted in all our simulations:

$$F_\alpha = w_\alpha \left[\frac{(\mathbf{c}_\alpha - \mathbf{u}^*)}{c_s^2} + \frac{(\mathbf{c}_\alpha \ \cdot \ \mathbf{u}^*)\mathbf{c}_\alpha}{c_s^4} \right] \ \cdot \ \mathbf{F} \ . \tag{3.18}$$

Here, c_α is the microscopic velocity in α-direction. $w_0 = \frac{1}{3}$, $w_{1,\ldots,6} = \frac{1}{18}$ and $w_{7,\ldots,18} = \frac{1}{36}$. c_s is the sound velocity on the lattice and is equal to $1/\sqrt{3}$. Equilibrium velocity, $\mathbf{u}^*$, is equivalent to fluid velocity and is given by: $\rho\mathbf{u}^* = \sum_\alpha c_\alpha f_\alpha$. $\mathbf{F} = \rho\mathbf{g}$ is the body force density, where g is the acceleration due to F [72]. To avoid stability problem and to make sure that the flow is always laminar, a small value of $g = 10^{-8}$ was used in all our simulations.

3.2.4 Permeability calculation from LBM

By choosing the right boundary conditions and applying an appropriate driving force, LBM solves for local velocity field. At the microscopic scale, particles are propagated between nodes and are collided with each other on the nodes where particle distribution functions are averaged at each time step resulting in macroscopic density and velocity. The local velocities are then volume averaged before being applied in Darcy's equation for calculating the permeability of the structure.

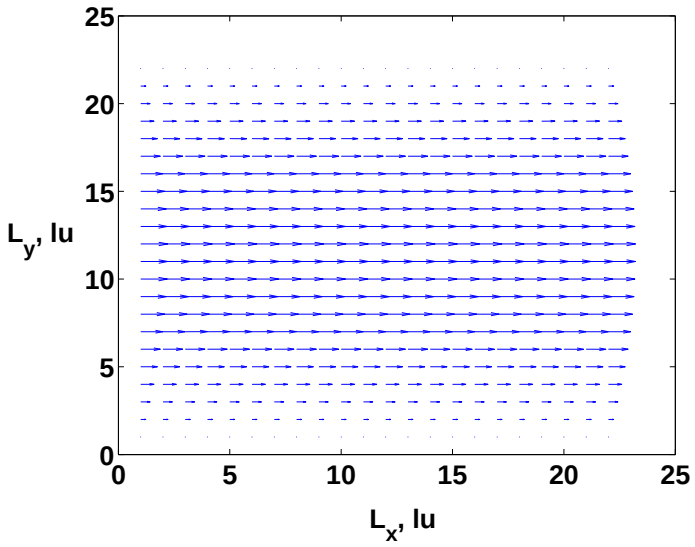

Figure 3.10: Local velocity components in a slit of width 22 lu by implementing pressure boundary conditions.

3.3 2D, heterogeneous porous media

3.3.1 Microporosity significance

To investigate the significance of microporosity on the permeability, some simple yet useful 2D model structures were constructed as binarised images. Figure 3.11 shows one example in which a 2D channel is parallel to a porous matrix region. The porous matrix was generated by randomly assigning solid pixels (shown in black) until the required porosity was reached. Local velocity components, calculated by LB simulation, have been superimposed on the figure. The no-slip boundary condition was applied on all solid boundaries and using the periodic boundary condition in the flow direction guaranteed the infinity of the domain in that direction. Navier-Stokes equations were solved in both free-flow and porous regions, resulting in the continuity of the velocity profile at the interface (see Fig. 3.11). An interesting point in this figure is the deviation of velocity parabola towards the interface (shown by a red rectangle in Fig. 3.11). The existence of low permeable region has caused the infiltration of fluid, flowing freely in the channel, into the porous-matrix and consequently the asymmetry of the velocity profile in the channel. This velocity shift corresponds to the slip-flow hypothesis of Beavers and Joseph [24], which would be more significant for higher porosities of porous matrix.

To quantify the effect of porous matrix on the flow through the channel and on the whole system, similar structures as shown in Fig. 3.12 with different porosities and connectivities for porous matrix and two different channel widths were built. Similar to Fig. 3.11, the medium is a binarised image. First a porous matrix region

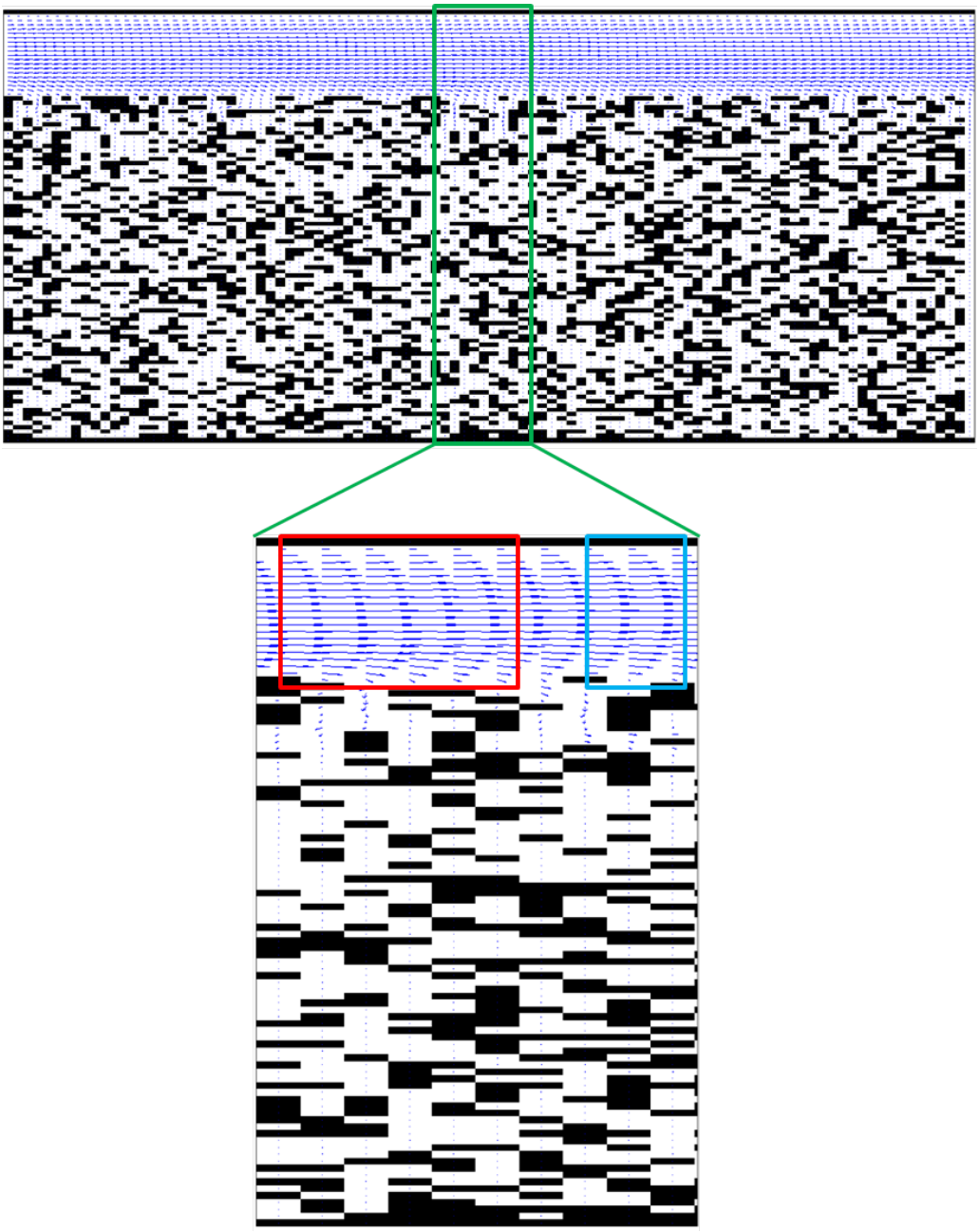

Figure 3.11: Porous matrix overlaid by a channel representing a dual-scale porous media (top). The bottom subfigure shows a zoomed section of the model (stretched for better visualisation). The light blue rectangle indicates a region where negligible infiltration occurs and the velocity profile remains parabolic whereas in the region shown by red rectangle, due to the infiltration of the fluid from the channel into the porous matrix, the velocity profile deviates from a symmetric parabola.

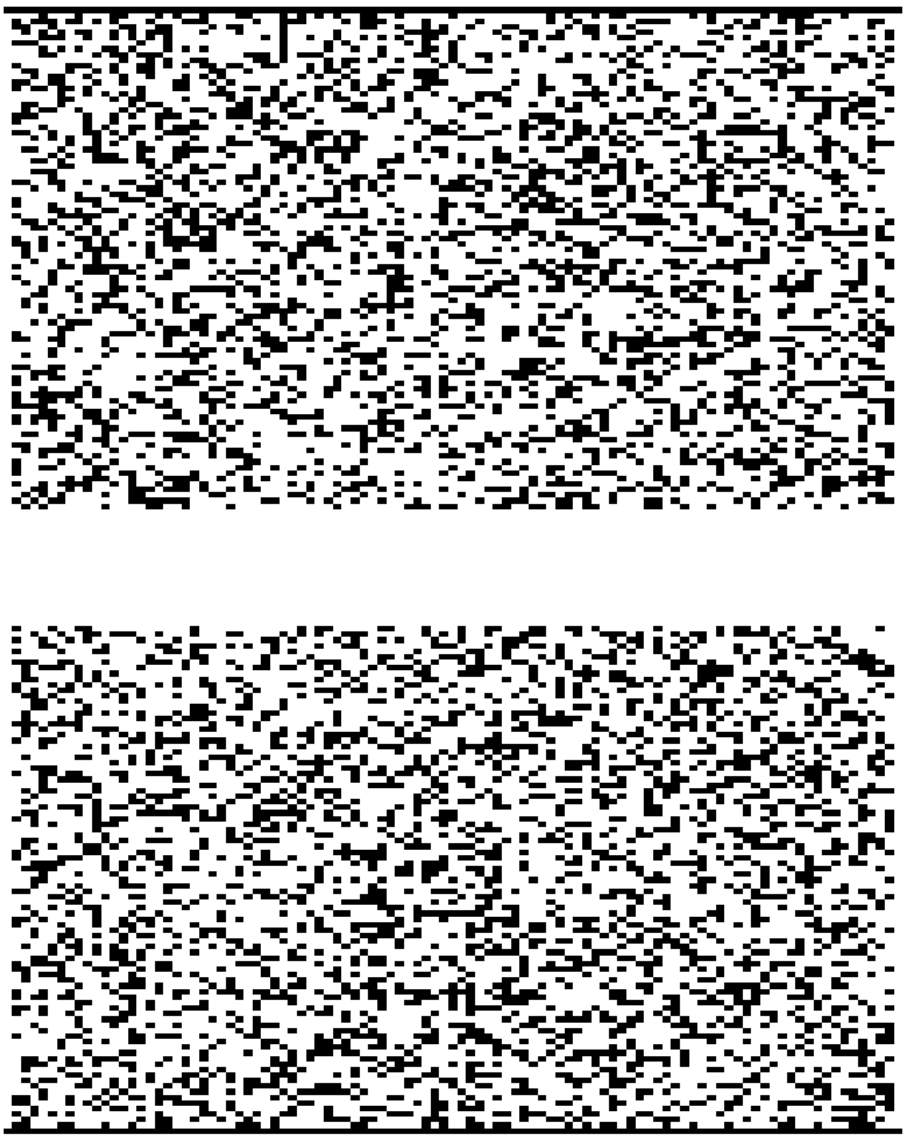

Figure 3.12: An illustration of a 2D model structure with a channel of width 19 lu and length of 100 lu. Model is discretised on 200×100 lattices.

of length 200 pixels and width of 100 pixels was generated by random positioning of solid pixels between two solid walls. Then, a channel of required width was placed in the middle of the medium by converting all covering pixels into pore pixel. In all cases, incompressible lattice Boltzmann method with gravitational body force was applied to simulate fluid flow and to obtain the velocity field. Effective permeability of the whole system was then calculated using Darcy's law.

To calculate the hydraulic conductivity of the channel, a parallel plate model [179] was considered for which an exact analytical solution exists and yields the well-known "cubic law" [202]. For a channel with aperture h, width W and length l, subjected to a differential pressure in x-direction and no-slip boundary condition

on its walls, the analytical solution for pressure and velocity are given by [201]:

$$P(x) = P_i - \frac{x}{l}(P_i - P_o) \ , \tag{3.19}$$

$$u(z) = \frac{1}{2\mu}\left(\frac{P_i - P_o}{l}\right) z(h - z) \ , \tag{3.20}$$

where P is pressure, u is velocity and μ is the viscosity of the fluid. Integrating the velocity across the channel from $z = 0$ to $z = h$ results in the total volumetric flux:

$$Q_x = -\frac{Wh^3}{12\mu}\left(\frac{P_o - P_i}{l}\right) \ . \tag{3.21}$$

Darcy's law for flow through porous media with cross sectional area $A = Wh$ and in one dimension is expressed as:

$$Q = -\frac{KWh}{\mu}\left(\frac{P_o - P_i}{l}\right) \ . \tag{3.22}$$

From Eqn.3.21 and Eqn.3.22, the permeability of the channel can be derived as:

$$K = \frac{h^2}{12} \ . \tag{3.23}$$

Figure 3.13 shows the dependency of the normalised permeability of the channel and the whole system on the normalised permeability of the porous matrix for two channel width. The value K is the effective permeability of the system including permeable matrix and channel, K_0 is that of the whole system under the assumption of impervious matrix, K_p is the permeability of the porous matrix and K_c is the channel permeability calculated from cubic law (Eqn.3.23). The ratio K/K_0 could be used as an indication of error caused by the assumption of the impervious porous matrix. It is clear that even for $K_p/K_c < 10^{-4}$ there would be an error in calculating the effective permeability of the whole system. This finding highlights the importance of micro-porous regions on the flow properties of dual-scale porosity media and disagrees with the results of previous studies [83, 109] that neglected the effect of a permeable matrix for $K_p/K_c<10^{-4}$. According to Fig. 3.13, for the channel of width 11 lu, incorporating the permeable matrix could nearly double the calculated effective permeability of the whole system when the ratio K_p/K_c increases to 10^{-1}. Compared to the wider channel, $h = 19lu$ this effect is more evident for channel of width 11 lu where the proportion of the porous matrix increases. These numerical experiments, although simple, justify the incorporation of micropores in the permeability calculation of dual-scale porosity medium.

It is worth mentioning that the 3.13 tries to highlight the significance of microporosity on the effective permeability of the whole system and not essentially the coupling of Darcy and Stokes equations at the interface of the porous matrix

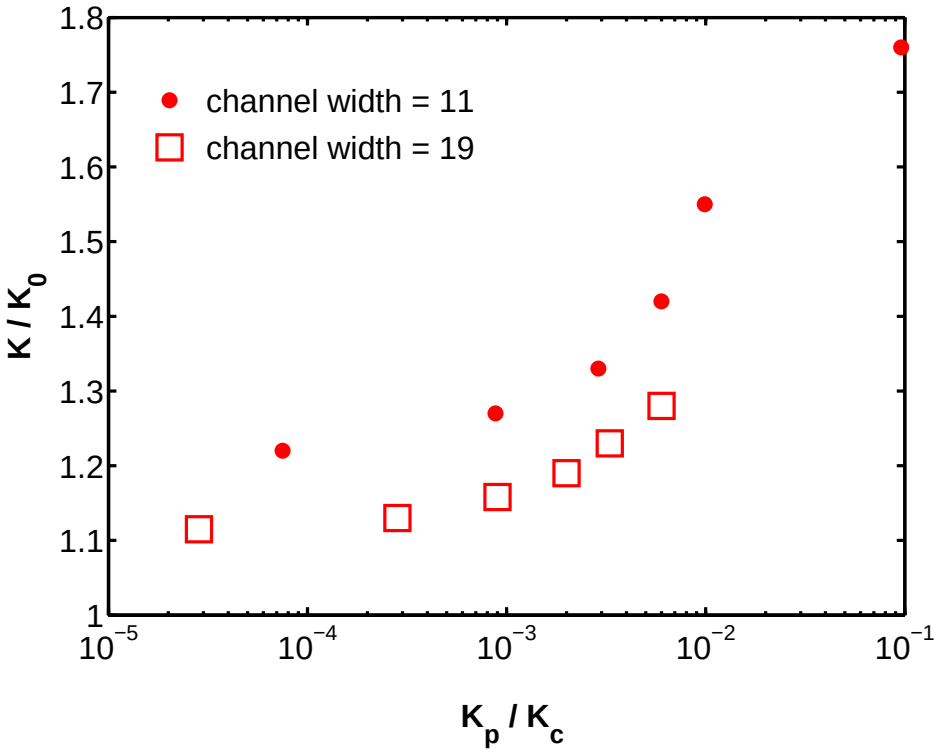

Figure 3.13: Microporosity significance for model structures with channel width of 11 and 19 *lu*. The value K is the effective permeability of the system including permeable matrix and channel, K_0 is that of the whole system under the assumption of impervious matrix, K_p is the permeability of the porous matrix and K_c is the channel permeability calculated from cubic law.

and the channel. Stokes equations were solved to calculate K, K_0 and K_p. For calculating the effective permeability of the whole system, K, if two systems (channel and porous matrix) perfectly act in parallel, arithmetic averaging could give an estimate but it overestimates the effective permeability. Geometric averaging would be a better choice for such systems.

3.4 Permeability estimation

While image-based computation of permeability of porous media using LBM is interesting, it remains computationally expensive for large 3D volumes and particularly when a large number of computations is required. In such a case, estimating permeability based on some morphological and topological properties is of great use. Below, the concept of the characteristic length as a good estimator of permeability is introduced. It will then be used as a qualitative measure for investigating the effect of microporosity on the effective permeability.

3.4.1 Characteristic length

Due to the broad interest in transport properties of porous media, there has been a huge effort to relate the permeability, as a macroscopic property, to either the geometrical [41] or hydraulic properties [166] of the porous materials. This section briefly describes various models which relate permeability to the squared value of some characteristic pore diameter.

3.4.1.1 Kozeny-Carman equations

first proposed by Kozeny [100] and later modified by Carman [41], the Kozeny-Carman (KC) equation is typically used to calculate the pressure drop of a fluid flowing through a packed bed of spherical grains. The KC equation assumes a porous medium as a bundle of capillary tubes and is developed from Poiseuille's equation for laminar flow. Its formula for estimating permeability is:

$$K = \frac{\phi (V_p/S)^2}{2\alpha} \ , \tag{3.24}$$

where ϕ is the porosity of the porous medium and V_p and S are the volume and the surface area of the pore space, respectively. The ratio V_p/S is considered as a hydraulic radius which provides a pore length scale and α as the tortuosity of the medium and could be related to the formation resistivity factor by:

$$\frac{\phi}{\alpha(\phi)} = \frac{1}{F(\phi)} \ . \tag{3.25}$$

On digitised image, which has been already discretised, ϕ and V_p/S could be obtained by counting the number of voxels and faces on the image [32, 11], although due to digital representation of objects some corrections are needed to be applied [117, 9].

Following the KC equation, more models were proposed which relate the permeability to a hydraulic radius (the pore volume divided by the pore surface area) and porosity. [137] and [195] established a relationship between formation factor, F, and tortuosity, α and proposed an equation for permeability as follows:

$$K = \frac{(r_h)^2}{c_f F} \ , \tag{3.26}$$

where c_f is a shape factor, a dimensionless number between 1.7 and 3.0, r_h is hydraulic radius and K is the permeability.

3.4.1.2 Katz and Thompson relationship

An alternative approach for permeability estimation is to implement percolation concepts to define a characteristic length for the permeability in random

porous media. Based on the percolation arguments, [5] suggested that transport in a porous medium with broad distribution of conductances is controlled by those conductances which are greater than a characteristic value. Following this concept, Katz and Thompson proposed a relationship for absolute permeability of rocks [84]:

$$K = c_k(l_c)^2(\sigma_{eff}/\sigma_f) \ , \tag{3.27}$$

where l_c is some characteristic length of the pore space, σ_{eff} is the conductivity of the rock saturated with brine of conductivity σ_f and c_k is a constant on the order of $1/226$ that depends on the pore size distribution. While more recent works suggest different values for c_k [20, 108, 161], slow variation of this parameter across a broad range of pore shapes and pore size distribution in Katz and Thompson, makes this relationship as a robust predictor of permeability [9]. By conducting mercury intrusion test on a set of 50 rocks with permeability range from 5 microdarcies to 5 Darcies, Katz and Thompson showed that the l_c corresponds to the inflection point of mercury injection curve. Similar to Eqn.3.26, Katz and Thompson equation relates the permeability to square of a characteristic length.

While correlating the permeability with other physical properties such as electrical conductivity [203] and nuclear magnetic resonance (NMR) response [87, 88, 86] have also been considered, the permeability estimates based on a characteristic pore length, l_c, was found to be the most reliable [9]. In this thesis, we calculate and use l_c as a good measure of the permeability on digitised image of model structures.

3.4.1.3 Mathematical formulation

To calculate l_c on digital images, pore size information is needed. Describing the morphology in terms of basic geometrical quantities, such as inscribed spheres, is one technique which is implemented by [9] to compute pore size distribution for the four 480^3 sandstone tomograms. In this approach, a covering radius corresponding to an opening size in the standard mathematical morphology is assigned to each point in the pore phase. Associated with the diameter of the largest sphere that can pass through the pore phase from the inlet to the outlet, l_c is defined by the percolation threshold of a non-wetting phase during a drainage experiment [9]. In other words, l_c corresponds to the largest percolating cluster of the non-wetting phase.

Using the language of mathematical morphology, the dilation of a pore phase domain A by a spherical element B of radius l_c is the set covered by all translations of B_{l_c} centered in A

$$A \oplus B_{l_c} = \cup_{r \in A, s \in B_{l_c}} (\mathbf{r} + \mathbf{s}) \ . \tag{3.28}$$

The erosion is the dual operation corresponding to dilation of the complement A^c of A and represents all points in A not covered by a sphere B_{l_c} centered out of A via

$$A \ominus B_{l_c} = (A^c \oplus B_{l_c})^c \,. \tag{3.29}$$

The connected cluster is defined when $(A \ominus B_{l_c})$ first percolates and the resultant domain after opening is given by $(A \ominus B_{l_c}) \oplus B_{l_c}$ [9, 169].

Argued by Katz and Thompson [84], l_c could be measured from mercury intrusion measurements. Alternatively, the drainage process could be simulated for measuring l_c. Considering all possible invading sphere radii, Hilpert and Miller proposed a pore-morphology based approach which results in complete mercury intrusion capillary pressure curve [75]. The maximal of the pore size distribution from simulated mercury intrusion corresponds to the value of l_c [9].

3.5 3D, heterogeneous porous media

For bimodal porous media, it would be useful to understand the significance of each pore type on the fluid flow prior to attempting to couple them. To show the effect of microporosity on the effective permeability, ten 4-phase model structures with GRF fraction of 0.0, 0.2, 0.3 $\cdots$ 1.0 were made while the particle density in both Boolean model 1 and 2 kept fixed in all of them. GRF fractions 1.0 and 0.0 correspond to pure micro and pure macro, respectively. As detailed before and depicted in Fig. 2.6, heterogeneous models were generated by combining two Boolean processes, which were spatially separated by a cut through a Gaussian random field. While the ratio of micro-to-macro porosity was controlled by adjusting the level cut, an attempt was made to have a sufficient contrast in the permeability of micro- and macro-phase. The parameters of Boolean models are summarised in Tab. 3.1. Boolean model 1 forms the micro-porous phase whereas Boolean model 2 constitutes the macro-pores and there is an order of magnitude difference in the permeability of constituting Boolean models.

Table 3.1: Characteristics of Boolean models used for making bi-modal porous media D-G.

Particle model	Particle diameter (lu)	Particle fraction	Critical length (lu)	K_z (D)
Boolean Model 1	12	0.5	8	0.871
Boolean Model 2	24	0.4	20	8.08

Compared to 2D simulations, the calculation of permeability on 3D model structures using LBM is more expensive. For this reason, a characteristic length as

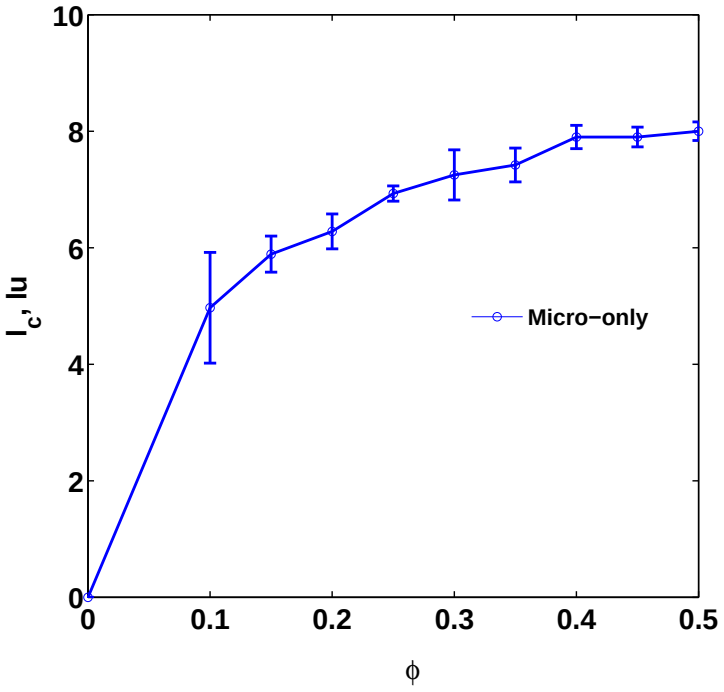

Figure 3.14: The relation between critical length and porosity for micro-phase in bimodal porous media with GRF fraction of 0.0, 0.2, 0.3 $\cdots$ 1.0.

a good estimate of permeability is used to show the significance of microporosity and screening the right models for coupling micro- and macropore in the following chapters.

3.5.1 Microporosity significance through critical diameter analysis

Defined as the maximum diameter of spheres that can penetrate through the porous medium from the inlet to the outlet, the critical diameter (or critical length) for each micro- and macro-phase was calculated separately and the results are shown in Fig. 3.14 and Fig. 3.15. For each GRF fraction, 10 realisations were built and the error bars in these figures show the variation in critical length, while the variation in porosity is negligible. As can be seen in Fig. 3.14, the critical length of micro-phase is zero at GRF fraction of zero. By adding more microporosity into the system, the critical length increases to 8.0 lu at porosity 0.5. This point corresponds to Boolean model 1 in Tab. 3.1. Similarly, as the fraction of macro-phase increases or the GRF fraction decreases, the critical length of macro-phase increases (see Fig. 3.15) and finally reaches to about 20 lu at porosity 0.6, corresponding to Boolean model 2 in Table 3.1.

The effect of microporosity is clearer in Fig. 3.16, where the critical length of pore phase (micro + macro) versus porosity has been plotted. Again, the error

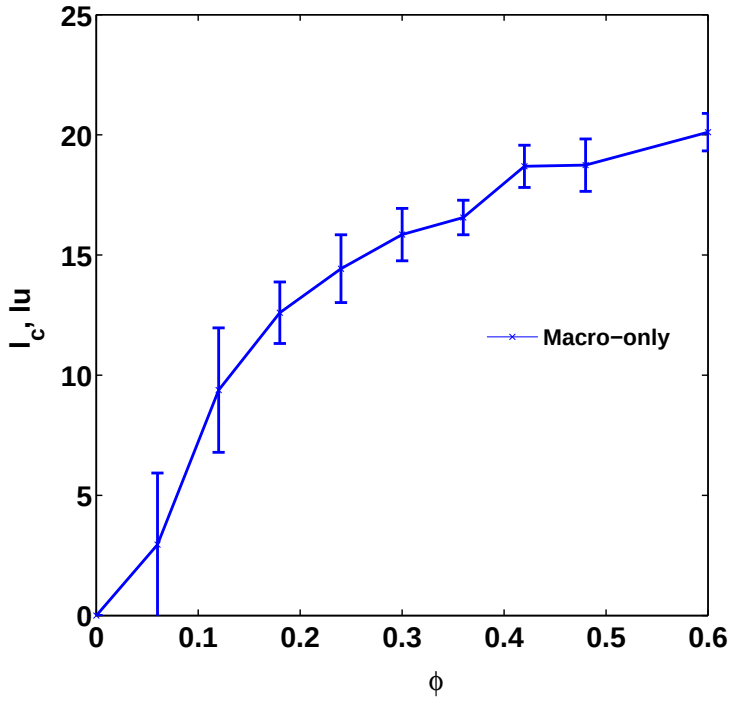

Figure 3.15: The relation between critical length and porosity for macro-phase in bimodal porous media with GRF fraction of 0.0, 0.2, 0.3 $\cdots$ 1.0.

bars show the standard deviation for 10 realisations at each GRF fraction. An interesting aspect of this figure is the intersection of the critical length curves for pure micro and macro-phase. Considering first the percolation properties of the individual components of the 4-phase composite, for porosities larger than this 52% (or a GRF fraction of the macro-porous phase of 20%), the critical length of the macro-phase is larger than that of the micro-phase, suggesting that permeability will start to be controlled by the macroporosity from this point. For the combined pore space (micro + macro) at a GRF fraction of about 50% ($\phi = 0.55$), the critical length of the system closely follows the critical length of the macro-phase, while for smaller porosities the critical length of micro-phase is expected to be the controlling parameter for flow. At porosity 0.51, for instance, the critical diameter of pore phase is about 9.43 lu which is closer to that of micro-phase ($l_c = 7.9\ lu$) rather than macro-phase ($l_c = 2.95\ lu$). As expected, the critical length of pore phase approaches the critical length of micro-phase at porosity 0.5 and macro-phase at porosity 0.6 (Fig. 3.16).

There are some important points about the critical length as follow:

- The conclusion drawn based on the characteristic length in 3.16 will still be true if the total porosity is low. However, image-based calculation of the critical diameter is limited by the resolution of the image.

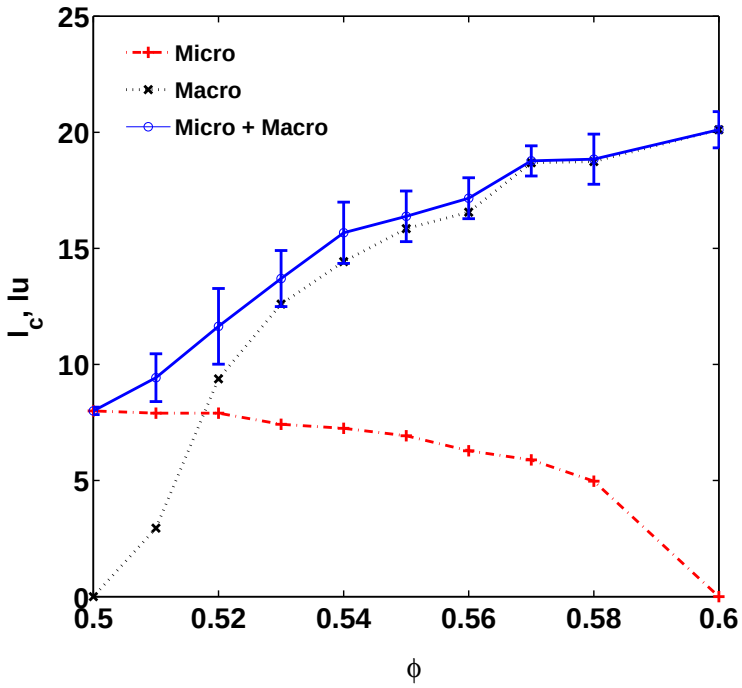

Figure 3.16: The significance of microporosity on fluid flow through critical length.

- Based on the definition of the critical length, mentioned earlier, the same concept can still be used when neither of macro- and micro-porosity percolate. In such a case, the critical length (diameter) and consequently the permeability of each individual pore type will be zero while for the pore phase (micro + macro), the combined critical length should be considered.

- Implementing the concept of critical length as a good estimate of permeability for showing the significance of microporosity is reasonable however, it remains qualitative. Below a flux analysis technique is described and implemented to quantify the effect of each pore type on fluid flow.

3.5.2 Flux analysis

To investigate the effect of micro-porosity on the fluid flow in the dual-scale porous media, the relevant flow equations combined with separate tracking of the fluxes in the different pore systems is considered. By definition, flux is the rate of flow of a property per unit area with a dimension of [quantity].[time]$^{-1}$.[area]$^{-1}$ [33]. Vector flux is defined as follows:

$$q = \int_{t_1}^{t_2} \oiint j \cdot \hat{n}\, dA\, dt\ , \tag{3.30}$$

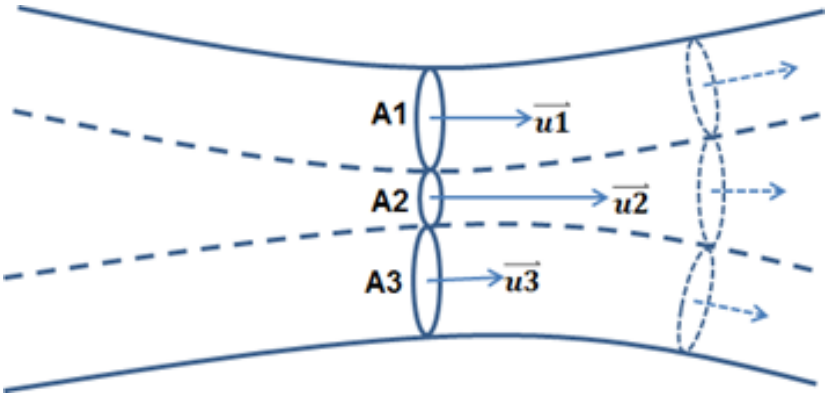

Figure 3.17: An illustration of procedure for volumetric flux.

where the surface integral of scalar flux j, over a surface, followed by an integral over the time duration t_1 to t_2, gives the total amount of the property flowing through the surface in the time $(t_2 - t_1)$. The result of this operation is simply called the surface integral of the flux. Here, we are more interested in volumetric flux which similarly accounts the amount of fluid flowing per second out of a volume element. It could be calculated by multiplying the fluid speed by the perpendicular area through which the fluid flows (Fig. 3.17).

Dividing the pore space into macro-pores and micro-pores, the total amount of the flux flowing through the pore space is the sum of the fluxes through these regions. It can be easily extended to account all phases existing in the region of interest. Having the local velocities at each elementary cell (voxels in 3D image), the average velocity through each region is given by:

$$u_l = \langle u(i,j,k,l) \rangle = \frac{1}{N_l} \sum_k \sum_j \sum_i u(i,j,k,l) \ , \tag{3.31}$$

where, subscript l refers to a specific region and N_l is the number of voxels constituting each region. With N_t = total number of voxels, the permeability can then be written as for incompressible fluids. The permeability of each region is calculated using Darcy law :

$$K_l = \frac{u_l \mu}{\nabla p} N_t \ . \tag{3.32}$$

Here, μ is dynamic viscosity and ∇p is the pressure gradient across the domain.

3.5.2.1 Microporosity significance through flux analysis technique

Analysing the results depicted in Fig. 3.16, help us to choose the right models for more quantitative investigation of the microporosity effect on the effective permeability. From 10 models explained above, four models D, E, F and G corresponding to GRF fraction of 0.2, 0.6, 0.8 and 0.9 respectively (see Tab. 3.2) were

Table 3.2: Results computed from LBM and following flux analysis technique on 3D heterogeneous model structures D – G (all permeabilities are reported in Darcy).

Models	Size	$K_{z0,micro}$	$K_{z0,macro}$	$K_{z,micro}$	$K_{z,macro}$	$K_{z,LBM}$	$K_{z,LBM}$ / $K_{z0,macro}$
D	400^3	0.033	5.011	0.269	5.45	5.719	1.14
E	400^3	0.309	1.16	0.651	1.901	2.552	2.20
F	400^3	0.534	0.183	0.777	0.752	1.529	8.36
G	400^3	0.686	0.031	0.829	0.331	1.16	37.4

selected for permeability calculation. It should be noted that, in all these models, not only percolating clusters exist in both microporosity and macroporosity, these two pore type are well interconnected.

We used label fields distinguishing micro- and macro-porous regions to analyze the local velocity fields obtained by the lattice Boltzmann method according to Eqn. 3.31. The computations were carried out on 10 realisations where the average values for permeabilities is given in Table 3.2. Micro and macro subscripts indicate two pore types whereas K_{z0} is the permeability of each pore type when the other is considered as impermeable. In the case of interconnectivity between micro- and macro-pores, $K_{z,micro}$ and $K_{z,macro}$ is calculated based on the flux tracking technique. $K_{z,LBM}$ is the summation of $K_{z,micro}$ and $K_{z,macro}$ and serves as "true solution" to be compared with results from MLBM described in chapter 5. As the fraction of microporosity increases, its effect on the whole permeability becomes more significant. For example, $K_{z,LBM}$ / $K_{z,macro}$ for model D is 1.05, while this ratio for model G increases to 3.5, highlighting the significance of microporosity in this model. Defining the percent error as:

$$\delta = \frac{K_{z,LBM} - K_{z,macro}}{K_{z,LBM}} \times 100 \ , \tag{3.33}$$

the exclusion of micropores in permeability calculation will result in errors of 12.38%, 54.45%, 88.03% and 97.33% for models D, E, F and G respectively.

The results are also shown in Fig. 3.18 where the significance of each individual pore type on the effective permeability is evident. Interestingly, permeability results shown in this figure for micro-, macro- and pore phase, which is the combination of micro and macro, is consistent with the results shown in Fig. 3.16 for critical length, highlighting the merit of critical length for permeability estimation.

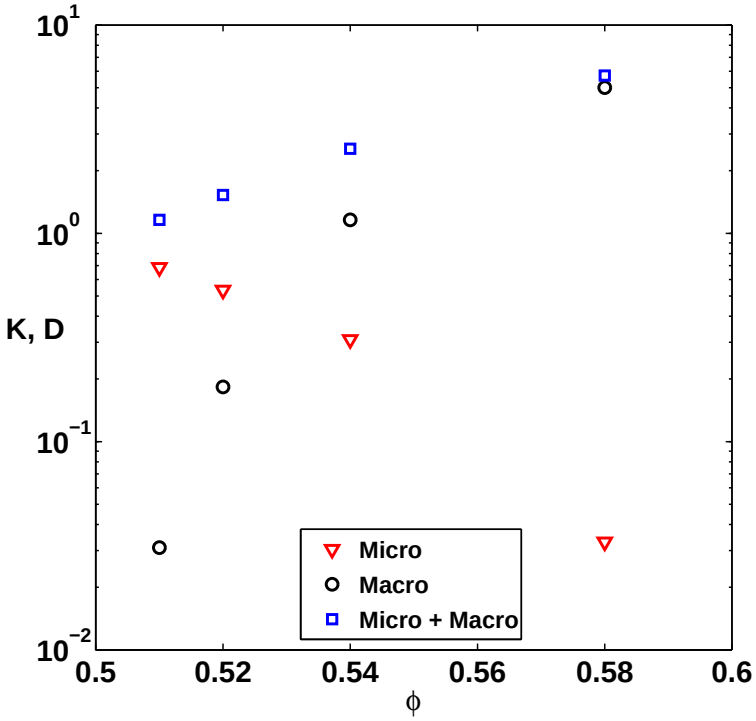

Figure 3.18: The significance of microporosity on effective permeability calculated by LBM and flux analysis technique for models D, E, F and G with total porosity 0.58, 0.54, 0.52 and 0.51, respectively.

CHAPTER 4

PORE SCALE MODELING: TWO PHASE FLOW

As an extension to single phase flow in the previous chapter, this chapter considers two-phase flow simulations. First, the experimental and the numerical techniques for mapping the saturation distribution in porous media are reviewed. A pore morphology-based approach, which was used for partially saturating the models, is then explained and implemented on some selected model structures. Finally, the significance of the effect of microporosity on the effective permeability of the wetting phase is investigated through critical diameter and permeability calculations.

4.1 Two phase fluid distribution in porous media

Simulating fluid flow in a complex geometry such as a porous medium is a non-trivial task particularly when multiple phases share the existing pore space. Much of this difficulty arises from the complex pore structure, rock-fluid and fluid-fluid interactions. In contrast to single phase flow properties, which are mainly controlled by the topology and morphology of the pore structure, multi-phase flow properties are also affected by the saturation of occupying fluids and how they are distributed in the pore space. At the reservoir scale, the physics of multiphase fluid flow is captured by introducing constitutive relations, relative permeability and capillary pressure curves, into the reservoir simulators. While the capillary pressure-saturation relationship defines the distribution of fluids in the reservoir, the effective permeability of each fluid at any particular saturation is controlled by relative permeability functions. At the pore scale level and especially for image-based fluid flow simulation, an accurate mapping of fluid phases is required as a crucial part in the pore scale modeling of multi-phase fluid flow. It is also essential for quantification and proper homogenisation of micro-phase, which is the ultimate goal of this thesis and is described in chapter 5.

With this in mind, experimentalists have tried to obtain a better insight into the pore scale physics of fluid distribution and modelers put many efforts

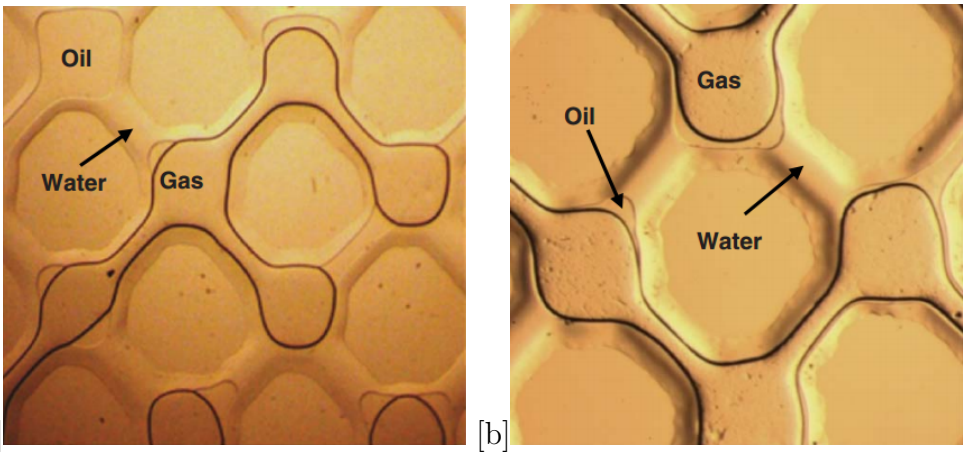

[a] [b]

Figure 4.1: Three-phase fluid distribution in strongly water-wet glass micromodel for [a] negative spreading coefficient and [b] positive spreading coefficient. (Fig. 1 from [57])

on simulating displacement processes at the pore scale to reproduce experimental observations.

4.1.1 Experimental imaging of multiple fluids in porous media

By constructing glass micromodels and performing different displacement experiments, [181, 131, 57] have attempted to visualize and better understand the processes which control the distribution of fluids in the pore space. [131] investigated the waterflood residual oil recovery after tertiary gas flooding for both positive and negative spreading coefficients. Similar experiments were performed by [57] and the results are shown in Fig. 4.1. Studying nonaqueous phase liquid (NAPL) movement [85, 207] and three phase capillary pressure-saturation relationship [181] is another example of the application of micromodels. Although simple, they helped to improve the theoretical background of current pore network models. Two dimensional light transmission methods (LTM) have also been used for studying multiphase flow in natural porous media [50]. Since both micromodels and LTM are in 2D, the connectivity of the pore network in 3D can not be captured. Computing relative permeability functions at the pore scale requires more quantitative representation of fluids distribution and their connectivity in porous media at 3D.

The emergence of 3D imaging techniques provided better visualisation of fluid distribution in porous media. [129] developed a photoluminescent volumetric imaging (PVI) technique to visualise and quantify multiphase flows and interface behaviour in a transparent porous medium system. By using laser scanning confocal microscopy (LSCM), [63] statistically characterised the microgeometry of both natural and engineered porous materials. More recent advances in X-ray computed

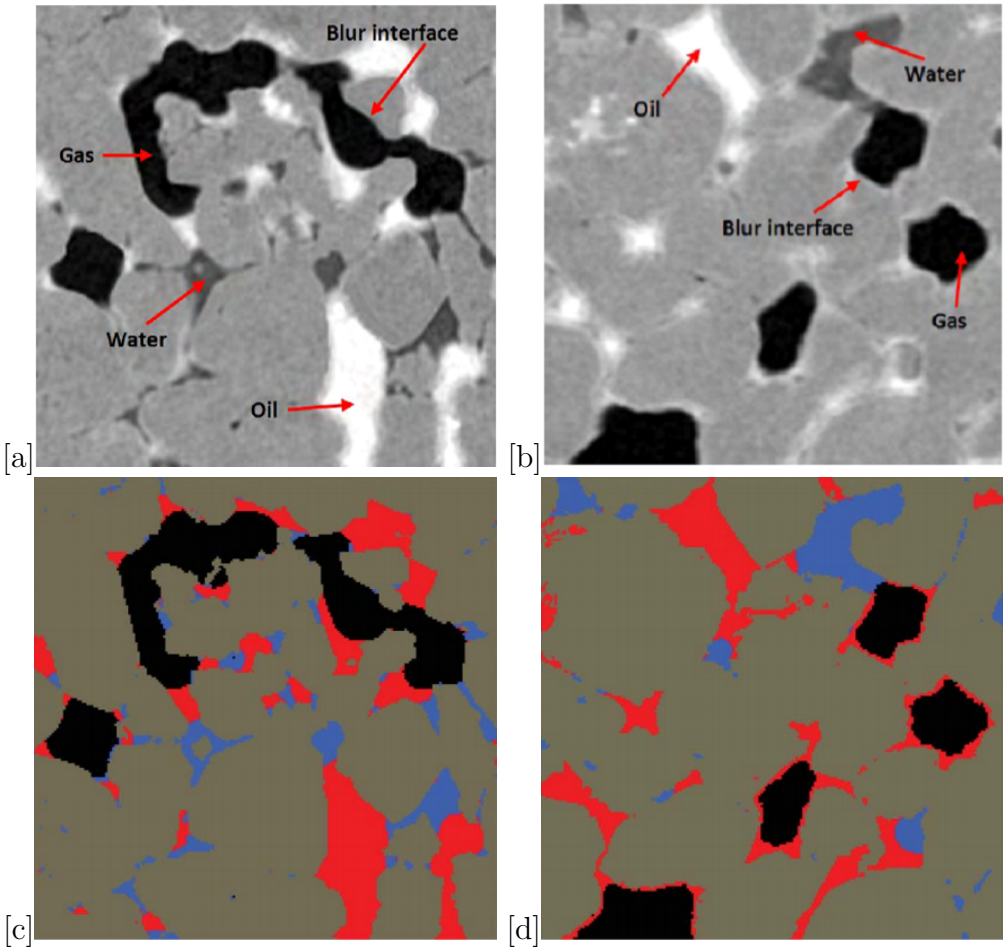

Figure 4.2: Sections of tomograms (top row) and segmented tomograms (bottom row) showing three-phase fluid distribution in Bentheimer sandstone for [a, c] negative spreading coefficient and [b, d] positive spreading coefficient. In segmented images, gas is shown in black, oil in red and water in blue. (Fig. 4-4 and Fig. 4-6 from [58])

tomography (CT), as the non-intrusive and non-destructive methods, received significant attention in the study of displacement processes mechanisms [52, 128] and various multiphase processes [45, 17]. Although these are promising, the poor resolution of CT images limit their application in quantitative analysis of multiphase fluid distribution in real rock materials. X-ray microtomography offers orders of magnitude higher resolution than CT and the potential of this technique for imaging multiple phases has been proven for sandpacks [4, 167] and more recently for some real rock materials [104, 103, 57]. Fig. 4.2, shows the distribution of three fluids in Bentheimer sandstone captured by μ-CT [57]. Having segmented the fluids into gas, water and oil, it is now possible to compute multiphase flow properties directly on the image.

4.1.2 Numerical modeling

Despite significant progresses in the field of experimental imaging, mapping of multiphase fluid distribution is not a trivial task and comes with some uncertainties. For example, in a three-fluid system of water, oil and gas and for a positive spreading coefficient (see Fig. 4.2), the oil phase forms a film between water and gas phase [57]. Resolving this oil film where its thickness is less than the resolution of the image is very difficult, if not impossible. In addition, to preventing disturbance to the capillary equilibrium of the system and consequently the distribution of the phases in the core prior to imaging, one needs to implement dynamic imaging of the steady state flow [79]. In this technique, the flow cell is mounted on the CT scanning set up where flooding and imaging are performed simultaneously.

The goal of this thesis is to develop a method to upscale relative permeability curves from the pore scale. Simulating fluid distribution is helpful, if one wants to understand how to upscale. As an alternative to the experimental methods mentioned above the modellers tried to simulate physical processes which control the fluid distribution in the porous media. In the following section, three numerical methods are briefly introduced.

4.1.2.1 Simulated annealing

After formulation of simulated annealing (SA) as an optimisation algorithm by Kirkpatrick and coworkers [93], this method has been used by some researchers to find the equilibrium distribution of fluid phases in porous media. Having an analogy with annealing processes in solids, simulated annealing provides a framework for optimising the properties of complex systems. Knight et al. implemented a SA technique to drive microscopic fluid distribution in porous media [99]. Based on the assumption that the interfacial free energy governs the distribution of the fluid phases, they determined the fluid phase distribution which corresponds to the minimum total interfacial free energy of the system. They used three numerical methods to determine the distribution of two phases (water vapor and liquid water) for a 2D pore space model acquired from a digitised thin section image of a rock. In the first two methods, all the pore space elements are either vapor or liquid elements where the initial total interfacial free energy includes only the solid/vapor or solid/liquid interfaces, respectively. At each time step, one vapor element is selected to be replaced by a liquid element or vice versa in such a way that the total interfacial free energy of the system is minimised. This procedure is repeated until the required saturation is obtained. Although simple, these methods could produce fluid distribution close to the equilibrium configuration. However, simplistic single

element algorithm in these two methods results in metastable configurations. The third method which was based on SA, showed to be a robust method for producing the minimum possible free energy configuration [99]. The SA method used by [99], was later extended to three dimensions to examine the distribution of water and air in the wet unsaturated sphere packs [177] and real sandstone pore spaces [30]. Recently, [142] implemented the SA technique for two distinct problems. A hybrid method was proposed for solving an inverse problem associated with the reconstruction of three dimensional microstructures from 2D SEM cross-sectional images. The reconstructed sphere packs generated by this methodology were then used for determining the fluid spatial distributions.

4.1.2.2 Pore morphology-based approach

Hazlett developed a network model for simulating drainage and imbibition processes by utilising an assemblage of inscribed spheres [74]. This heuristic approach was tested for reproducing capillary dominated displacements on mixed wet network models extracted from micro-images of real reservoir rock samples. An oil-water spatial distribution in a Berea sandstone, resulted from this approach, was exported into a lattice Boltzmann method for flow modelling. Although the simulation domain was quite small, the end-point oil relative permeability calculated on a sample of size 256^3 was in reasonable agreement with that measured on core-scale Berea samples of similar porosity.

In a similar work to [74], Hilpert and Miller developed a quasi-static method for simulating drainage in a porous medium [75]. Based on the concepts of mathematical morphology, this approach simulates the drainage curve in three consecutive steps: erosion, a connected component analysis and dilation. The method was used for simulating the capillary pressure curve of a random sphere pack, where the results were in good agreement with experimental data, especially in the horizontal part of the curve.

More recently, [144] proposed a novel application of the level set method [133, 170, 59] for accurate determination of critical curvature for throat drainage and pore imbibition. Through the solutions of the level set model equations for model porous media and imaged geometries of real rocks, [144] showed that this method can also handle the merging and splitting of multiple menisci, which is of particular importance in "snap-off" of the non-wetting phase at the pore level. While only asymptotic solutions were considered by [144], they argued that the model can be used for dynamic interface tracking. An algorithm developed by these researchers, called progressive quasi-static (PQS) algorithm, was later implemented by [171] to simulate drainage process in Fontainebleau sandstone and dolomite samples. The

fluid phase configurations were then used to compute relative permeability of each phase using a single phase LBM.

4.1.2.3 Lattice Boltzmann method

The ability of lattice Boltzmann methods to simply incorporate interfacial tension and surface tension has made them as an interesting choice for simulating fluid distribution in the porous media. The colour-gradient model [159, 71, 107] and Shan and Chen model [173, 174, 78] are the most used models for this purpose. Coles and co-workers [45] imaged a partially saturated sandstone rock at resolution of 30 μm using synchrotron X-ray tomography. The imaged fluid distribution compared with that simulated by lattice Boltzmann technique and a network model. A modified colour-gradient LBM was used to simulate the drainage process and the results showed an exceptional agreement with the imaged fluid distribution. Because of computational demand of LBM, the displacement process was carried out at capillary number of approximately $5 * 10^{-5}$ compared to $N_{Ca} = 4 * 10^{-7}$ in the laboratory experiments. For the network model, although the water saturation was lower than that observed in the experiment, the pore level fluid distribution was similar. [186] used a Shan-and-Chen multicomponent, multiphase LBM to simulate wetting and non-wetting phase configurations on the image of a porous medium composed of packed quartz sand grains. The results were then validated against data acquired from cone-beam X-ray microtomographic images for oil, water and air distributions, showing consistency for both macroscopic and microscopic scales.

4.1.2.4 Discussion

Applying simulated annealing for determining the spatial distribution of multiple phases is based on the assumption that those phases are in complete equilibrium. Although this may be reasonable at low saturations, it is impossible to simulate drainage and imbibition processes [30]. One possible solution for that could be the modification of the SA algorithm to account for the fluid movement and redistribution at the low water saturations [176]. Pore morphology-based approaches or random percolation models [135] proposed by Hilpert and Miller [75], have received a lot of attention for simulating spatial fluid distributions. They assume a strongly wetting system with no trapped or irreducible wetting phase. Although it overpredicts S_w in the range of high capillary pressure, a limitation that lattice Boltzmann does not have, it is less computationally expensive compared to the lattice Boltzmann method. Kumar tested the applicability of capillary drainage transform (CDT) algorithm, which is based on the Hilpert and Miller method, for

different carbonate and sandstones rocks [102]. CDT-based fluid distributions were also used to calculate the relative permeability curves on Berea sandstone [79]. The comparison with image-based calculations and a LBM showed an encouraging agreement. Here we adapt the pore morphology-based method for partially saturating the models.

4.1.3 Drainage simulation on digitised images

To set the saturation, one can use a range of distance maps and their thresholds, including Euclidean distance transform (EDT), covering radius transform (CRT) and capillary drainage transform (CDT). The Euclidean distance transform of a given phase assigns to each voxel of each phase the distance of that voxel to the nearest non-object voxel (Fig. 4.3a). The covering radius transform assigns to each voxel of a given phase the maximal radius of a sphere, which is completely contained in the same phase, and can cover the voxel under consideration (Fig. 4.3b). The capillary drainage transform assigns similarly to the CRT to each voxel the largest radius of a sphere which can cover it. However, an additional condition is that the covering sphere must be able to reach the voxel of the interest from the inlet, moving through the same phase (Fig. 4.3c).

We implement the concept of CDT, described by [75] for simulating the drainage process. The process is similar to a mercury intrusion capillary pressure (MICP) test [53], in which capillary pressure is increased step by step allowing invasion of smaller pores by non-wetting phase. On the digitised image, however, the intruding elements are generally spheres whose diameter are related to the capillary pressure via Young-Laplace equation given by:

$$P_c = \frac{4\sigma}{d_s} \,, \tag{4.1}$$

where P_c is the capillary pressure, σ is the interfacial tension and d_s is the diameter of the intruding sphere. At each step, the volume of overlapping spheres represent the non-wetting phase saturation at that capillary pressure. As capillary pressure increases or the diameter of intruding spheres decreases, more wetting phase is drained out by invading non-wetting phase, resulting in an increase in the non-wetting phase saturation.

Fig. 4.3d, depicts an example of this process for one saturation point where pores with CDT value greater than four voxels are invaded by non-wetting phase, shown in white colour. Reducing the radius of intruding sphere will result in invasion of smaller pores in the next steps. The same procedure was followed for partially saturating the porous media in this study.

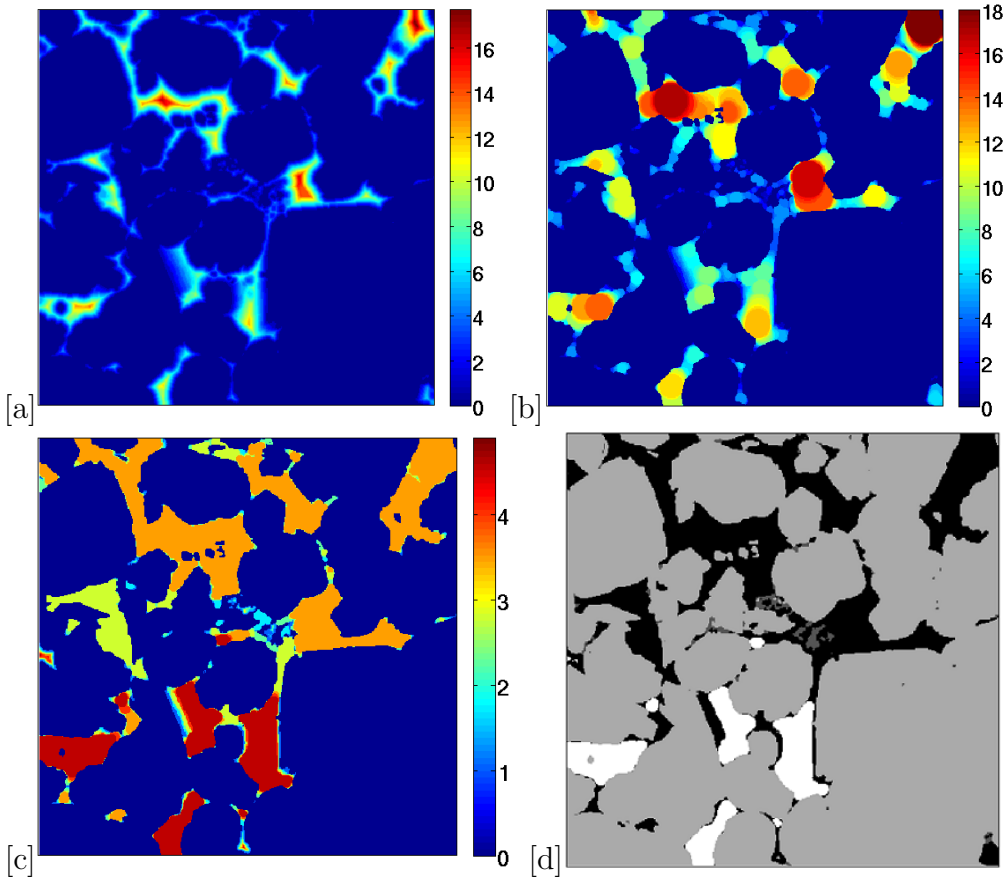

Figure 4.3: 2D cross-sections of different distance maps calculated on an image of Bentheimer sandstone: [a] Euclidean distance transform (EDT), [b] Covering radius transform (CRT) and [c] Capillary drainage transform (CDT). [d] An example of drainage process simulation in which all pores with CDT values greater than four voxels have been drained by non-wetting phase (shown in white). All models are discretised on 400^3 lattice with voxel size of 2.9 μm.

4.2 Relative permeability calculation

Of particular interest to this study is the examination of the effect of micro-porosity on the relative permeability functions. Similar to single phase flow, lattice Boltzmann method has received much attention for two-phase flow simulation at the pore scale. Both color gradient models [69, 71, 152, 159] and Shan-Chen models [78, 116, 134, 173, 174] showed an excellent capability for this purpose but come with an intensive computational cost. The other difficulty for applying multiphase LBM is choosing the right initial conditions for distributing the fluids in porous media. Simulating the spatial distribution of fluids requires pore scale information of wettability, as a priori knowledge; a condition which has not been satisfied so far at least for mixed-wet conditions.

A significant simplification for calculating relative permeability is to consider

only one phase flowing at a time and to assume the other phases immobile. In other words, for a two-phase fluid system consisting of water and oil, for example, when we solve for permeability of water phase, the oil phase is considered as solid phase and vice versa. By doing this for each phase, one can follow the same methodology outlined earlier for single phase LBM in calculating absolute permeability. This procedure is then repeated sequentially for all phases to calculate the relative permeability curves [66, 82].

As mentioned in the previous section, we simulate the drainage process for partially saturating the model structures. At each saturation point, the single phase LBM is run for wetting and non-wetting phase separately. The effective permeability of phase i, $k_{e,i}$, is obtained from Darcy's law:

$$k_{e,i} = -\frac{\mu_i \langle u_i \rangle}{\langle \nabla p \rangle} , \qquad i = w, nw. \tag{4.2}$$

Again here μ is the dynamic viscosity, u is the local velocity calculated from LBM and p is the pressure. The relative permeability of phase i, $k_{r,i}$, is then calculated by dividing the effective permeability, $k_{e,i}$, by the absolute permeability, K:

$$k_{r,i} = \frac{k_{e,i}}{K} . \tag{4.3}$$

4.3 Heterogeneous porous media

In section 3.5, the effect of microporosity on single phase fluid flow in bimodal porous media was investigated using model structures. Ten models with GRF fraction of 0.0, 0.2, 0.3, $\cdots$, 1.0 with 10 realisations for each model were made and the contribution of microporosity to fluid flow was studied by measuring the critical diameter of the pore space in both micro and macropore regions. Using 3D heterogeneous models built for single phase flow, in this section we show the significance of the microporosity on the effective permeability of the wetting phase for the whole range of saturation. A drainage process is simulated for distributing the wetting and the non-wetting phase.

4.3.1 Drainage process simulation

For two phase flow simulations, seven models with different GRF fractions were selected including GRF0 and GRF100, as pure macropore and pure micropore model respectively and GRF50, GRF60, GRF70, GRF80 and GRF90. Again for each GRF fraction, 10 realisations were considered. As detailed earlier in section 4.1.3, different threshold values were applied to the CDT map of the pore phase to acquire specific saturations. Fig. 4.4 shows an interface of GRF0 and GRF100 in

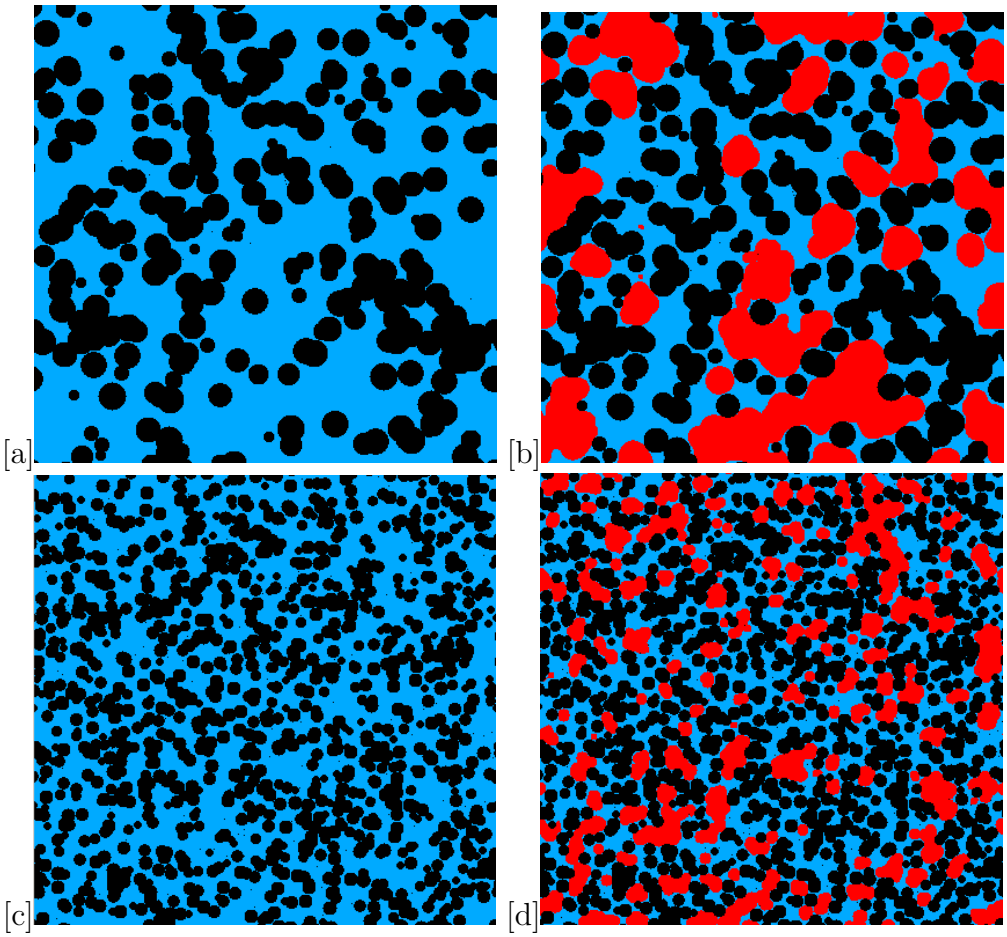

Figure 4.4: 2D cuts through 3D model structures of GRF0 and GRF100 corresponding to pure macropore and pure micropore, respectively. Solid is black and wetting and non-wetting phase is shown blue and red. [a] GRF0 in completely saturated state and [b] partially saturated state ($S_w = 0.73$). [c] GRF100 in completely saturated state and [d] partially saturated state ($S_w = 0.88$).

totally and partially saturated state where black, blue and red colours correspond to solid, wetting and non-wetting phase, respectively. For partially saturating GRF0 and GRF100 model, we start from totally saturated model (Fig. 4.4a and Fig. 4.4c) and by increasing the capillary pressure sequentially, the non-wetting phase is invading into the model. Fig. 4.4b and Fig. 4.4d correspond to $S_w = 0.73$ and $S_w = 0.88$ on GRF0 and GRF100, respectively.

In contrast to model GRF0 and GRF100, in which only one pore type exists, two pore types coexist in GRF50-GRF90. Fig. 4.5 shows an interface of model GRF70 in two saturation states. While the underlying one-level cut GRF controls the distribution of micropore and macropore regions, the drainage process is simulated on the 2-phase structure (Fig. 4.5a) where solid phase is in black and pore phase is in blue. As can be seen in Fig. 4.5b, which corresponds to $S_w = 0.57$, the

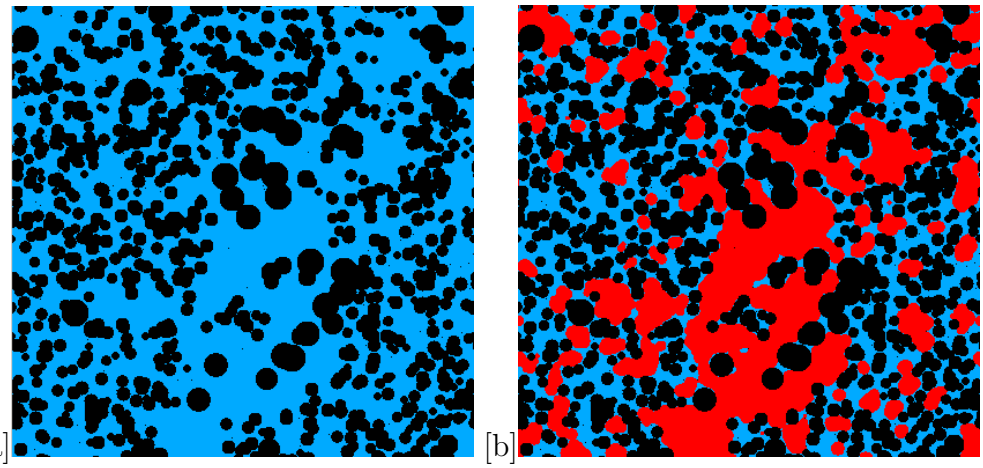

Figure 4.5: 2D cross-sections of 3D representations of model GRF70 in two saturation states. [a] $S_w = 1.0$ and [b] $S_w = 0.57$. Black is solid, blue is wetting phase and red is non-wetting phase.

non-wetting phase first occupies the macropores and then the larger pores in the microporous region.

4.3.2 Microporosity significance through critical diameter analysis

By using the concept of the characteristic length, the effect of microporosity on the effective absolute permeability was shown in section 3.5. Similar to single phase fluid flow, the critical length of wetting phase and non-wetting phase is separately calculated at each saturation on partially saturated models to show the significance of microporosity. As shown in Fig. 4.4b and Fig. 4.4d, models were partially saturated and then at each saturation the critical length was calculated for both wetting and non-wetting phase. This procedure was repeated for all 10 realisations of each GRF model. Fig. 4.6 shows the relation between the critical length and saturation for seven model structures. The error bars in this figure correspond to the standard deviation in calculated l_c at each saturation point. As can be seen, the error associated with $l_{c,nw}$ is more than that for $l_{c,w}$ for the whole range of saturation. The reason for this has been shown in Fig. 4.7 by schematic representation of critical length-saturation relationship for ten realisations. The dashed, blue rectangle in this figure specifies the averaging window at $S_w = 0.5$ where a large variation in percolation threshold is observed among different realisations.

Analysing the results shown in Fig. 4.6 reveals some interesting points. In pure macropore model, GRF0, the maximum value of l_c for both wetting and non-wetting phase is 20 lu (Fig. 4.6a), which coincides with the maximum l_c in Fig. 3.15 for macro-only systems. Similarly, for GRF100 as pure micropore model, the maximum l_c is 8 lu (Fig. 4.6g), which again agrees with that in Fig. 3.14 for

micro-only system. As the fraction of microporosity increases, the maximum l_c for both wetting and nonwetting phase decreases from 20 lu in GRF0 to 8 lu in GRF100. Another interesting point in Fig. 4.6a-f is the inflection point of curve $l_{c,w}$, which corresponds to maximum l_c for pure micropore model (Fig. 4.6g). While in model GRF0, the inflection point is hardly distinguished, it is clearer for models with higher fractions of microporosity. In addition, the intersection of $l_{c,w}$ and $l_{c,nw}$ for GRF0 and GRF60 is well beyond the inflection point, highlighting the reduced significance of microporosity for these models compared to GRF70, GRF80 and GRF90 where the inflection point is shifted to the right of the intersection.

Fig. 4.6, shows a combined effect of micropore and macropore on wetting and non-wetting phase flow property. Of particular interest to this study is to investigate the significance of microporosity on the relative permeability of the wetting phase. To do this, at each saturation the volume fraction of the wetting phase in micropore and macropore needs to be determined separately before calculating the effective permeability of wetting phase in these regions. The following procedure was devised to decouple the wetting phase saturation in micro- and macropores:

- The CDT map of the pore phase was calculated on the 2-phase structure (Fig. 4.8 a, d).
- Different threshold values were then put on the CDT map while constrained by the 4-phase structure (Fig. 4.8 b, e) in which the boundary of micropore and macropore region was defined by one-level cut GRF model.

While the threshold value sets the invasion of the non-wetting phase, the provided 4-phase structure defines the distribution of the wetting phase and non-wetting phase in the micropore and macropore regions. As depicted in Fig. 4.8, this procedure assigns five labels to the five phases in the partially saturated models. Solid phase is in black and the non-wetting phase is red in both micro- and macropore region. The wetting phase in the micropore and macropore is dark blue and light blue, respectively. Fig. 4.8 shows two different realisations of GRF70. Realisation A, on the top row, is partially saturated to $S_w = 0.57$ where the above procedure shows $S_{w,micro} = 0.52$ and $S_{w,macro} = 0.05$. For realisation B, at the bottom, the total water saturation is $S_w = 0.83$ while $S_{w,mciro} = 0.63$ and $S_{w,macro} = 0.2$.

The above procedure was followed for all realisations of GRF50, GRF60, GRF70, GRF80 and GRF90. The results are summarised in Fig. 4.9 in which the volume fraction of the wetting phase is normalised by the total porosity and plotted against the critical length of the wetting phase. Shown in this figure, as the fraction of microporosity increases from GRF50 to GRF90, the difference between micro and macro becomes more evident. Except for GRF50 and only for

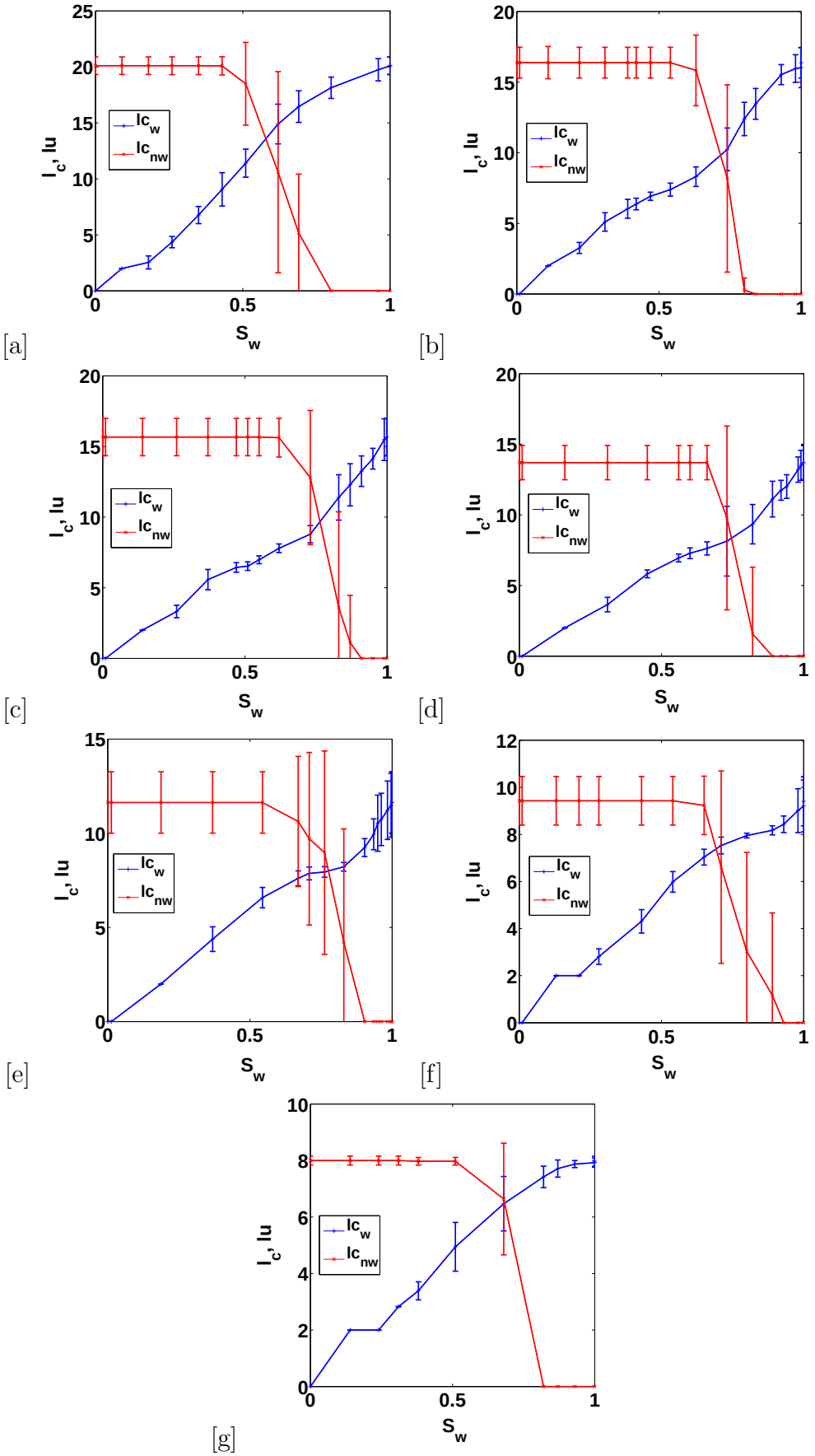

Figure 4.6: The relationship between critical length and wetting phase saturation for different heterogeneous model structures including: [a] GRF0 which corresponds to pure macropore, [b] GRF50, [c] GRF60, [d] GRF70, [e] GRF80, [f] GRF90 and [g] GRF100 corresponding to pure micropore.

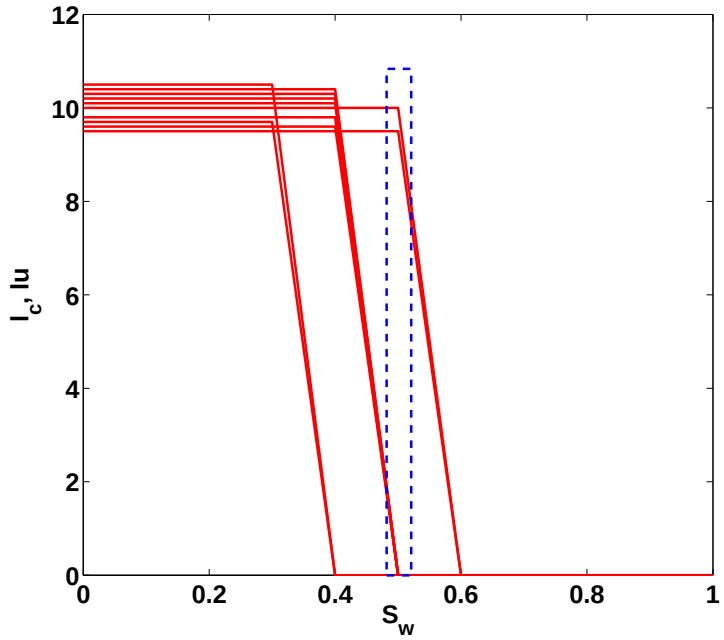

Figure 4.7: Schematic representation of large variations in the critical length of non-wetting phase near the percolation threshold.

$l_{c,w} > 13.5$ in which the volume fraction of the wetting phase in macro is more than that in micropore region, for all other models the wetting phase is largely stored in the micropore for the whole range of $l_{c,w}$. In GRF50, GRF60 and GRF70 corresponding to Fig. 4.9 a, b and c respectively, the volume fraction of the wetting phase in macropore continuously increases with $l_{c,w}$, while it reaches to a plateau in micro at $l_{c,w} = 8lu$. As detailed before for single phase flow simulation, $l_{c,w} = 8lu$ is the critical length of the pure microporosity system. The effect of micropores is dominating significantly in GRF80 and GRF90, resulting in near zero volume fraction of wetting phase in macropore for $l_{c,w} < 8lu$. Fig. 4.9 clearly shows that the volume fraction of the wetting phase in micropore region is by far larger than that in macropores especially for $l_{c,w} < 8lu$. In addition, the variation in calculated ϕ_w/ϕ_t for macropore is bigger than that for micropore, especially for GRF50 and GRF60.

Knowing the distribution of the wetting phase in micro and macropore, we are now able to calculate the effective permeability of the wetting phase in each of these regions, using flux analysis technique described in section 3.5.2.

4.3.3 Microporosity significance through flux analysis technique

Using flux analysis technique, the total flux of the wetting phase computed on the pore space was post processed to obtain the contribution of each region

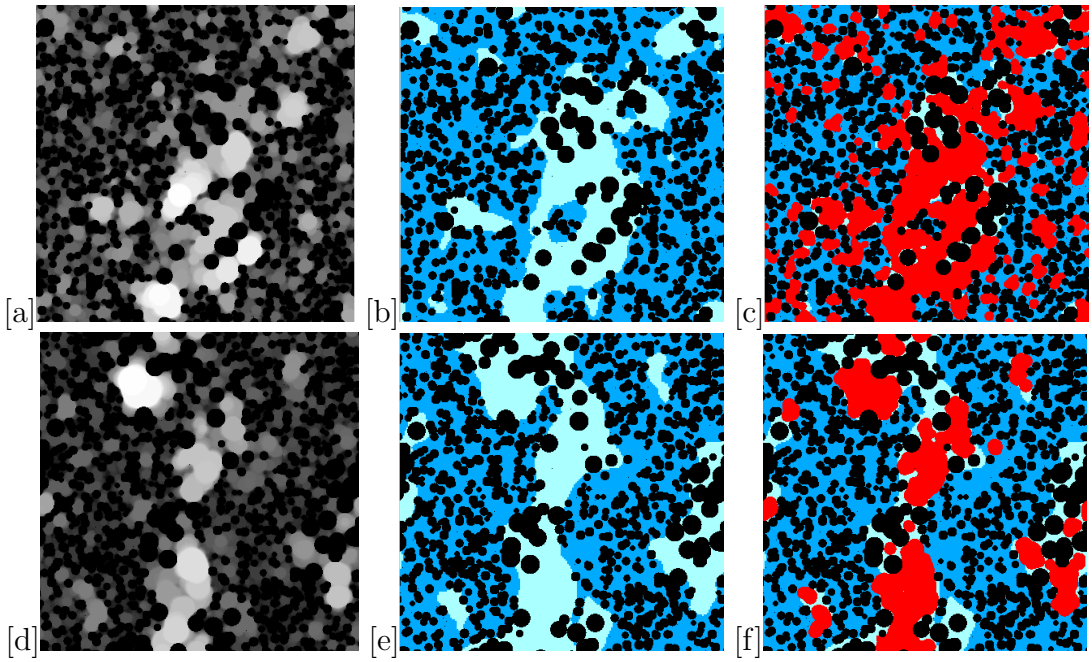

Figure 4.8: A snapshot of the procedure devised for decoupling the wetting phase saturation in micropore and macropore for two different realisations and saturations of GRF70 (realisation A on the top row and realisation B at the bottom). CDT map of pore phase calculated on 2-phase structure for [a] realisation A and [d] realisation B. Solid phase is in black and the grey colour shows the CDT values. White colour corresponds to the maximum CDT value. The 4-phase model structure of [b] realisation A and [e] realisation B. 5-phase partially saturated model of [c] realisation A and [f] realisation B. Solid phase is black and the non-wetting phase is red in both micro- and macropore region. The wetting phase in the micropore and macropore is shown in dark blue and light blue, respectively. All models are discretised on 400^3 lattices.

(micropore and macropore). The calculations were performed on 10 realisations of each GRF model and the average results are reported in Tab. 4.1. The semi-log plot of the effective permeability versus total saturation of the wetting phase for five GRF models is shown in Fig. 4.10. At each saturation point, the LBM was used to solve the Stokes equations and obtain the velocity field and consequently to calculate the effective permeability of the wetting phase. As described above, wetting phase in micro and macropore was indicated with different labels and the post processing of the total flux resulted in the effective permeability of the wetting phase in micro and macropore region. Again as the fraction of the microporosity increases, its effect on the effective permeability of the wetting phase increases. For GRF50 at $S_w > 0.65$, for instance, the macropore is dominating and $k_{w,macro} > k_{w,micro}$ while for GRF60 and GRF70 it happens at $S_w > 0.75$ and $S_w > 0.85$, respectively (Fig. 4.10 a, b and c). For GRF80 and GRF90, the effective permeability of the wetting phase in micro is higher than that in macro for the whole range of saturation (Fig.

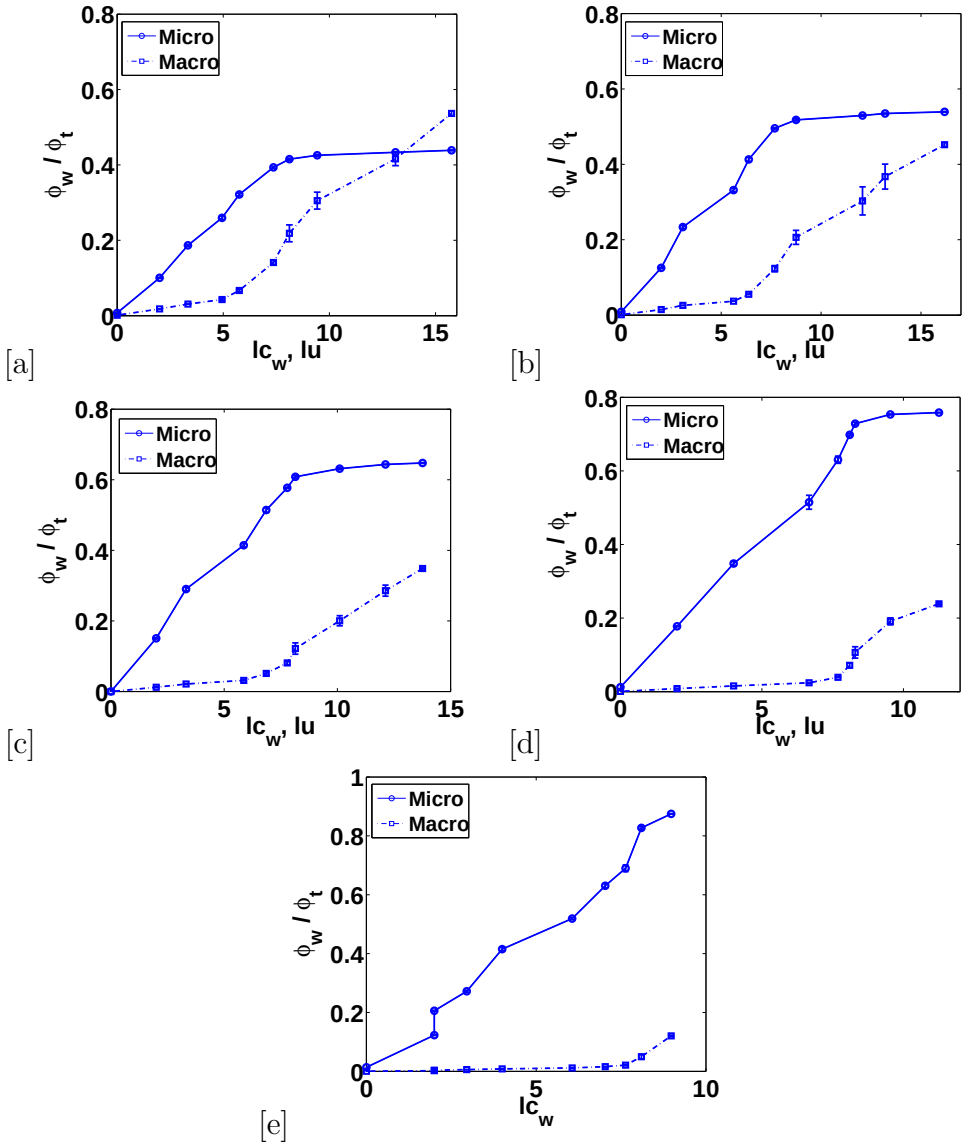

Figure 4.9: The relationship between the volume fraction and critical length of the wetting phase in micro- and macropore region for models [a] GRF50, [b] GRF60, [c] GRF70, [d] GRF80 and [e] GRF90. The error bars show the standard deviation in the calculated ϕ_w/ϕ_t among different realisations.

4.10 d and e). Although the effect of microporosity on the effective permeability of the wetting phase is more significant in GRF70, GRF80 and GRF90, its effect in GRF50 and GRF60 is not negligible, especially at lower saturations.

Another point which is worth paying attention to in Fig. 4.10, is the variation of the calculated effective permeabilities at each saturation for micro and macropore region. The error bars show the standard deviation in $k_w(S_w)$ for 10 realisations of each GRF model and as can be seen it is much smaller for wetting phase in micropore compared to macropore. This again could be partly related to the REV concept and shows that we are closer to an REV in the micropore region compared to the macropore region.

4.4 Discussion

As the significance of the microporosity increases, the error associated with its exclusion in the permeability calculation increases. Defining percent error as:

$$\delta = \frac{k_{w,LBM} - k_{w,macro}}{k_{w,LBM}} \times 100 \ , \tag{4.4}$$

where $k_{w,LBM}$ is the effective permeability of the wetting phase and $k_{w,macro}$ is the effective permeability of the wetting phase in the macropore only, one can quantify the error resulting from the exclusion of the microporosity. Fig. 4.11 shows this error as a function of total saturation for model structures GRF50 to GRF90. As expected, at higher saturations of the wetting phase the error is smaller, meaning that at higher saturations the effect of microporosity on the effective permeability of the wetting phase is less significant. However, it should be noted that, even for GRF50 and at $S_w > 0.9$, the error is more than 20 %. This increases to more than 50 % in GRF80 and more than 70 % in GRF90.

Table 4.1: The significance of the effective permeability of the wetting phase in micropore on the total effective permeability of the wetting phase for five partially saturated model structures. $k_{w,LBM}$ is the effective permeability of the wetting phase which is a combination of $k_{w,mic}$ and $k_{w,macro}$.

	S_w	$k_{w,LBM}$	$k_{w,mic}$	$k_{w,mac}$
GRF50	0.12	0.0000	0.0000	0.0000
	0.30	0.0342	0.0342	0.0000
	0.39	0.0893	0.0866	0.0027
	0.54	0.2518	0.2056	0.0462
	0.63	0.4532	0.2830	0.1702
	0.73	0.8442	0.3606	0.4836
	0.85	1.6684	0.4602	1.2082
	0.98	2.8820	0.5620	2.3200
GRF60	0.14	0.0000	0.0000	0.0000
	0.26	0.0053	0.0053	0.0000
	0.47	0.1497	0.1444	0.0053
	0.62	0.3563	0.3030	0.0533
	0.83	1.2329	0.4960	0.7369
	0.99	2.5702	0.6442	1.9260
GRF70	0.16	0.0000	0.0000	0.0000
	0.45	0.0870	0.0865	0.0005
	0.57	0.2267	0.2142	0.0125
	0.73	0.5351	0.4273	0.1078
	0.83	0.8852	0.5434	0.3418
	1.00	1.9872	0.7272	1.2600
GRF80	0.19	0.0000	0.0000	0.0000
	0.36	0.0221	0.0221	0.0000
	0.54	0.1632	0.1608	0.0024
	0.67	0.3531	0.3396	0.0135
	0.83	0.7177	0.5818	0.1359
	1.00	1.4952	0.7852	0.7100
GRF90	0.21	0.0000	0.0000	0.0000
	0.42	0.0332	0.0332	0.0000
	0.53	0.1089	0.1080	0.0009
	0.71	0.3658	0.3544	0.0114
	0.88	0.7068	0.6386	0.0682
	1.00	1.1396	0.8332	0.3064

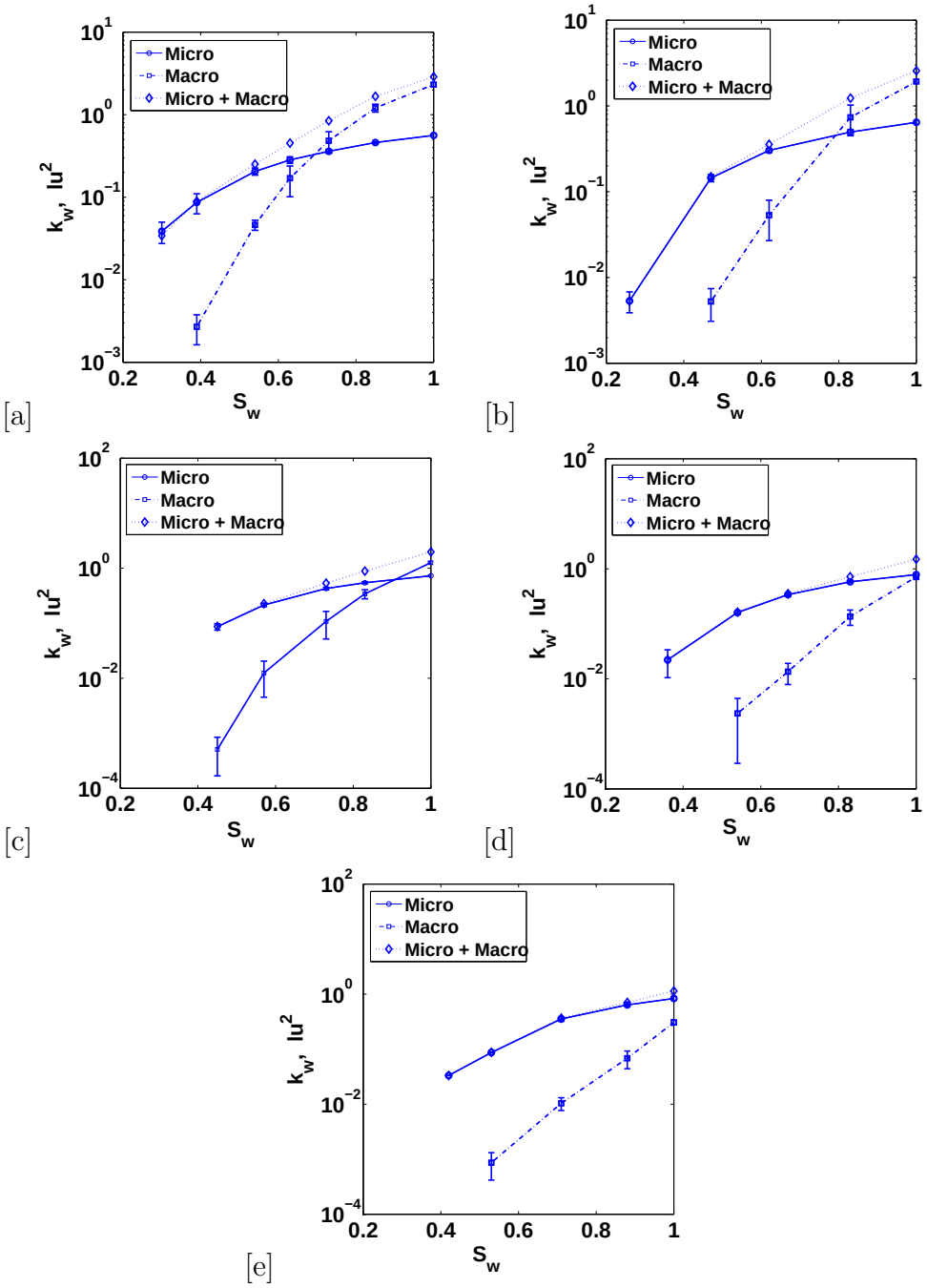

Figure 4.10: The significance of the effective permeability of the wetting phase in micropore on the total effective permeability of the wetting phase for five partially saturated model structures [a] GRF50, [b] GRF60, [c] GRF70, [d] GRF80 and [e] GRF90. The standard deviation in effective permeability at each saturation is shown by error bars.

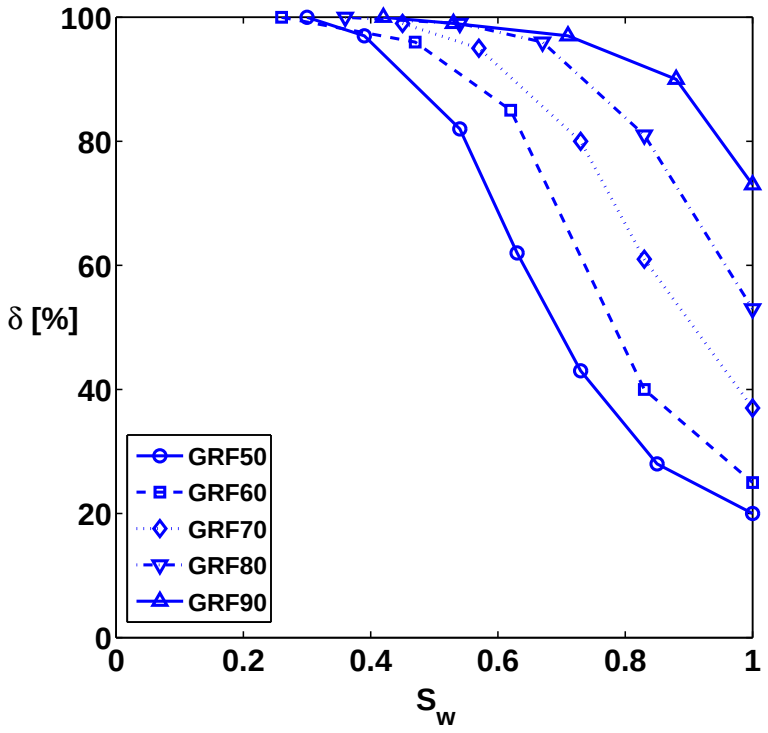

Figure 4.11: The relative error associated with the exclusion of the microporosity for calculating the effective permeability of the wetting phase in five GRF models.

CHAPTER 5

UPSCALING

In this chapter, upscaling from the pore scale is briefly introduced followed by a description of a macroscopic lattice Boltzmann method (MLBM) as the main approach for upscaling in this thesis. The method is first applied for single phase flow on 2D, homogeneous and heterogeneous model structures before extending it to 3D and heterogeneous porous media. For two-phase flow simulations, MLBM is used for coupling an average effect of wetting phase in micropores with an explicit representation of wetting phase in macropores. Finally, the results of MLBM are compared with those obtained from a pore scale Laplace approach for testing direct approaches against homogenisation of the microporosity regions.

5.1 Background

5.1.1 Upscaling from the core scale and beyond

Data from core analysis in conjunction with formation properties from log, seismic interpretation and well test analysis is used to populate geological models. Building a geological model with grid size of a core plug might be possible but is not practical. For some reservoirs, these models could reach several millions of grid blocks to capture the heterogeneities of the reservoir. Recent advances in computational resources have made it possible to perform some calculations such as oil in place and even some single phase fluid properties on detailed geological models. However, simulating multiphase flow on these models, which is of particular interest in production from hydrocarbon reservoirs, could be unreasonably expensive [121]. Therefore, it is necessary to coarsen the grid blocks in reservoir simulation model. It should be done in a way that the coarse grid model could reproduce the results of fine grid models. This process of transforming the data between different scales is referred to as "upscaling".

The ultimate aim of upscaling is to capture the flow using fewer grid blocks. The difficulty of the process could vary from simple averaging for some scalar properties such as porosity and net-to-gross ratio to more sophisticated mathematical

procedures for non-additive properties such as absolute permeability, relative permeability and capillary pressure. Compared to relative permeability and capillary pressure, upscaling the single phase flow properties is more straightforward and many works have been devoted to this. For example, pressure solver methods [25, 55], renormalisation techniques [92] and effective medium theory have been used for this purpose. In upscaling multiphase flow properties, the aim is to derive effective or pseudo relative permeability and capillary pressure curves for each phase in coarse grid blocks. By this, the effect of fine grid variations on the coarse grid flow is preserved. Like single phase flow, multiphase flow upscaling is still a very active research topic but most of the studies in the literature (see e.g. reviews by [198, 153, 44] for single phase flow and [21, 56, 140] for two phase flow) only consider the upscaling from the geological model to reservoir simulation model which is out of the scope of this work. Instead we are interested in upscaling from the pore scale to the core scale.

5.1.2 Upscaling from the pore scale to the core scale

Upscaling from the pore scale is a relatively new research topic, mainly because the pore scale modeling is still in its infancy. Similar to upscaling from the core scale to reservoir model, the process involves a broad range of scales; making the problem more complicated. This task is very critical in the context of "digital core analysis" where optimising the field of view is constrained by the system resolution. In other words, one prefers to have a high resolution image of a core plug (1.5 in. diameter and 2.0 in. length), in which all pore space is resolved. Even though it is possible, computing flow and transport properties on such a big model is not practical for uncertainty analysis. In an attempt to address this problem, [90] acquired high resolution images (voxel size = 2.75 and 3.57 μm) of 4 mini-plugs drilled from a core plug (imaged at resolution of 25.96 μm). The porosity and permeability computed on the image of these mini-plugs was then used to populate the image of the core plug using different interpolation and stochastic simulation techniques. Having a well-defined local permeability field of the core plug, the effective absolute permeability was then computed by upscaling through the solution of Laplace equation. The same procedure was applied for upscaling formation factor and the results were compared with some averaging and renormalisation techniques.

Implementing dual-scale pore network models is another approach which has been proposed to bridge pores at different length scales. Using information estimated from tomographic images, [125] modeled a vuggy carbonate for which relative permeability curves were computed. In a recent study, [123] proposed a dual-scale pore network model and studied the effect of micro-porosity on capil-

lary pressure-saturation relationship of tight gas sandstone. The model was later used for determining the permeability of the shale gas matrix [122]. In contrast to conventional pore network models, in these models the macropore network is augmented with networks representing microporous regions. While the macropore network is extracted based on resolved pores, the physical size of the microporous network is tuned to preserve the estimated pore volume [123].

Despite remarkable contribution of the above mentioned studies in transforming the data from the pore scale to the core scale, the problem of upscaling single phase and in particular multiphase flow properties deserves more investigations. In this thesis we use a special class of LB as a direct numerical simulation method to couple the information from two different length scales. In this approach, an explicit representation of sub-resolution pores is not required, but the permeability of the microporous region is preserved.

5.2 Macroscopic lattice Boltzmann method

Despite all advantages standard LBMs have, they require an explicit characterisation of porous structure in terms of pore and solid nodes. In other words, one needs a Boolean representation of the pore structure, where each pixel/voxel is labeled as either pore or solid; a prerequisite condition which may not be always satisfied.

X-ray imaging, as a non-destructive technique, provides 3D representation of porous media at finite resolution. Moreover, bimodal or multi-modal pore size distributions in some sedimentary rocks, result in the phase segmentation process being difficult and uncertain. Constrained by system resolution, the pore space is partitioned into macro-pores (resolvable pores), and micro-pores which are smaller than the resolution of the image. This partitioning procedure leads to a three-phase identification, in which macropore and macrosolid phase are separated explicitly whereas regions with ambiguous intensity are considered as an intermediate phase [68, 180]. Due to this limitation, the Boolean representation of the porous media is impossible and not desirable for fluid flow simulation using standard LBMs. To address this problem researchers have proposed alternative approaches, classified here as macroscopic lattice Boltzmann method (MLBM) and gray lattice Boltzmann method (GLBM). Despite major differences these two categories have, a common aspect of both is their capability of handling gray nodes in addition to black and white nodes.

In GLB methods, also named partial bounce-back, a volume fraction of net fluid particles is bounced back at each node. A model parameter, n_s which depends

on local permeability and fluid viscosity, controls the amount of fluid particles, δf, to be reflected back. This idea first developed for lattice gas (LG) by [18, 67]. Thinking of porous media as a collection of obstacles to fluid flow, [18] introduced a random distribution of fixed point scatters into flow. They tried to obtain an effective Darcys law by modifying Navier-Stokes equations through the introduction of a damping term. The permeability was related to the density of the scatters. Later, Gao and Sharma proposed a LG model for simulating fluid flow in heterogeneous porous media. By distributing scatters of solid nodes based on a fixed scattering node model and a probabilistic model, isotropic, anisotropic, random and correlated permeability fields were generated. They showed that by varying the probability of occurrence of solid particles, the effective permeability of the medium could change over orders of magnitude [67].

Inspired by these works on LG, Dardis and McCloskey extended it to lattice Boltzmann methods [48, 49]; avoiding the inherent statistical noise associated with LG. Using a multicomponent model, Thorne and Sukop [189] proposed another partial bounce back scheme and solved Elder problem, as a benchmark problem in solute-induced buoyancy flow. In contrast to Dardis and McCloskey, in which 'δf' takes the post streaming distribution functions, this method uses post-collision distribution functions in defining the partial bounce back term, $n_s \delta f$. Using post collision and pre-collision distribution functions in defining δf , [196] proposed another GLB method. They compared their model with [48] and [189] and showed that these two models are not mass conservative in heterogeneous media. Most recently, [208] introduced another GLB method, arguing more stability compared to Walsh et al. model. They presented a comprehensive review of GLB methods and proposed a procedure for estimating the model parameter, n_s; a key issue in applying these models for real porous media.

The macroscopic lattice Boltzmann method (MLBM) differs from GLB in the way it handles gray nodes. A dissipative forcing, applied either through the equilibrium distribution function [182] or the body force term in the standard lattice Boltzmann method [115], results in momentum reduction at gray nodes. This approach is the focus of this research and has been proven to be able to recover Darcy-Brinkmans equations or generalised Navier-Stokes equations [64, 83, 182]. The Brinkman equation is as follows:

$$\langle \nabla p \rangle = -\frac{\mu}{k} \langle \mathbf{u} \rangle + \mu_e \nabla^2 \mathbf{u} \, , \tag{5.1}$$

where $\langle \mathbf{u} \rangle$ denotes the ensemble-averaged velocity within the porous medium, μ is the fluid viscosity and μ_e is an effective viscosity parameter. Here, μ_e could be considered as a matching parameter which controls the continuity of velocity and shear

stress in the interface of free flow-porous matrix region. In Brinkman's approach, Darcy equation is modified to include a viscous term to facilitate the matching of the boundary conditions at the interface between macropores and micropores. In this study, we recover Brinkman equation through the lattice Boltzmann method.

5.2.1 Spaid approach

Spaid and Phelan used the D2Q7 lattice configuration [148] for modeling micro-scale flow in fibrous porous media. Reducing the momentum in some specified sites is done through the modification of velocity in the particle equilibrium distribution function given by [182]:

$$U = u(x,t) + s(x)\frac{\tau F(x,t)}{\rho(x,t)} \, , \tag{5.2}$$

where U is the modified velocity and $s(x)$ is either 0 or 1, indicating a site as open or porous region, respectively. The form of the forcing term to recover Brinkman equation is as follows:

$$F(x,t) = -\beta\rho(x,t)u(x,t) \, . \tag{5.3}$$

Here, β controls the magnitude of the momentum sink. Replacing F in U we have:

$$U = u(x,t)(1-\beta\tau) \, . \tag{5.4}$$

Setting $\beta = \nu/K_{micro}$, it has been shown that the above equation recovers Brinkman equation [182].

5.2.2 Martys approach

In Spaid's approach [182], the momentum loss due to the microporous region was incorporated by a velocity shift in the Boltzmann equilibrium distribution function. Arguing that this approach could produce errors of order τ^2F^2, Martys proposed an alternative approach in which the momentum loss is incorporated into a body force term. A lattice Boltzmann formulation of evolution equation with body force term is given by [72]:

$$f_\alpha(x + c_\alpha, t+1) = f_\alpha(x,t) + \Omega_{c,\alpha}(x,t) + F_\alpha \, . \tag{5.5}$$

Based on the first and the second order in Hermite polynomials, Martys introduced two models, named as model B1 and B2, respectively. Here we adapt model B2 [115]. Instead of scaling the velocity in the equilibrium distribution function,

in this approach momentum is reduced by scaling the body force term resulting in recovering the Brinkman equation in the micoporous region and Stokes flow in open pores. A forcing term similar to Spaid [182] is used:

$$F = \rho g = -\frac{\mu u}{K} \, . \tag{5.6}$$

Setting $\beta = \nu / K_{micro}$ and $\nu = \mu / \rho$, we have:

$$F = -\beta \rho u \, , \tag{5.7}$$

where ρ and u are macroscopic density and velocity, respectively. β is a parameter controlling the magnitude of the momentum sink and is related to the permeability of the microporous region and fluid kinematic viscosity. In our simulations, micropores correspond to porous matrix regions while macropores are treated as open free flow regions.

Fig. 5.1 shows a slice through a typical representation of a porous model structure used by LBM and MLBM. As can be seen in this figure, LBM needs an explicit representation of solid and fluid node whereas MLBM can handle gray nodes (shown in red in Fig. 5.1b). Although the microporous region was made to be homogeneous here and only one value for β was defined, it is easily possible to use β as a function of location.

5.3 Single phase flow

5.3.1 2D, homogeneous porous media

In contrast to Spaid and Phelan [182], who used pressure boundary conditions, we use gravitational acceleration as body force and periodic boundary conditions in the flow direction. Free fluid layer [114] is implemented for non-periodic structures. D2Q9 lattice configuration was implemented for 2D simulations. First, different 2D models were constructed and simulations performed using Spaid's approach and Martys approach. Although we obtained the same results from both methods for the cases considered, it has been proven that Spaid's approach will produce errors of order $\tau^2 F^2$ in the pressure tensor [115]. To avoid this error, we followed Martys approach for the rest of our simulations.

It is generally accepted that the GLBM and MLBM should reproduce the results of standard lattice Boltzmann method for limiting momentum sink parameters. To check this capability in our model, simulations were performed on 2D model structures in which the momentum sink parameters were varied over the whole range $0 \leq \beta \leq 1$. Figure 5.2 shows the results of simulations compared with

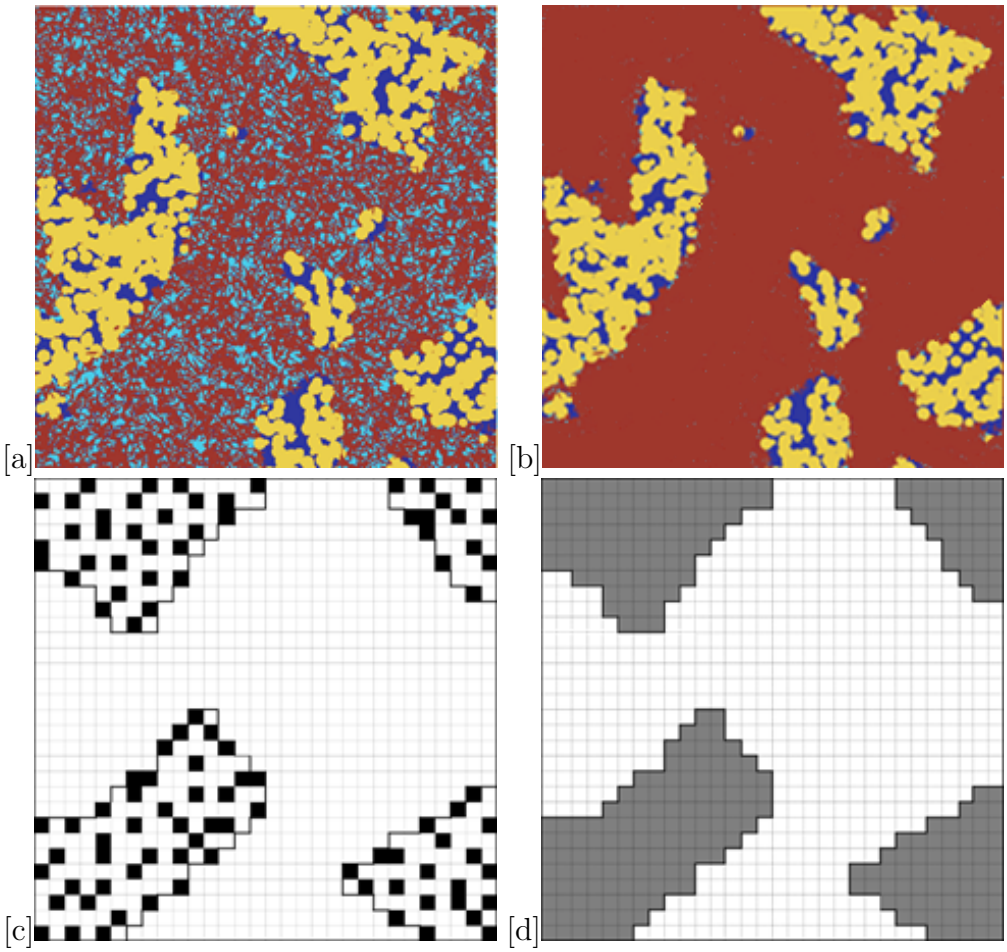

Figure 5.1: A typical 2D representation of a porous structure used by [a] LBM and [b] MLBM. [c] A conceptual model shows an explicit representation of the pores and solid pixels, versus [d] a grey representation of an aggregate of fine pores and solid nodes and larger pores.

the results obtained from an analytical relation (Eqn. 5.8) and percolation theory (see Eqn. 5.9). As evident, for the lower bound of the momentum sink parameter, MLBM reproduces the same results as predicted analytically by [18] for random scatters in a lattice gas model:

$$K = \lim_{n_s \to 0} \frac{\nu}{2n_s} \ , \tag{5.8}$$

where ν is the kinematic viscosity and n_s is a parameter controlling the momentum sink. For the upper bound, MLBM exactly matches the results obtained from percolation theory written as:

$$K = 0.2(\phi - \phi_c)^{1.3} \ . \tag{5.9}$$

Here ϕ and ϕ_c are porosity and critical porosity, respectively.

To show in more detail how the macroscopic lattice Boltzmann method works, a simple 2D channel was considered in which solid pixels were randomly placed

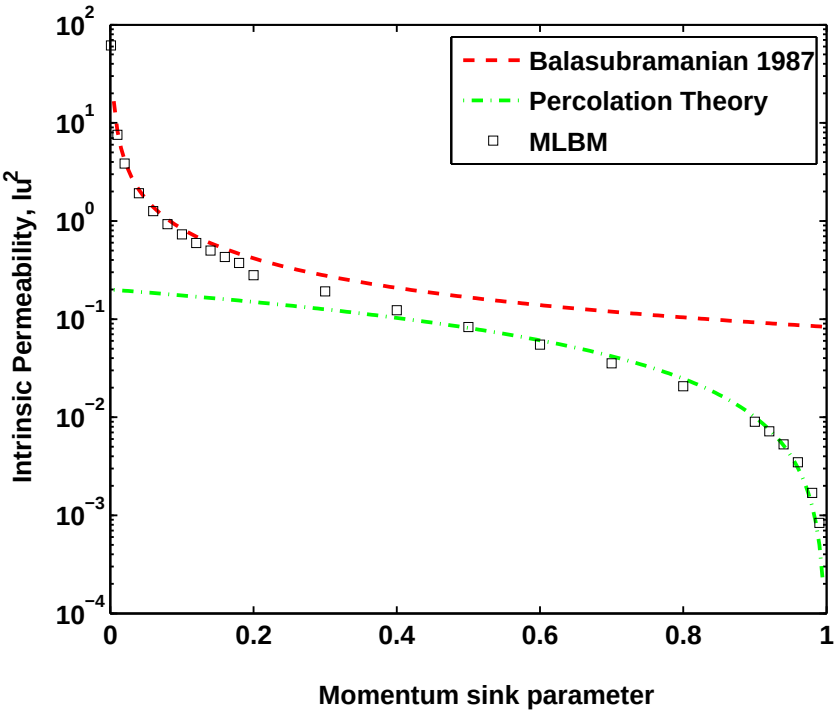

Figure 5.2: Comparing the results of MLBM (this study) with percolation theory and an analytical relation.

between two solid walls (Fig. 5.3). A standard LB method with lattice configuration of D2Q9 [148] was used to solve Stokes equations and to calculate the velocity field. Using the mid-point bounce back scheme, no-slip boundary condition was applied on all solid boundaries and fluid was forced from left to right with a constant body force. Implementing periodic boundary condition at the inlet and outlet boundaries provided an infinite domain for simulations. Local velocity components were averaged and Darcy's law applied to calculate the permeability of the medium. The same procedure was followed for structures exhibiting a wide range of porosity and permeability. In the next step, solid pixels in the channel were removed and all nodes were assigned with the parameter controlling the amount of resistance to flow (Fig. 5.4). The degree of greyness or in other words the degree of momentum sink is related to the permeability of the porous medium and the fluid viscosity.

Following the above procedure, the macroscopic lattice Boltzmann method was implemented for three different momentum sink parameters: 0.1, 0.2 and 0.5. The results are shown in Fig. 5.5. As evident from this figure, the velocity profile has been flattened due to momentum reduction in the channel. The more restriction to flow, the bigger momentum sink and consequently the higher damping occurs in the velocity profile. Similar results reported by [18, 67] for lattice gas models and [48, 189] for lattice Boltzmann method.

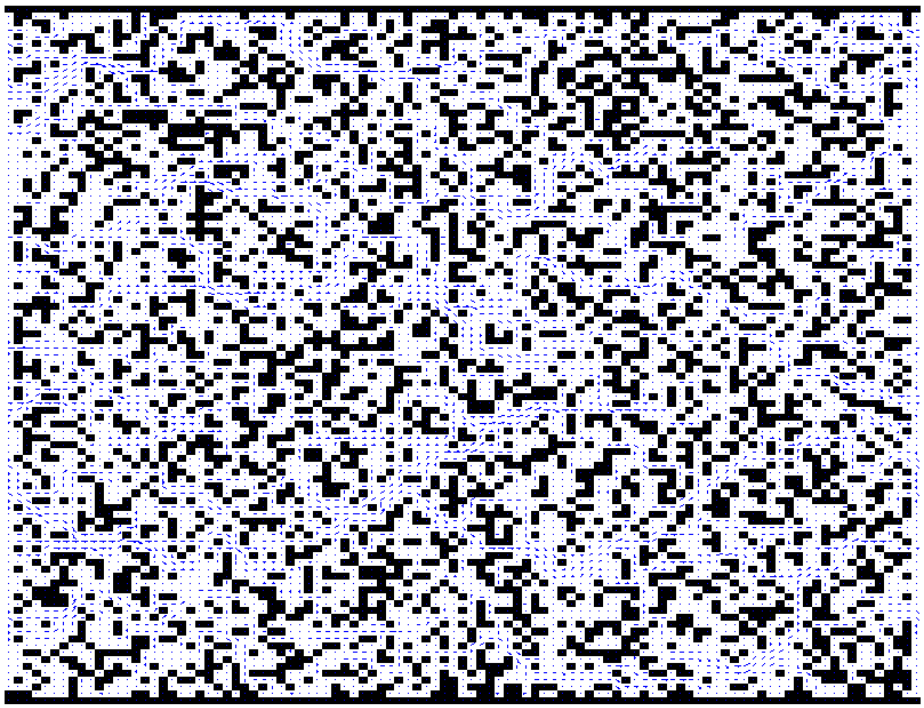

Figure 5.3: A typical representation of a 2D channel, filled with solid pixels. Local velocity components have been superimposed into the structure.

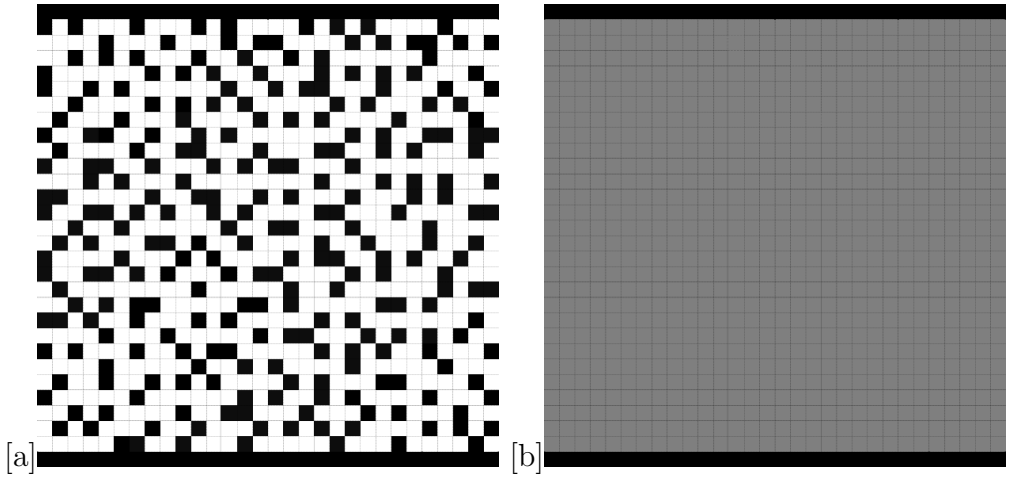

Figure 5.4: Schematic representation of porous media used by [a] LBM and [b] MLBM. LBM requires an explicit representation of pore and solid whereas MLBM could handle grey nodes in addition to black and white representation of solid and pore.

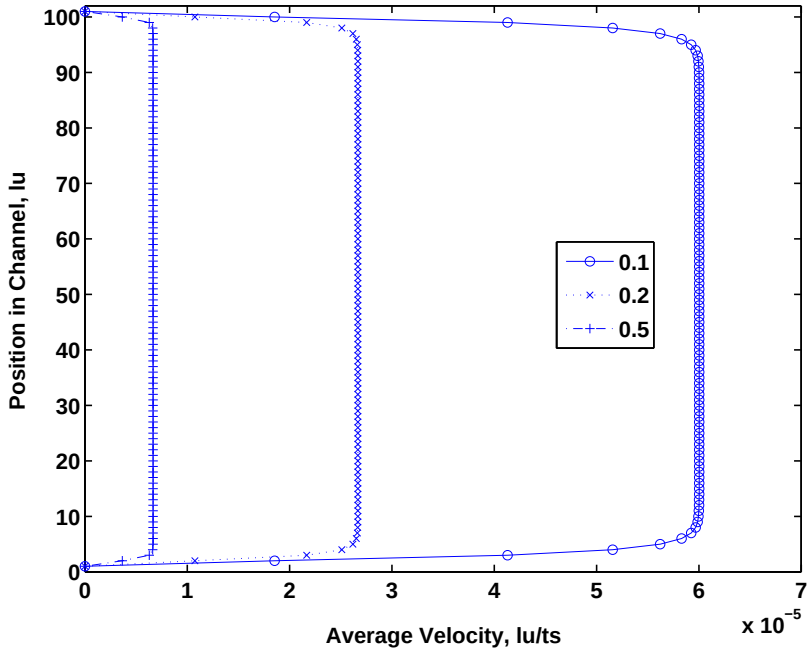

Figure 5.5: Damping velocity in a 2D channel by introducing momentum sink parameter to each pixel.

As mentioned above, macroscopic lattice Boltzmann methods should be able to reproduce the results of the standard lattice Boltzmann method for limiting values of momentum sink parameter. As shown in the Fig. 5.6, our model is doing well in this regard. It gives a parabolic velocity profile for 100 % porous channel and zero velocity for totally impervious channel, corresponding to $\beta = 0.0$ and $\beta = 1.0$, respectively.

5.3.2 2D, heterogeneous porous media

The simulations were also carried out for more heterogeneous porous structures to examine the capability of MLBM to capture the influence of microporosity. Similar to Fig. 3.11, 2D structures were constructed in which a porous matrix is overlaid by an open channel of width 19 *lu* traversing from the inlet to the outlet. For this dual scale porous medium, MLBM needs to treat the open channel and porous matrix differently. A similar procedure as mentioned previously for the 2D channel was applied for the porous region. The solid pixels in the porous region are replaced with momentum sink parameters whereas pixels located in the open channel are treated as 100% porous (Fig. 5.7b). The lattice Boltzmann method employs an explicit representation of pore and solid phases (Fig. 5.7a) and Stokes' equations are recovered in both porous matrix region and in the channel. The

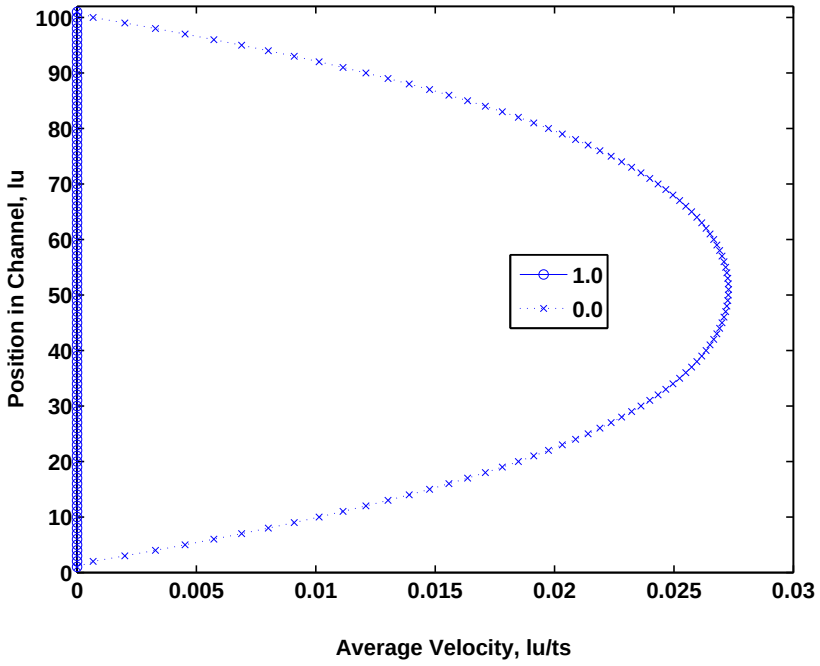

Figure 5.6: Velocity profile in a 2D channel for two extreme values of momentum sink parameters: $\beta = 0$ and $\beta = 1.0$.

macroscopic lattice Boltzmann method recovers Brinkman equation in which the solution of Darcy equation in porous matrix region is coupled with the solution of Stokes' equations in the channel.

Again, the same structures but with porous matrix of different porosity and permeability were constructed. Fig. 5.8 shows the results obtained for three dif-

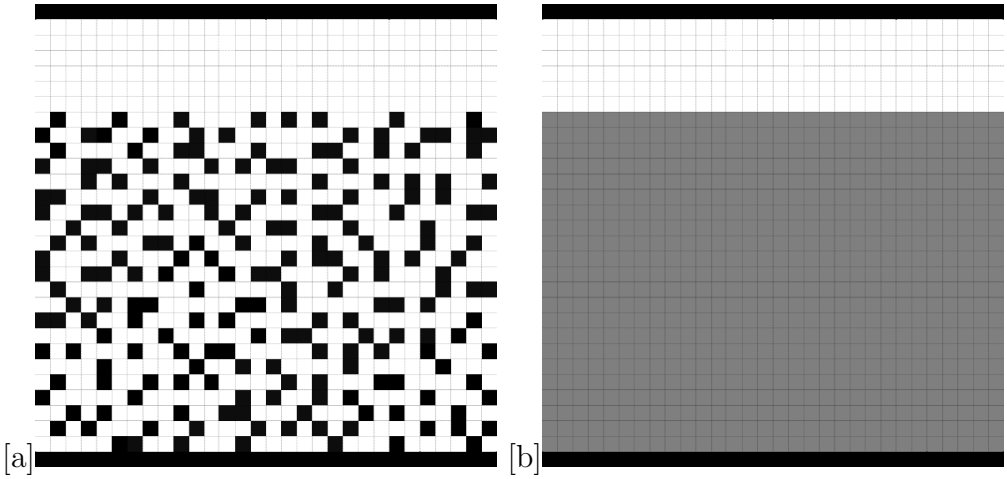

Figure 5.7: Schematic representation of a heterogeneous porous medium used by [a] LBM and [b] MLBM. LBM uses an explicit representation of pore and solid phases while MLBM deals with grey node in addition to black and white nodes representing solid and pore.

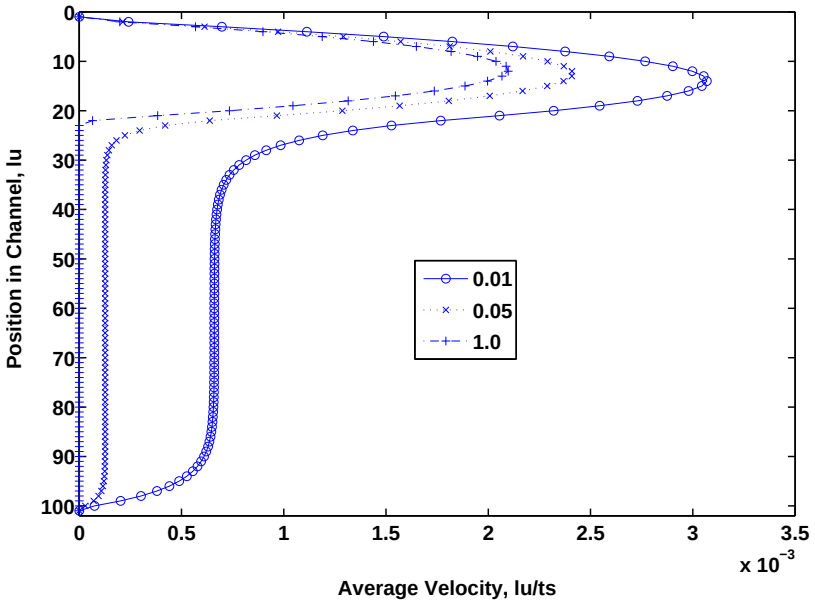

Figure 5.8: Comparing velocity profiles for different momentum sink parameters assigned to porous matrix region shown in Fig. 5.7.

ferent model structures. As can be seen, similar to Fig. 5.5 the velocity profile is damped more as the resistance to flow increases. A momentum sink parameter of $\beta = 1.0$ implies impervious porous matrix. More interestingly is the effect of the porous region on the average fluid flow in these dual-scale porous media. The porosity and the permeability of the porous region have a direct and strong effect on the overall velocity profile even though the flow is parallel to the porous matrix. Another noteworthy point in this figure is the parabolic profile of velocity in the channel versus flat profile in the porous region. Moreover, the condition of continuity of velocity in the interface of porous and free-flow region is also satisfied by the model. This results in the smooth transition in fluid velocity flowing from one region to the other.

In the interest of completeness, another type of heterogeneous model structures was also considered in which a channel was placed between two porous regions (Fig. 3.12). Different realisations with varying channel width and a range of porosity and permeability values for porous matrix were constructed. Fig. 5.9 compares results obtained from MLBM for three different momentum sink parameters. Similar to previous models, porous regions were replaced with homogenised regions where momentum was reduced whereas pixels in the channel considered as free flow nodes where Stokes equations solved.

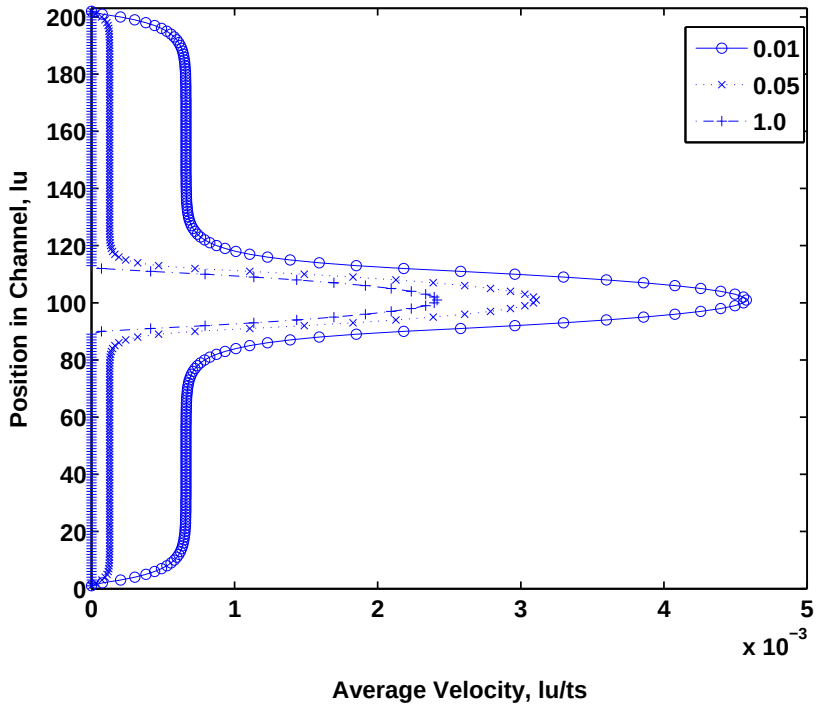

Figure 5.9: Comparing velocity profiles for different momentum sink parameters. The channel width is 21 pixels and crosses through the whole domain.

5.3.3 3D, homogeneous porous media

To show the capability of the MLBM in homogenisation of microporosity region in 3D porous media, the 2D code was extended to 3D and was validated using homogeneous porous media. Following the procedure outlined in chapter 2, homogeneous model structures with unimodal pore size distribution were generated. To allow controlling discretisation errors [10], a set of Boolean models were considered. In addition, X-ray images of Bentheimer and Fontainebleau sandstone as detailed in chapter 2 were used. The characteristics of the model structures and two sand-

Table 5.1: Characteristics of unimodal porous media.

Porous medium	Particle diameter (lu)	Sample size
Model A	20	$400 \times 400 \times 400$
Model B	40	$400 \times 400 \times 400$
Model C	80	$800 \times 800 \times 800$
Bentheimer	-	$400 \times 400 \times 400$
Fontainebleau	-	$400 \times 400 \times 400$

stone samples used in this study, have been summarised in Tab. 5.1. The size of the samples were selected with considering the representative elementary volume

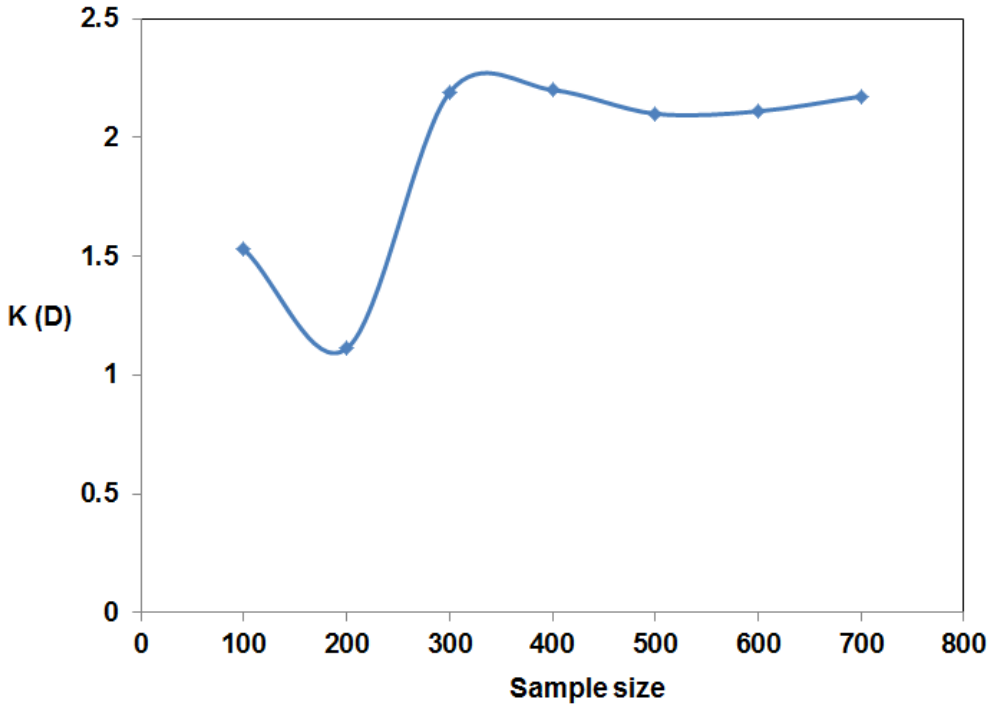

Figure 5.10: REV test on FB sandstone.

(REV) concept [23, 77]. It is generally accepted that for having a representative sample, there should be at least 7-10 particles or grains across the sample [17]. It is clear that for Boolean models A-C, this condition is satisfied. An REV test was carried out for Fontainebleau sandstone (Fig. 5.10), showing that the sample size of 400^3 voxel is sufficient for being an REV.

Table 5.2: Results computed from standard LBM and macroscopic LBM.

Porous medium	ϕ	$K_{z,LBM}$ [lu^2]	β	$K_{z,MLBM}$ [lu^2]
Model A	0.26	0.184	0.905	0.184
	0.5	2.301	0.072	2.302
	0.8	29.362	0.005	29.239
Model B	0.17	0.167	0.996	0.167
	0.5	10.142	0.016	10.162
	0.8	113.116	0.002	111.099
Model C	0.12	0.172	0.969	0.172
	0.5	40.891	0.004	40.695
	0.8	407.479	0.0004	414.154
Bentheimer	0.21	0.288	0.578	0.288
Fontainebleau	0.17	0.179	0.927	0.180

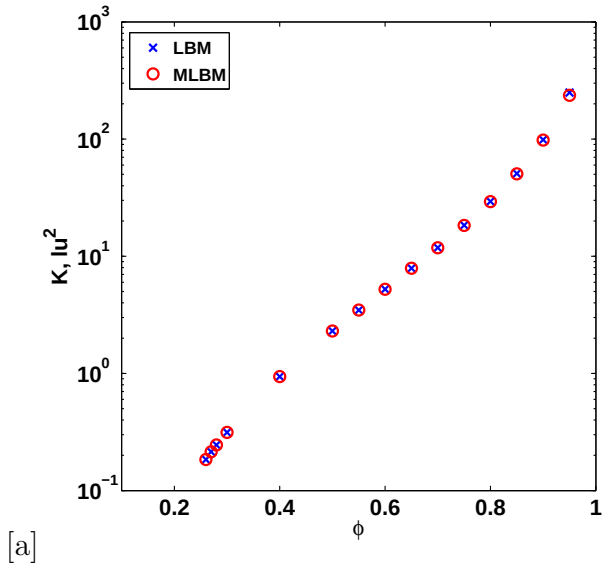

[a]

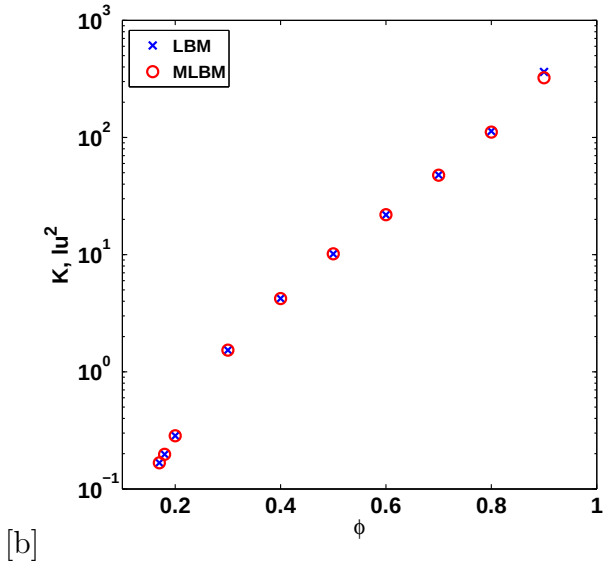

[b]

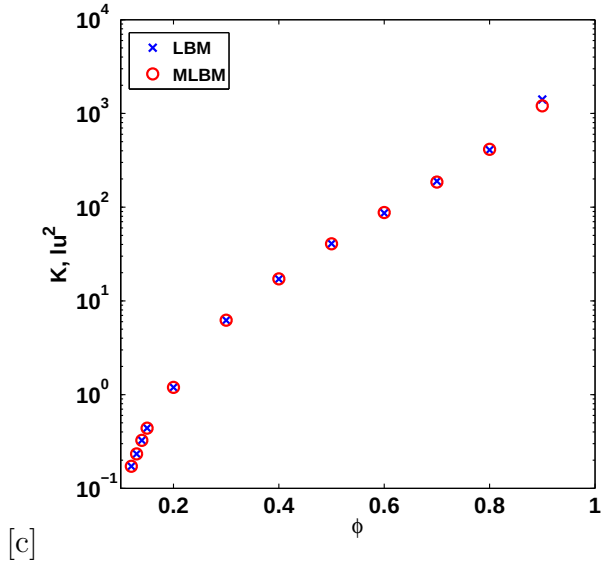

[c]

Figure 5.11: The comparison between permeabilities calculated by LBM and MLBM for three different model structures. [a] Model A, [b] Model B and [c] Model C.

The results of computations for the simulated model structures and sandstone samples with a fairly wide range of porosities for the model structures are given in Tab. 5.2. A standard lattice Boltzmann method was first implemented to obtain velocity field and consequently to calculate the permeability. This permeability is considered as "true solution" and is also used to calculate the momentum sink parameter, β, for the macroscopic lattice Boltzmann method. Periodic boundary conditions were applied in all three directions and no-slip condition implemented on the boundary of solid nodes through a mid-way bounceback scheme.

It should be noted that, similar to the procedure for 2D structures, standard LB simulations were performed on explicit representations of pore and solid whereas in MLBM simulations all pore and solid voxels were replaced with a uniform grey scale which corresponds to momentum sink parameter. For model A with porosity of 0.26, for instance, we have $\beta = \nu/K = ((2\tau-1)/6)/K_{z,LBM} = (1/6)/0.184 = 0.905$.

In addition, Fig. 5.11 compares LBM and MLBM for three model structures A, B and C for the whole range of porosity. As can be seen, there is an excellent agreement between LBM and MLBM. While the validity of the Brinkman equation for dilute systems has been proven [91, 54], its applicability for low porosity systems is still an open question. Knowing that the MLBM recovers the Brinkman equation, the results shown in Fig. 5.11 might prove the validity of the Brinkman equation for very dense systems.

The results shown in Tab. 5.2 and Fig. 5.11 highlight the capability of the MLBM for calculating permeability on images with finite resolution and in particular for bimodal porous media.

5.3.4 3D, heterogeneous porous media

As shown in Fig. 5.1 and explained above for unimodal porous media, for upscaling heterogeneous porous media using MLBM, microporous region is assumed as homogeneous where momentum is scaled based on permeability of that region and fluid viscosity. Macropores, however, are treated as free-flow region and Stokes equations are solved. Four models D, E, F and G, which were the subject of microporosity investigation in chapter 3, are considered for this purpose. For all these models, the Boolean model 1 in Table 3.1 constitutes the microporosity phase and therefore its permeability (K_z = 0.871 D) is used for calculating the momentum sink parameter in MLBM simulations. All simulations were performed on 10 realizations of these models and the average and standard deviation of the calculated permeabilities is reported in Tab. 5.3.

Table 5.3: Results computed from LBM and MLBM for single phase fluid flow on 3D heterogeneous model structures D – G.

Models	Size	$K_{z0,micro}$ [D]	$K_{z0,macro}$ [D]	$K_{z,micro}$ [D]	$K_{z,macro}$ [D]	$K_{z,LBM}$ [D]	σ_{LBM}	$K_{z,MLBM}$[D]	σ_{MLBM}
D	400^3	0.033	5.011	0.269	5.45	5.719	0.117	6.19	0.113
E	400^3	0.309	1.16	0.651	1.901	2.552	0.074	3.16	0.083
F	400^3	0.534	0.183	0.777	0.752	1.529	0.027	1.73	0.033
G	400^3	0.686	0.031	0.829	0.331	1.16	0.021	1.06	0.029

The comparison between LBM and MLBM for heterogeneous models D, E, F and G corresponding to porosity 0.58, 0.54, 0.52 and 0.51 is also shown in Fig. 5.12. Similar to Fig. 5.11 for unimodal model structures, MLBM reproduces LBM results in bimodal porous media. The permeability of macropore is also shown in this figure. Once more, the difference between macropore permeability and LBM (micro + macro) highlights the effect of microporosity.

5.3.4.1 Effect of disconnected macro-porosity on permeability

To address the important case of a vuggy carbonate system, cases were also considered in which the macropores do not form a percolating cluster and their connectivity is solely through micropores. This case is of particular relevance, since often in the case of heterogeneous carbonate plugs the micro-porosity might not be resolved and one only has a permeability estimate of the (homogenised) background through other means. Using Boolean model 3 and Boolean model 4 (Tab. 5.4), random 4-phase model structures of size 400^3 (model H) and 800^3 (model I) with the same GRF realisation were generated, thus keeping the spatial distribution of micro- and macro-porosity constant. For model I this implies that both micro- and macro-phase are closer to their respective REVs. The permeability of the Boolean model 4, which constitutes the macro-porous region, is 3.54 (D) and nearly one order of magnitude greater than the permeability of Boolean model 3 as constitutive model for the micro-porous region (Tab. 5.4).

Since both models H and I were designed with macropores below the percolation threshold we have $\mathrm{K}_{z0,macro} = 0$ when microporosity is assumed to be impervious. On the other hand, when both micro- and macro- phase are contributing to the flow, the effective permeability of the system will increase to 0.315 (D) and 0.307 (D) for model H and model I, respectively. Not surprisingly, in both model H and I, the contribution of the disconnected vugs increased the effective permeability by a factor of almost 3. This is consistent with the results reported by [124] for partially dissolved microporosity where micropores provide parallel flow paths to the disconnected macropores. An increase of permeaility in the range of 1-7% was obtained for the single length scale ratios of 3, 4 and 5 with maximum of 14% for a mix of scaling parameters in the range of {3, 4, 5} [124]. The influence of microporosity on the effective permeability are more significant in our simulations compared to those presented by [124]. This is mainly due to the smaller length scale ratio of 2 that we used.

We compare direct calculations on the model ($\mathrm{K}_{z,LBM}$) to the homogenised solution ($\mathrm{K}_{z,MLBM}$) in Tab. 5.5. The permeability of Boolean model 3 ($\mathrm{K}_z = 0.202$ D), constituting the microporosity, was used for calculating the momentum sink

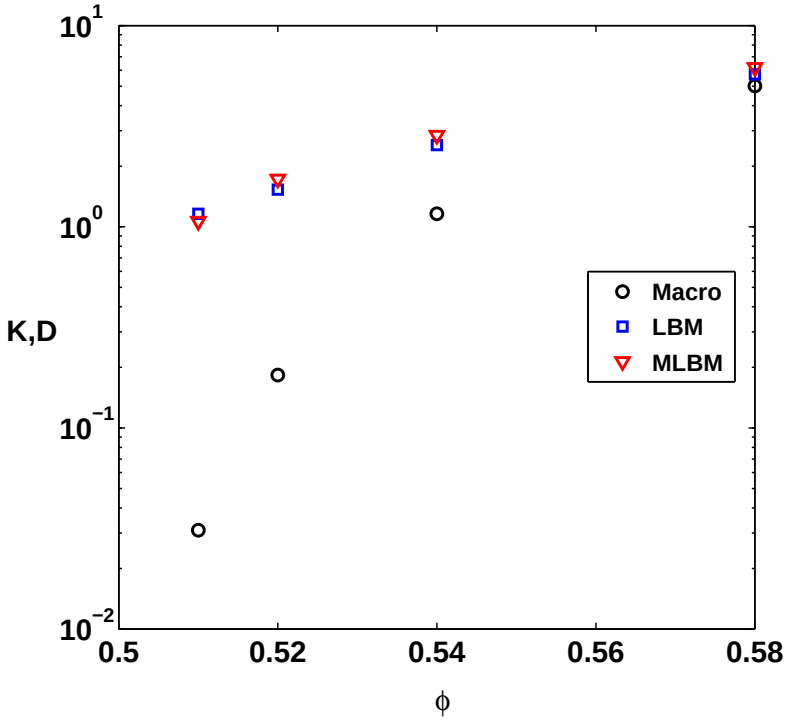

Figure 5.12: The comparison between peremabilities calculated by LBM and MLBM for models D, E, F and G with total porosity 0.58, 0.54, 0.52 and 0.51, respectively.

parameter. The microporous region was homogenised and its effect on the whole permeability was coupled into macropores through MLBM. The relative mismatch between LBM and MLBM for models H and I is up to 40%. Considering that permeability for such systems might vary by order of magnitudes, this implies that the most important uncertainty is in the estimation of the background permeability.

Table 5.4: Characteristics of Boolean models used for generating model H and I.

Particle model	Particle diameter (lu)	Particle fraction	Critical length (lu)	K_z (D)
Boolean Model 3	12	0.65	14	0.202
Boolean Model 4	24	0.50	36	3.54

Table 5.5: Results computed from LBM and MLBM for single phase fluid flow on model H and I representing vuggy carbonate models.

Models	Size	$K_{z0,micro}$ [D]	$K_{z0,macro}$ [D]	$K_{z,micro}$ [D]	$K_{z,macro}$ [D]	$K_{z,LBM}$ [D]	σ_{LBM}	$K_{z,MLBM}$[D]	σ_{MLBM}
H	400^3	0.153	0.0	0.197	0.118	0.315	0.008	0.397	0.0179
I	800^3	0.158	0.0	0.192	0.116	0.308	0.00308	0.433	0.0067

5.4 Two phase flow

It is interesting to note that when investigating the effect of microporosity on drainage relative permeability of the wetting phase for heterogeneous rocks, a percolation threshold of the wetting phase in the macropore region is always reached at some point. In chapter 4, the significance of microporosity on the effective permeability of the wetting phase was shown. Now, the question to answer is how to couple the microporosity effect into the macropores for partially saturated models? In contrast to single phase flow where the sample is completely saturated by a single fluid and the effective permeability is only a function of morphology and topology of the pore space, in two phase flow the saturation and distribution of fluids is also affecting the macroscopic flow properties.

5.4.1 3D, heterogeneous porous media

5.4.1.1 Upscaling through MLBM

Following the procedure described in section 4.3 for partially saturated models, the saturation and distribution of the wetting phase in micro- and macropore was determined. Wetting phase and solid phase in micropore and macropore were assigned different labels. Only one label was set for non-wetting phase in both micro- and macropore. While LBM was used for solving the Stokes equations on the wetting phase and to calculate its effective permeability, MLBM was implemented for upscaling. For LBM, we used an explicit representation of all phases (wetting phase, non-wetting phase and solid) in both micro- and macropore regions whereas in MLBM, the resolved wetting phase in macropores was coupled with an average effect of wetting phase in micropores. Similar to single phase flow, the permeability calculated from LBM was considered as a "true solution" to be compared with the results of MLBM.

Different scenarios were tested for coupling the effective permeability of the wetting phase in macropores with an average effect of the wetting phase in micropores. Since macropores represent pores whose sizes are larger than the image resolution, the wetting phase in macropore is resolved and therefore no momentum reduction is applied for this phase in all scenarios. For micropores, however, the wetting phase and solid is replaced with a homogenised medium with corresponding momentum sink parameter which is related to the fluid viscosity and the effective permeability of the wetting phase at each saturation. The main difference between these scenarios is the way that the momentum sink parameter is defined for the wetting phase in micropores.

In the first scenario, namely Scen1, the momentum sink parameter, β, is defined as:

$$\beta = \frac{\nu}{k_{w,micro}} \ , \tag{5.10}$$

where $k_{w,micro}$ is the effective permeability of wetting phase in micropore and is calculated based on the flux analysis technique described in section (3.5.2) and applied on high resolution image. ν, is the kinematic viscosity which is related to the relaxation time by Eqn.3.7. In this scenario, the local flux computed from LBM for the wetting phase in micro and macropores is post processed to determine the amount of flux passing through the micro- and macropore individually.

In the second scenario, Scen 2, the same equation for β was adapted but $k_{w,micro}$ was computed differently. For this scenario, LBM was run for wetting phase in micropore only. While different boundary condition in this method results in different $k_{w,micro}$ compared to Scen 1, a huge difference is not expected. Since the microporosity remains embedded in the larg scale GRF structure, both methods therefore define a macro-scale relative permeability curve through $\beta(S_{w,micro})$, including the macro-tortuosity of the microporosity.

Fig. 5.13 compares the results of LBM as a "true solution" with an upscaled solution obtained by MLBM based on Scen 1 and Scen 2. Although for all models, there is a little difference between Scen 1 and Scen 2 and both of them agree well with the results of LBM, Scen 2 is slightly more accurate than the Scen 1. In addition, in all models MLBM is only applicable for $S_w > 0.5$ and the reason for this is that for all saturations less than 0.5, the effective permeability of the wetting phase in micropore is so small resulting in a momentum sink parameter larger than 1. Defining the momentum sink parameter via Eqn.5.10 and being constrained by the condition $0 \leq \beta \leq 1.0$ and $\tau = 1.0$ results in $k_{w,micro} = 0.166\ lu^2$ as the lower limit for the effective permeability of wetting phase in micropores.

Another point which is worth mentioning in Fig. 5.13 is that by having the right momentum sink parameter, MLBM reproduces the results of LBM, although for $S_w > 0.5$. In both Scen 1 and Scen 2, an explicit representation of wetting phase in micropores was used for computing $k_{w,micro}$ and consequently the momentum sink parameter. However, at any particular resolution, only the macropores are resolved and micropores are kept unresolved. Therefore, similar to single phase flow an explicit representation of wetting phase in macropores needs to be coupled with its average effect in micropores. The results shown in Fig. 5.13 is computed on five different realisations of each GRF model. Tab. 5.6 shows detailed results for both Scen 1 and Scen 2.

Named as Scen 3, in the third scenario the relative permeability-saturation relationship of the wetting phase in pure micropore model is used for coupling

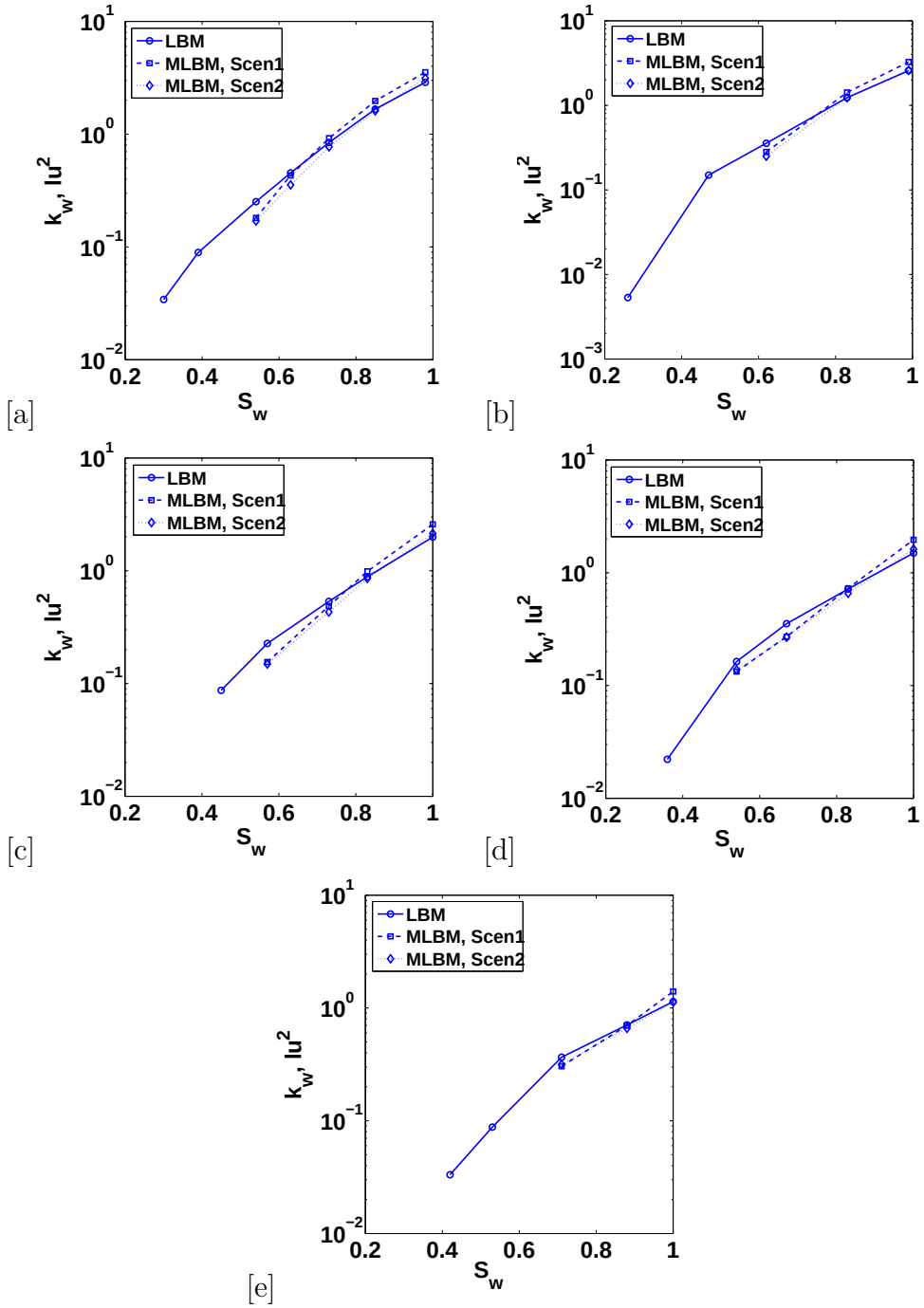

Figure 5.13: The comparison between LBM as "true solution" and MLBM, as an upscaled solution, based on two scenarios for [a] GRF50, [b] GRF60, [c] GRF70, [d] GRF80 and [e] GRF90.

Table 5.6: Detailed results of LBM and MLBM simulations under two scenarios: Scen1 and Scen2 (all permeabilities are reported in lu^2).

			Scen1		Scen2	
	S_w	$k_{w,LBM}$	$k_{w,micro}$	$k_{w,MLBM}$	$k_{w,micro}$	$k_{w,MLBM}$
GRF50	0.12	0.0000	0.0000	0.0000	0.0000	0.0000
	0.30	0.0342	0.0342	0.0000	0.0314	0.0000
	0.39	0.0893	0.0866	0.0000	0.0807	0.0000
	0.54	0.2518	0.2056	0.1810	0.1593	0.1695
	0.63	0.4532	0.2830	0.4304	0.1870	0.3548
	0.73	0.8442	0.3606	0.9198	0.1973	0.7718
	0.85	1.6684	0.4602	1.9740	0.2048	1.6123
	0.98	2.8820	0.5620	3.5440	0.2088	3.1260
GRF60	0.14	0.0000	0.0000	0.0000	0.0000	0.0000
	0.26	0.0053	0.0053	0.0000	0.0000	0.0000
	0.47	0.1497	0.1444	0.0000	0.1395	0.0000
	0.62	0.3563	0.3030	0.2814	0.2780	0.2500
	0.83	1.2329	0.4960	1.4234	0.3560	1.2300
	0.99	2.5702	0.6442	3.2560	0.4568	2.6000
GRF70	0.16	0.0000	0.0000	0.0000	0.0000	0.0000
	0.45	0.0870	0.0865	0.0000	0.0000	0.0000
	0.57	0.2267	0.2142	0.1552	0.1958	0.1492
	0.73	0.5351	0.4273	0.4864	0.3384	0.4298
	0.83	0.8852	0.5434	0.9894	0.3748	0.8564
	1.00	1.9872	0.7272	2.5760	0.3990	2.1380
GRF80	0.19	0.0000	0.0000	0.0000	0.0000	0.0000
	0.36	0.0221	0.0221	0.0000	0.0000	0.0000
	0.54	0.1632	0.1608	0.1330	0.1985	0.1380
	0.67	0.3531	0.3396	0.2706	0.3344	0.2678
	0.83	0.7177	0.5818	0.7276	0.4902	0.6576
	1.00	1.4952	0.7852	1.9620	0.5322	1.6200
GRF90	0.21	0.0000	0.0000	0.0000	0.0000	0.0000
	0.42	0.0332	0.0332	0.0000	0.0000	0.0000
	0.53	0.1089	0.1080	0.0000	0.0000	0.0000
	0.71	0.3658	0.3544	0.3044	0.3560	0.3158
	0.88	0.7068	0.6386	0.6988	0.6014	0.6602
	1.00	1.1396	0.8332	1.4000	0.6828	1.1266

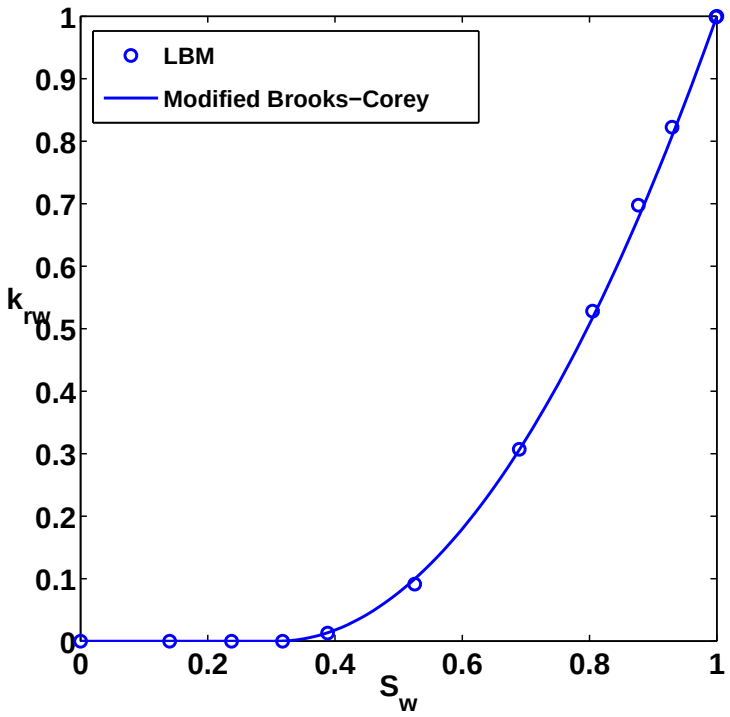

Figure 5.14: The relationship between relative permeability and saturation of the wetting phase of pure micropore model (GRF100). Lattice Boltzmann method was implemented for calculating relative permeability at some limited saturation points on which the modified Brooks-Corey function was fitted.

micropore into the macropore. Model GRF100, as a pure micropore model, was partially saturated and the relative permeability calculated for the wetting phase. Fig 5.14 depicts the $k_{rw} - S_w$ relationship computed at some saturation points with the modified Brooks-Corey function fitted and shown as solid line. In our notation, the modified Brooks-Corey relationship for the wetting phase relative permeability is [139]:

$$k_{rw} = k_{rw,max} \left(\frac{S_w - S_{wc}}{1 - S_{nwr} - S_{wc}} \right)^{n_w} , \tag{5.11}$$

where k_{rw} and S_w are the relative permeability and saturation of the wetting phase, respectively. S_{wc} is the connate wetting phase saturation, S_{nwr} is the residual non-wetting phase saturation and n_w is a fitting exponent ranging from 1 to 6. With $k_{rw,max} = 1.0$, $S_{wc} = 0.31$ and $S_{nwr} = 0.0$, the best fit is obtained for $n_w = 1.98$ with root-mean-square-error (RMSE) [199] of 0.01985.

Following the procedure explained in Fig. 4.8, wetting phase saturation is first decoupled into micro and macropore. Then, at each saturation, the corresponding relative permeability to $S_{w,micro}$ is obtained from Fig. 5.14. Multiplying the relative permeability with the absolute permeability of the pure micropore model (K =

$0.873\ lu^2$) results in the effective permeability of the wetting phase in the micropore regions at each saturation, which is later used for calculating the momentum sink parameter. Consequently, for upscaling, wetting phase and solid particles in micropore regions are homogenised and coupled with the wetting phase in macropores. Similar to Scen 1 and Scen 2, no momentum reduction applies for wetting phase in macropores while in micropores a momentum sink parameter corresponding to the microporosity saturation is applied.

The results of Scen 3 are shown in Fig. 5.15 and compared with the results of LBM (see Tab. 5.7 for more details). Adapting the same equation as Eqn.5.10, we could only apply MLBM for models GRF70, GRF80 and GRF90. Since for models GRF50 and GRF60 the wetting phase saturation in micropore regions and corresponding wetting phase permeability is so small, β value is out of the range. The same issue arises at low saturations of wetting phase in micropores for GRF70, GRF80 and GRF90. For higher saturations, there is a good agreement between LBM and MLBM especially for GRF70 and GRF90. Fig. 5.15 also shows the effective permeability calculated on the wetting phase in macropore only. Similar to Fig. 4.10 and Fig. 4.11, this again highlights the effect of microporosity on the relative permeability.

As shown above, adapting Eqn.5.10 for defining the momentum sink results in $\beta < 0$ at low wetting phase saturations. To address this issue, scenario 4 was devised. In this scenario, named as Scen 4, another relation for β was implemented which was proposed by [196] and is claimed to be applicable for the whole range of solid density fractions. The relation is as follows:

$$\beta = \frac{\nu}{2k_{w,micro} + \nu}\ , \tag{5.12}$$

where $k_{w,micro}$ is the effective permeability of wetting phase in micropore and ν is the kinematic viscosity. Similar to Eqn. 5.10, both $k_{w,micro}$ and ν are in lattice units.

Fig. 5.16 a and Fig. 5.16 b show the results of Scen 4, for GRF50 and GRF60. As can be seen, by using Eqn.5.12 for computing β, MLBM remains always valid for coupling the wetting phase in micro- and macropores. In both models, for total wetting phase saturation less than 0.5, $S_{w,micro}$ is so small resulting in $k_{w,micro} = 0$ but for $S_w > 0.5$ there is an excellent agreement between LBM and MLBM.

Eqn. 5.12 was also tested for GRF70, GRF80 and GRF90 and the results are shown in Fig 5.16. For GRF70 (Fig. 5.16 c), Eqn. 5.12 results in better definition of momentum sink parameter compared to Eqn. 5.10 and the agreement between LBM and MLBM is very good. It also reproduces the results of LBM at lower saturations ($S_w = 0.57$ and $S_w = 0.45$). Similarly, in GRF80 scenario 4 could be

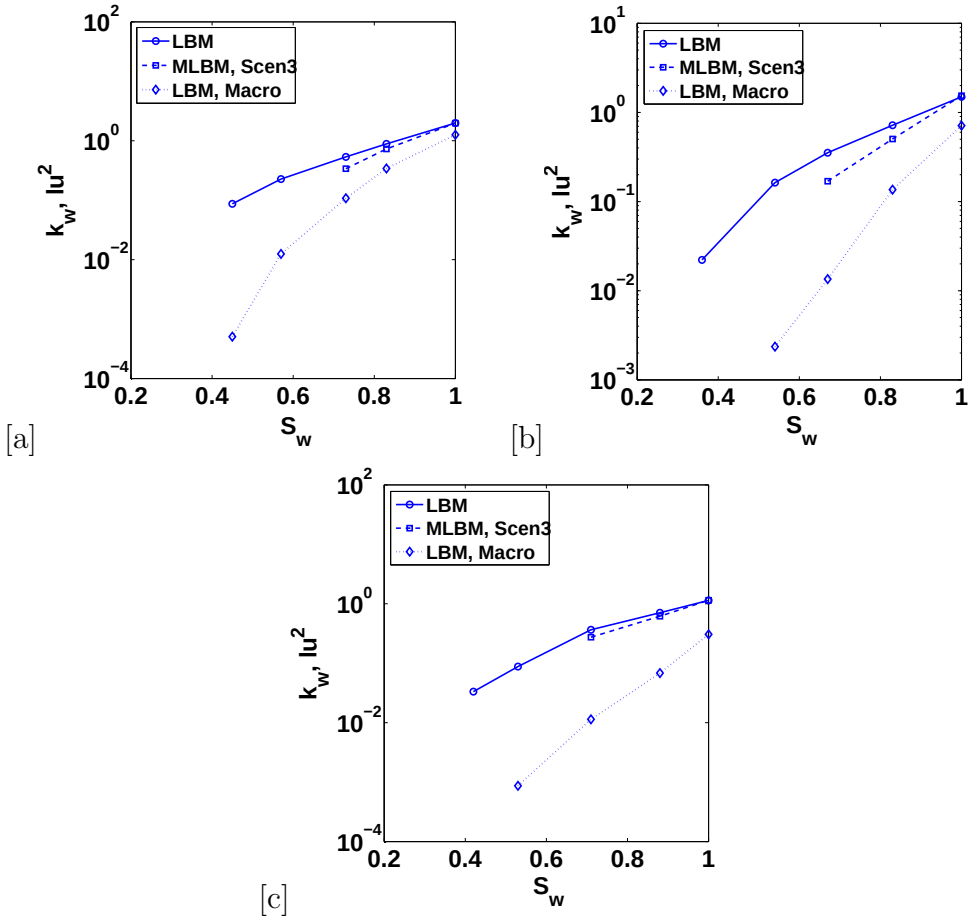

Figure 5.15: The comparison between LBM as "true solution" and MLBM, as an upscaled solution, based on scenario 3 for [a] GRF70, [b] GRF80, [c] GRF90. The effective permeability of wetting phase in solely macropore is also shown and highlights the effect of micropores on k_w.

used for implementing MLBM for lower wetting phase saturations, $S_w = 0.36$, (Fig. 5.16d) compared to $S_w = 0.67$ in Scen 3 (Fig. 5.15b). While the agreement between LBM and MLBM for saturations down to $S_w = 0.54$ is good and significantly improves on using macroporosity only, it overestimates LBM results at $S_w = 0.36$. Again, in GRF90 Scen 4 can be used for implementing MLBM for saturation down to $S_w = 0.36$ (Fig. 5.16e), but it slightly overestimates LBM for the whole range of saturations.

5.4.1.2 Upscaling through Laplace equation

Upscaling by solution of a Laplace equation is traced back to 1990s by which the effective permeability of each phase is upscaled, resulting in pseudo-relative permeabilities for coarse grid simulations [3, 178, 160]. At the pore scale, [172] derived a generalised Laplace equation from a diffusive-advective method for creeping flow

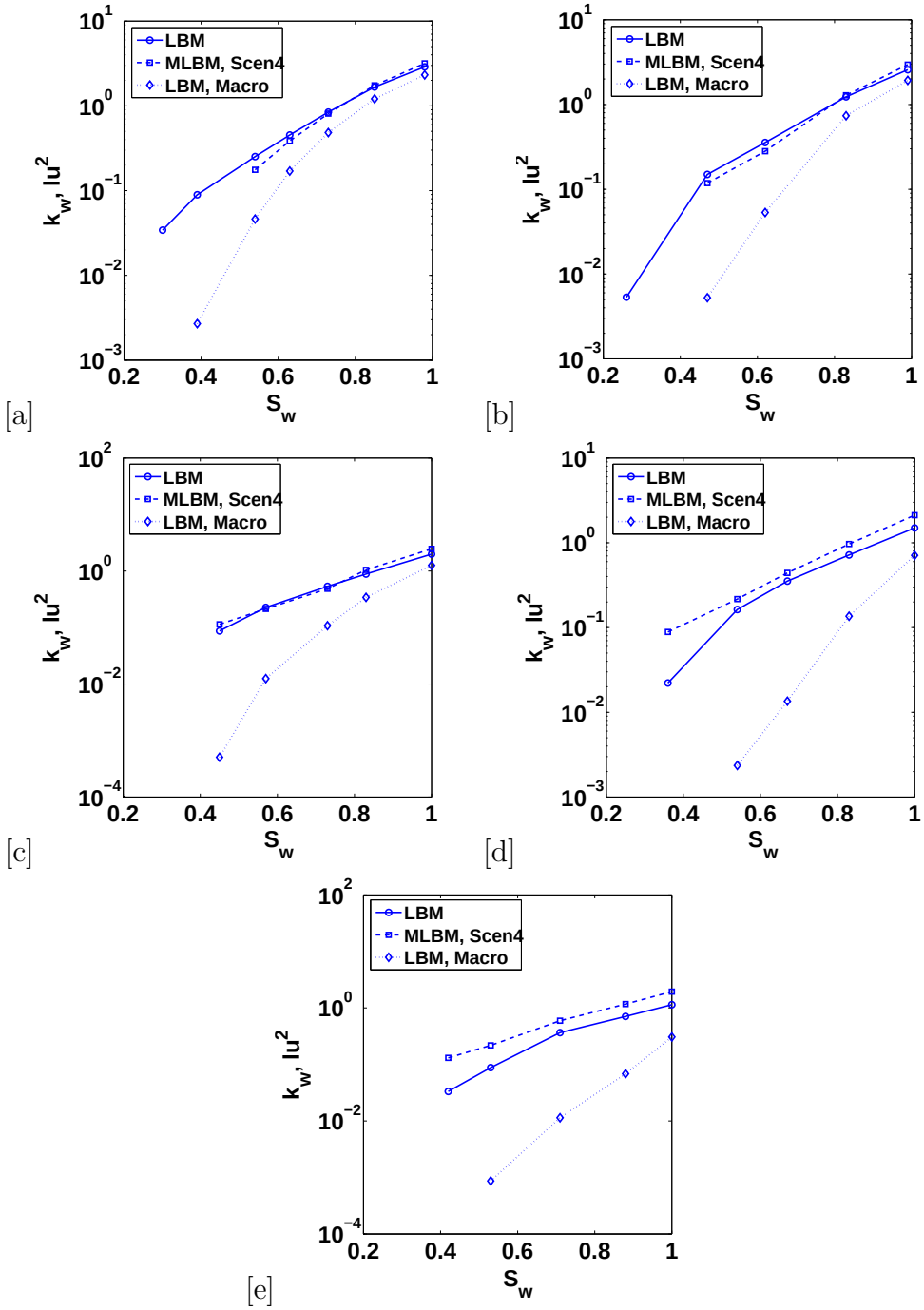

Figure 5.16: The comparison between LBM as "true solution" and MLBM, as an upscaled solution, based on scenario 4 for [a] GRF50, [b] GRF60, [c] GRF70, [d] GRF80 and [e] GRF90. The effective permeability of wetting phase in macropore only is also shown and highlights the effect of micropores on k_w.

Table 5.7: Detailed results of LBM and MLBM simulations based on scenario 3. $S_{w,micro}$ is the wetting phase saturation in microporous region of the heterogeneous models while $k_{w,micro}$ is corresponding permeability obtained from Fig. 5.14 (all permeabilities are reported in lu^2).

	S_w	$k_{w,LBM}$	$S_{w,micro}$	$k_{w,micro}$	$k_{w,MLBM}$
GRF70	0.16	0.0000	0.15	0.0000	0.0000
	0.45	0.0870	0.41	0.0192	0.0000
	0.57	0.2267	0.52	0.0786	0.0000
	0.73	0.5351	0.61	0.1746	0.3392
	0.83	0.8852	0.64	0.2183	0.7268
	1.00	1.9872	0.65	0.2226	1.9760
GRF80	0.19	0.0000	0.18	0.0000	0.0000
	0.36	0.0221	0.34	0.0017	0.0000
	0.54	0.1632	0.51	0.0786	0.0000
	0.67	0.3531	0.63	0.1999	0.1690
	0.83	0.7177	0.72	0.3239	0.5028
	1.00	1.4952	0.76	0.3885	1.5380
GRF90	0.21	0.0000	0.20	0.0000	0.0000
	0.42	0.0332	0.42	0.0262	0.0000
	0.53	0.1089	0.52	0.0786	0.0000
	0.71	0.3658	0.71	0.3056	0.2738
	0.88	0.7068	0.83	0.5151	0.6166
	1.00	1.1396	0.88	0.6024	1.1460

in a porous medium. The equation reads as:

$$\nabla \cdot d\nabla P = 0 \ , \tag{5.13}$$

where d is a weight factor assigned to each voxel and is related to its position in the pore space. The pressure field and consequently the velocity field, obtained via solution of the Laplace equation, was used in Darcy's equation for calculating single phase effective permeability of the sample. Most recently, Laplace method was successfully tested for upscaling absolute permeability and formation factor from the pore scale to the core scale [90]. Here, we investigate its application for upscaling the effective permeability of the wetting phase from the pore scale in highly heterogeneous porous media and particularly at low wetting phase saturations.

Darcy's law for the flow of a single phase fluid in porous medium gives:

$$Q = -(K/\mu)\nabla P \ , \tag{5.14}$$

where Q is the volumetric flow rate per unit area, K is the permeability, μ is the viscosity and P is the pressure. Assuming incompressible flow, i.e. $\nabla \cdot Q = 0$, with constant viscosity and permeability results in the following equation for the pressure, which is known as the Laplace equation:

$$\nabla \cdot (K \nabla P) = 0 \, . \tag{5.15}$$

Here K is the local permeability at each voxel and we use an approximation method for obtaining it. The estimation of voxel-wise permeability based on the Euclidean distance map has been introduced by [8] and its validity was tested against a LB method. It reads as:

$$k_{i,j,k} = (r_{EDT(i,j,k)} - C)^2 \, , \tag{5.16}$$

where C is half the voxel size, r_{EDT} is the Euclidean distance of the phase of interest, introduced in section (4.1.3), and subscripts (i, j, k) refer to the specific coordinate of each voxel. It should be noted that unlike [172], this estimator does not use a parabolic profile for velocity but it works accurately at typical tomogram resolution because the discretisation errors are compensated in calculating the distance map.

To obtain the upscaled value of K, the next step is to solve the Laplace equation using appropriate boundary conditions. For a 3D structure (with dimensions $L_x \times L_y \times L_z$ and $0 \leq x \leq L_x$, $0 \leq y \leq L_y$, $0 \leq z \leq L_z$), by applying pressure boundary conditions on planes perpendicular to the flow direction and imposing either 'no-flow', 'periodic' or 'linear in pressure' condition on lateral boundaries, one can solve the above equation for the pressure field by using a finite difference or finite element method [21]. We use pressure boundary conditions in the flow direction and 'periodic' conditions on the lateral boundaries. By having the pressure field computed from the Laplace equation and estimating the local permeability field from Euclidean distance map of a particular phase in the image, Darcy's law gives local volumetric flow rate through each elementary volume of that phase, which is a voxel in this context. Total volumetric flow rate, Q, is then obtained by summation over all local volumetric flow rates. Having Q, differential pressure along the porous medium (∇P) and the viscosity of the fluid, μ, the upscaled or average permeability could be calculated from Darcy's law.

Before applying Laplace solver for coupling the effective permeability of the wetting phase in micropores with that in macropores, we test its capability for estimating wetting phase permeability at some saturation points on a high resolution image. The computations were performed on one realisation of model GRF50. At each saturation, the EDT map of the wetting phase was obtained and used for estimating local permeability field through Eqn. 5.16. A 2D slice of EDT map of the wetting phase at saturation $S_w = 0.39$ and its corresponding local permeability

field is shown in Fig. 5.17. A finite element formulation [10, 16] was used to solve the Laplace equation and resulted in the average effective permeability of the wetting phase at different saturations. The results for eight saturation points are shown in Fig. 5.18. As can be seen, there is a good agreement between the Laplace approach and LBM for the whole range of saturations. In addition, due to the stability problem associated with LBM at low saturations, $S_w = 0.3$ is the minimum saturation point which we could calculate permeability for, while the Laplace solver can estimate permeability for saturations down to $S_w = 0.1$. It should be noted that here we used an explicit representation of wetting phase in micropores and macropores where no homogenization applied.

For upscaling through the Laplace equation, however, only the wetting phase in macropores is explicitly resolved for which the EDT map is calculated and the local permeability field is estimated. For the wetting phase in micropores, a similar procedure as Scen 4 (explained earlier) is followed. At each total wetting phase saturation, the volume fraction of the wetting phase in micropores is firstly calculated. Its corresponding permeability is then obtained from the $k_r - S_w$ function for the pure micropore model (see Fig. 5.14). In contrast to the full solution where the local permeability field is estimated from the EDT map of the wetting phase in micropores and macropores, in upscaling mode the wetting phase and solid in micropores are homogenised and replaced with a uniform permeability. This homogenised permeability field in conjunction with the estimated local permeability field in macropores is used for calculating the average effective permeability of the wetting phase.

Fig. 5.19 shows the result of upscaling with the Laplace equation and full solution calculated by LBM. It also compares Laplace approach with MLBM for upscaling effective permeability of the wetting phase. As can be seen in this figure, while MLBM could only be used for upscaling at $S_w > 0.5$, Laplace approach fails to reproduce any result of LBM and the effective permeabilities are significantly underestimated by this method. It is partly due to the high permeability contrast between micropores and macropores. In the estimated voxel-wise local permeability field, which was used in the Laplace approach, the continuity of the velocity at the boundary of the micropores with macropores is not handled properly. In MLBM, in contrast, the transition from micro- to macropores is smooth and the continuity of the velocity at the interface is satisfied (see Fig. 5.8 and Fig. 5.9).

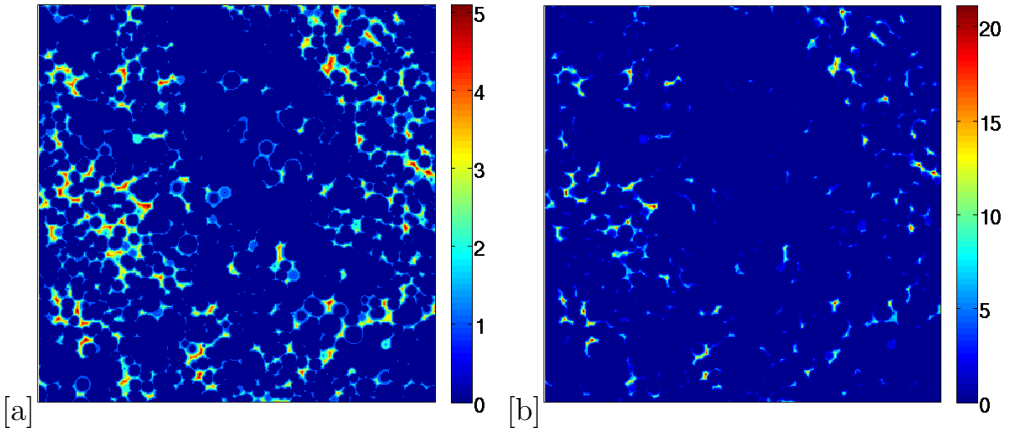

Figure 5.17: An interface of distance map and its corresponding permeability field used by Laplace solver. [a] A 2D slice of a 3D EDT map of wetting phase computed on one realisation of GRF50 at $S_w = 0.39$. [b] A 2D slice of 3D local permeability field estimated from EDT map using Eqn. 5.16.

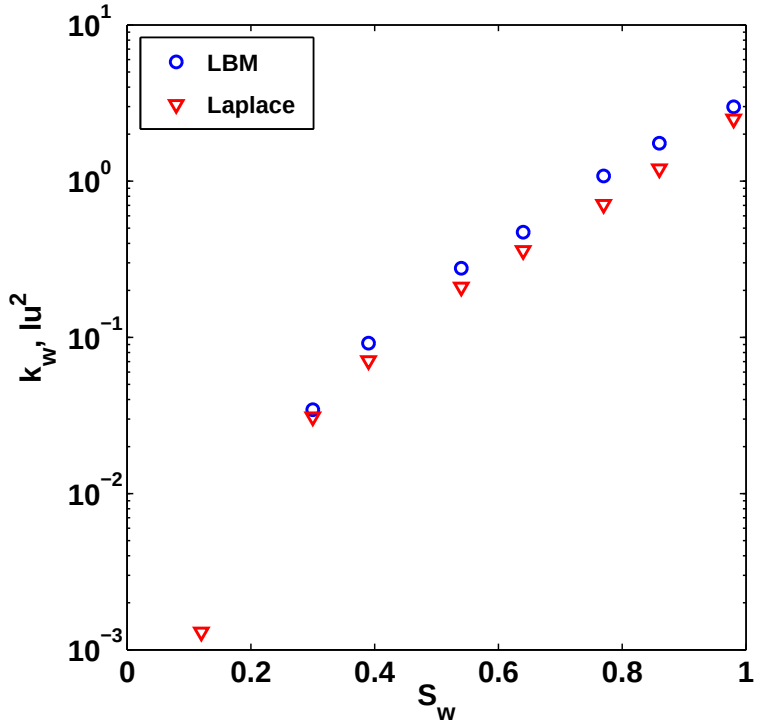

Figure 5.18: Comparing Laplace solver with LBM for one realisation of model GRF50 at different saturations. The model was partially saturated by putting thresholds on CDT map of the pore phase. Local permeability (conductance) used in Laplace solver was estimated based on EDT map of wetting phase at each saturation (see Eqn.5.16).

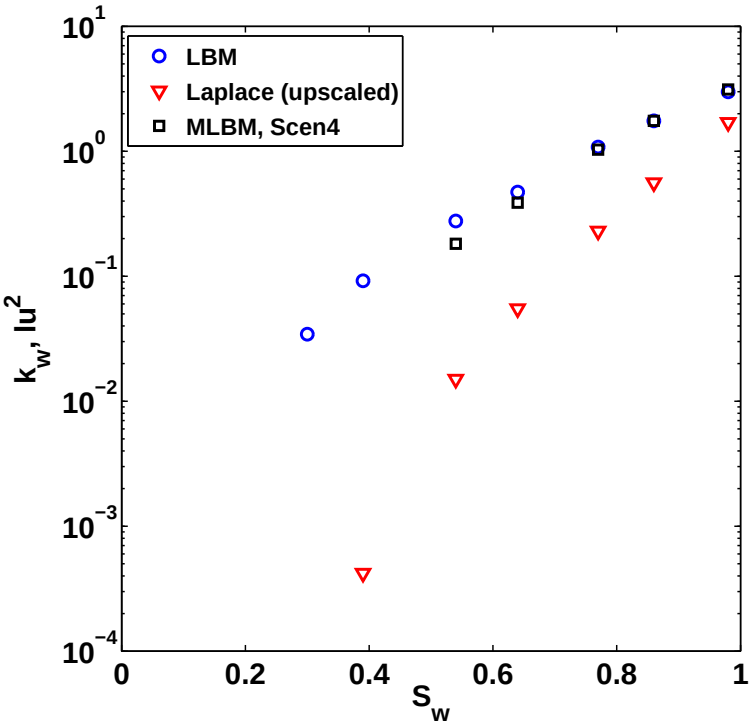

Figure 5.19: Comparing Laplace approach with MLBM for upscaling effective permeability of the wetting phase.

CHAPTER 6

CONCLUSIONS AND FUTURE DIRECTIONS

This chapter concludes this study by providing a summary of the methods and the results of numerical simulations followed by some recommendations for possible future directions.

Image-based fluid flow simulation is tied to the resolution of the acquired images. At any particular resolution, those pores which are smaller than the image resolution will remain unresolved. The significance of the effect of microporosity (sub-resolution pores) on the fluid flow has been repeatedly overlooked. In this thesis, a method was introduced to quantify and couple the effect of sub-resolution pores on the effective permeability of porous media for single phase and two-phase flow.

A novel approach was applied to generate heterogeneous model composites with varying amount of micro- to macro-porosity. Gaussian random fields (GRF) were combined with Boolean models to construct model structures exhibiting a bi-modal pore size distribution. While the large scale heterogeneity was controlled by one-level cuts through the GRF model, the porosity and the permeability of each micro- and macro-phase was controlled by two independent Boolean models. The significance of the effect of microporosity on fluid flow was first examined using a critical length as an estimate of permeability. A flux analysis technique was then applied to quantify the contribution of each pore type on the average permeability of single phase and two-phase flow.

While quantifying the effect of sub-resolution pores is not trivial, coupling their effect with an explicit representation of macropores is more complicated. This is mainly because of the different length scales associated with micropores and macropores. Microporous regions were assumed homogeneous and the Darcy equation solved, while in macropores Stokes equations were taken into account. To couple these equations seamlessly the unified Brinkman equation, which is a combination of Darcy and Stokes equations, was considered. We extended a special type of lattice Boltzmann method, called macroscopic lattice Boltzmann method (MLBM), to 3D while adding a sophisticated labeling technique for the purpose of

regional flux analysis and permeability calculations. This method is able to handle grey scale nodes (sub-resolution pores) in addition to black and white nodes (resolved solid and pore). Based on the permeability of the microporous regions and the fluid viscosity, a momentum sink parameter was defined which controls the momentum reduction at the grey nodes. It should be noted that, only the magnitude of the momentum wa reduced while its direction remained unchanged. No momentum sink was applied at voxels in macropores. The method was successfully implemented for single phase and two-phase flow on 2D and 3D porous media. The framework presented in this dissertation represents the first step in multi-stage upscaling, starting from the pore scale. On the basis of the procedures described and implemented in this study, the following conclusions are drawn:

6.1 Conclusions

- Simulating fluid flow on simple 2D heterogeneous model structures, generated by a percolating channel through a porous matrix, shows that neglecting the effect of porous matrix on the effective permeability of the whole system even for the permeability contrast of the order of 10^4 causes erroneous results. It is also proven that the incorporation of porous matrix in fluid flow could increase the effective permeability of the whole system by almost 80% for a model with channel of width 11 lattice units and for a permeability contrast of 10:1.

- For 3D and heterogeneous systems where both macro and microporosity regions percolate independently, microporosity still plays a significant role in increasing the effective permeability. This was illustrated using critical length argument and also confirmed by permeability calculations using LBM for models with permeability contrasts as low as 10:1.

- For two phase flow, the effect of microporosity on the effective permeability of the wetting phase is more significant at lower wetting phase saturations. However, even at $S_w > 0.9$ and for a permeability contrast of 4:1 between macro- and microporosity, the error of neglecting the microporosity is more than 20% for GRF50 and increases to more than 50% in GRF80 and more than 70% in GRF90.

- For unimodal (homogeneous) rock and single phase flow, a momentum sink parameter can be found over the full range of porosities, resulting in an excellent match between LBM (fine solution) and MLBM (coarse solution) methods.

- For heterogeneous systems the agreement between direct LBM (resolved microstructure) and MLBM again is excellent for the full range of GRF fractions, the latter of which control the amount of micro- versus macro-porosity.

- For a vuggy system with disconnected macro-porosity the predicted permeability using MLBM again shows a good match to the direct calculation using LBM.

- Similar to single phase flow, determination of the momentum sink parameter for the wetting phase in micropores is the main challenge for upscaling relative permeability using MLBM. By developing different scenarios in this study, we showed that how to compute momentum sink parameter using flux analysis technique and also from $k_{rw} - S_w$ relationship for microporosity region.

- For wetting phase saturation down to $S_w = 0.5$, there is a good agreement between MLBM and LBM (resolved microstructure). At lower saturations, the volume fraction of the wetting phase in micropores and associated effective permeability becomes very small, causing the momentum sink parameter to be out of range.

- Although there is an excellent agreement between Laplace approach and LBM in the case of resolved microstructure, the former significantly underestimates the wetting phase permeability in upscaling mode and fails to reproduce LBM results even at high saturations. We attribute this to a failure of coupling the the micro- and macroporosity regions appropriately.

6.2 Future directions

Making heterogeneous model structures with combination of homogeneous Boolean models enabled us to have a locally homogeneous saturation distribution. It was especially important in microporous regions where the wetting phase was homogenised and assigned a constant momentum sink parameter. For models with heterogeneous microstructure, a field of momentum sink parameters would be needed to capture the local variation in wetting phase saturation and consequently its effective permeability.

The approach proposed in this study was applied on the images of two relatively homogeneous sandstone rocks. For heterogeneous porous media, we simulated porous media with bi-modal pore size distributions. To prove the significance of

the effect of microporosity, model structures with varying amount of micro-to-macro porosity were an excellent option. While it is straightforward to apply the procedure proposed in this study on the images of real heterogeneous rock materials, it requires multiscale imaging techniques to acquire information of pores at different length scales.

Although we used the same value for μ and μ_e in solving Brinkman equation using MLBM, the approach we used can describe the general case of $\mu/\mu_e \neq 1$ [115]. However for very high permeability contrast between micro- and macro-porosity, it is highly recommended to implement a LBM with multiple relaxation time (MRT). This in conjunction with larger lattices may help to alleviate the constraint on the momentum sink parameters, especially at low wetting phase saturations in microporosity regions.

BIBLIOGRAPHY

[1] P. M. Adler. Porous Media: Geometry and Transports. Butterworth-Heinmann, 1992.

[2] P. M. Adler, C. G. Jacquin, and J. A. Quiblier. Flow in simulated porous media. Int. J. of Multiphase Flow, 16:691–712, 1990.

[3] F. G. Alabert and B. Corre. Heterogeneity in a complex turbiditic reservoir: Impact on field development. In SPE Annual Technical Conference and Exhibition. Society of Petroleum Engineers, 1991.

[4] F. E. Alvarado, A. S. Grader, O. Karacan, and P. M. Halleck. Visualization of three phases in porous media using micro computed tomography. PETROPHYSICS-HOUSTON-, 45:490–498, 2004.

[5] V. Ambegaokar, B. Halperin, and J. S. Langer. Hopping conductivity in disordered systems. Phys. Rev. B, 4:2612–2620, 1971.

[6] Todd Arbogast and Dana S. Brunson. A computational method for approximating a Darcy–Stokes system governing a vuggy porous medium. Computational Geosciences, 11(3):207–218, 2007.

[7] Todd Arbogast and Heather L. Lehr. Homogenization of a Darcy–Stokes system modelling vuggy porous media. Computational Geosciences, 10(3):291–302, 2006.

[8] C. H. Arns and P. M. Adler. A fast Laplace solver approach to pore scale permeability. Phys. Rev. Lett, 2012.

[9] C. H. Arns, M. A. Knackstedt, and N. Martys. Cross-property correlations and permeability estimation in sandstone. Phys. Rev. E, 72:046304, 2005.

[10] C. H. Arns, M. A. Knackstedt, W. V. Pinczewski, and W. B. Lindquist. Accurate estimation of transport properties from microtomographic images. Geophys. Res. Lett., 28(17):3361–3364, 2001.

[11] C. H. Arns, M. A. Knackstedt, W. V. Pinczewski, and K. R. Mecke. Euler-Poincaré characteristics of classes of disordered media. Phys. Rev. E, 63:031112:1–13, 2001.

[12] C. H. Arns, J. Mecke, K. R. Mecke, and D. Stoyan. Second-order analysis by variograms for curvature measures of two-phase structures. Europ. Phys. J. B: Cond. Matt., 47(3):397–409, 2005.

[13] C. H. Arns, A. Sakellariou, T. J. Senden, A. P. Sheppard, R. Sok, W. V. Pinczewski, and M. A. Knackstedt. Digital core laboratory: Reservoir core analysis from 3D images. Petrophysics, 46(4):260–277, 2005.

[14] C. H. Arns, A. Sakellariou, T. J. Senden, A. P. Sheppard, R. M. Sok, W. V. Pinczewski, and M. A. Knackstedt. Petrophysical properties derived from X-ray CT images. APPEA Journal, 43:577–586, 2003.

[15] Christoph H. Arns. The influence of morphology on physical properties of reservoir rocks. PhD thesis, University of New South Wales, 2002.

[16] Christoph H. Arns, Mark A. Knackstedt, W. Val Pinczewski, and E. G. Garboczi. Computation of linear elastic properties from microtomographic images: Methodology and agreement between theory and experiment. Geophysics, 67(5):1396–1405, 2002.

[17] F. M. Auzerais, J. Dunsmuir, B. B. Ferrèol, N. Martys, J. Olson, T. S. Ramakrishnan, D. H. Rothman, and L. M. Schwartz. Transport in sandstone: A study based on three dimensional microtromography. Geophysical Research Letters, 23(7):705–708, April 1996.

[18] K. Balasubramanian, F. Hayot, and W. F. Saam. Darcys law from lattice-gas hydrodynamics. Physical Review A, 36(5):2248, 1987.

[19] Christopher A. Baldwin, Andrew J. Sederman, Michael D. Mantle, Paul Alexander, and Lynn F. Gladden. Determination and characterization of the structure of a pore space from 3D volume images. Journal of Colloid and Interface Science, 181(1):79–92, 1996.

[20] Jayanth R. Banavar and Lawrence M. Schwartz. Magnetic resonance as a probe of permeability in porous media. Phys. Rev. Lett., 58:1411–1414, 1987.

[21] John W. Barker and Philippe Dupouy. An analysis of dynamic pseudo-relative permeability methods for oil-water flows. Petroleum Geoscience, 5(4):385–394, 1999.

[22] D. Bauer, S. Youssef, M. Fleury, S. Bekri, E. Rosenberg, and O. Vizika. Improving the estimations of petrophysical transport behavior of carbonate rocks using a dual pore network approach combined with computed microtomography. Transport in porous media, 94(2):505–524, 2012.

[23] J. Bear. Dynamics of Fluids in Porous Media. Elsevier, 1972.

[24] Gordon S. Beavers and Daniel D. Joseph. Boundary conditions at a naturally permeable wall. Journal of fluid mechanics, 30(01):197–207, 1967.

[25] S. H. Begg, R. R. Carter, and P. Dranfield. Assigning effective values to simulator gridblock parameters for heterogeneous reservoirs. SPE Reservoir Engineering, 4(04):455–463, 1989.

[26] S. Bekri, C. Laroche, and O. Vizika. Pore network models to calculate transport and electrical properties of single or dual-porosity rocks. In international symposium of the society of core analysts, Toronto, 2005.

[27] D. P. Bentz and N. S. Martys. Hydraulic radius and transport in reconstructed model three-dimensional porous media. Transport in Porous Media, 17:221–238, 1994.

[28] N. F. Berk. Scattering properties of a model bicontinuous structure with a well defined length scale. Phys. Rev. Lett., 58:2718–2721, 1987.

[29] N. F. Berk. Scattering properties of the leveled-wave model of random morphologies. Phys. Rev. A, 44:5069–5079, 1991.

[30] Brian Berkowitz and David P. Hansen. A numerical study of the distribution of water in partially saturated porous rock. Transport in porous media, 45(2):301–317, 2001.

[31] Prabhu L. Bhatnagar, Eugene P. Gross, and Max Krook. A model for collision processes in gases. i. small amplitude processes in charged and neutral one-component systems. Physical review, 94(3):511, 1954.

[32] H. Bieri and W. Nef. Algorithms for the Euler characteristic and related additive functionals. Comput. Vision, Graphics and Image Proc., 28:166–175, 1984.

[33] R. B. Bird, W. E. Stewart, and E. N. Lightfoot. Transport phenomena. John Wiley & Sons, 2007.

[34] B. Biswal, P. E. Oren, R. J. Held, S. Bakke, and R. Hilfer. Stochastic multiscale model for carbonate rocks. Phys. Rev. E, 75(061303), 2007.

[35] Martin J. Blunt. Flow in porous media–pore-network models and multiphase flow. Current opinion in colloid & interface science, 6(3):197–207, 2001.

[36] Martin J. Blunt, Branko Bijeljic, Hu Dong, Oussama Gharbi, Stefan Iglauer, Peyman Mostaghimi, Adriana Paluszny, and Christopher Pentland. Pore-scale imaging and modelling. Advances in Water Resources, 51:197–216, 2013.

[37] Mary L. Bouxsein, Stephen K. Boyd, Blaine A. Christiansen, Robert E. Guldberg, Karl J. Jepsen, and Ralph Müller. Guidelines for assessment of bone microstructure in rodents using micro–computed tomography. Journal of bone and mineral research, 25(7):1468–1486, 2010.

[38] John J. Buckles, Randy D. Hazlett, Shiyi Chen, Kenneth G. Eggert, Daryl W. Grunau, and Wendy E. Soll. Toward improved prediction of reservoir flow performance. Los Alamos Science, 22:112–121, 1994.

[39] J. M. Buick and C. A. Greated. Gravity in a lattice boltzmann model. Physical Review E, 61(5):5307, 2000.

[40] John W. Cahn. Phase separation by spinodal decomposition in isotropic systems. J. Chem. Phys., 42:93–99, 1965.

[41] Philip Crosbie Carman. Flow of gases through porous media. Butterworths Scientific Publications London, 1956.

[42] C. T. Chang, Jinli Qiao, Songhua Chen, and A. Ted Watson. Fracture characterization with NMR spectroscopic techniques. Journal of Magnetic Resonance, 126(2):213–220, 1997.

[43] Shiyi Chen and Gary D. Doolen. Lattice Boltzmann method for fluid flows. Annu. Rev. Fluid Mech., 30:329–364, 1998.

[44] M. A. Christie. Upscaling for reservoir simulation. Journal of Petroleum Technology, 48(11):1–004, 1996.

[45] M. E. Coles, R. D. Hazlett, P. Spanne, W. E. Soll, E. L. Muegge, and K. W. Jones. Pore level imaging of fluid transport using synchrotron X-ray microtomography. Journal of Petroleum Science and Engineering, 19(1-2):55–63, 1998.

[46] Rémi Cornubert, Dominique d'Humières, and David Levermore. A Knudsen layer theory for lattice gases. Physica D: Nonlinear Phenomena, 47(1):241–259, 1991.

[47] P. Anthony Crossley, Lawrence M. Schwartz, and Jayanth R. Banavar. Image-based models of porous media: Application to vycor glass and carbonate rocks. Applied physics letters, 59(27):3553–3555, 1991.

[48] Orla Dardis and John McCloskey. Lattice boltzmann scheme with real numbered solid density for the simulation of flow in porous media. Physical Review E, 57(4):4834, 1998.

[49] Orla Dardis and John McCloskey. Permeability porosity relationships from numerical simulations of fluid flow. Geophysical research letters, 25(9):1471–1474, 1998.

[50] C. J. G. Darnault, D. A. DiCarlo, T. W. J. Bauters, A. R. Jacobson, J. A. Throop, C. D. Montemagno, J. Y. Parlange, and T. S. Steenhuis. Measurement of fluid contents by light transmission in transient three-phase oil-water-air systems in sand. Water Resources Research, 37(7):1859–1868, 2001.

[51] D. B. Das and S. M. Hassanizadeh. Upscaling Multiphase Flow in Porous Media. Springer, 2005.

[52] E. Dezabala and J. Kamath. Laboratory evaluation of waterflood behavior of vugular carbonates. In SPE Annual Technical Conference and Exhibition, 1995.

[53] F. A. L. Dullien. Porous Media: Fluid Transport and Pore Structure. Academic Press, New York, 2 edition, 1992.

[54] L. Durlofsky and J. F. Brady. Analysis of the Brinkman equation as a model for flow in porous media. Physics of Fluids, 30(11):3329–3341, 1987.

[55] L. J. Durlofsky, Richard C. Jones, and William J. Milliken. A new method for the scale up of displacement processes in heterogeneous reservoirs. In 4th European Conference on the Mathematics of Oil Recovery, 1994.

[56] S. Ekrann and J. O. Aasen. Steady-state upscaling. Transport in Porous Media, 41(3):245–262, 2000.

[57] M. Feali, W. V. Pinczewski, Y. Cinar, C. H. Arns, J. Y. Arns, N. Francois, M. Turner, T. Senden, and M. Knackstedt. Qualitative and quantitative analyses of the three-phase distribution of oil, water, and gas in Bentheimer sandstone by use of micro-CT imaging. SPE Reservoir Evaluation & Engineering, 15(6):706–711, 2012.

[58] Mostafa Feali. characterisation of three-phase fluid distributions in a porous rock using micro computed tomography. PhD thesis, University of New South Wales, 2013.

[59] Stanley Osher Ronald Fedkiw. Level set methods and dynamic implicit surfaces. 2003.

[60] B. Ferreol and D. H. Rothman. Lattice-Boltzmann simulations of flow through Fontainebleau sandstone. Transport in Porous Media, 20:3–20, 1995.

[61] B. P. Flannery, H. W. Deckman, W. G. Roberge, and K. L. D'Amico. Three-dimensional X-ray microtomography. Science, 237:1439–1444, 1987.

[62] J. T. Fredrich. 3D imaging of porous media using laser scanning confocal microscopy with application to microscale transport processes. Phys. Chem. Earth (A), 24(7):551–561, 1999.

[63] J. T. Fredrich. 3D imaging of porous media using laser scanning confocal microscopy with application to microscale transport processes. Physics and Chemistry of the Earth, Part A: Solid Earth and Geodesy, 24(7):551–561, 1999.

[64] David M. Freed. Lattice-boltzmann method for macroscopic porous media modelling. International Journal of Modern Physics C, 9(08):1491–1503, 1998.

[65] U. Frisch, B. Hasslacher, and Y. Pomeau. Lattice-gas automata for the Navier-Stokes equation. Physical review letters, 56:1505–1508, 1986.

[66] A. N. Galani, M. E. Kainourgiakis, N. I. Papadimitriou, A. T. Papaioannou, and A. K. Stubos. Investigation of transport phenomena in porous structures containing three fluid phases. Colloids and Surfaces A: Physicochemical and Engineering Aspects, 300(1):169–179, 2007.

[67] Y. Gao and M. M. Sharma. A LGA model for fluid flow in heterogeneous porous media. Transport in Porous Media, 17(1):1–17, 1994.

[68] Abid Ghous. 3D Imaging and modelling of carbonate core at multiple scales. PhD thesis, University of New South Wales, 2010.

[69] D. Grunau, S. Chen, and K. Eggert. A lattice Boltzmann model for multiphase fluid flows. Physics of Fluids A: Fluid Dynamics (1989-1993), 5(10):2557–2562, 1993.

[70] A. F. Gulbransen, V. L. Hauge, and K. Lie. A multiscale mixed finite element method for vuggy and naturally fractured reservoirs. In SPE Reservoir Simulation Symposium. SPE119104-MS, 2009.

[71] Andrew K. Gunstensen and Daniel H. Rothman. Lattice Boltzmann model of immiscible fluids. Phys. Rev. A, 43(8):4320–4327, 1991.

[72] Z. Guo, C. Zheng, and B. Shi. Discrete lattice effects on the forcing term in the lattice Boltzmann method. PHYSICAL REVIEW E Phys Rev E, 65:046308, 2002.

[73] Helge H. Haldorsen and Larry W. Lake. A new approach to shale management in field-scale models. Society of Petroleum Engineers Journal, 24(4):447–457, 1984.

[74] R. D. Hazlett. Simulation of capillary-dominated displacements in microtomographic images of reservoir rocks. Transport in Porous Media, 20(1-2):21–35, 1995.

[75] M. Hilpert and C. T. Miller. Pore-morphology based simulation of drainage in totally wetting porous media. Advances in Water Resources, 24:243–255, 2001.

[76] M. M. Honarpour, F. Koederitz, and A. Herbert. Relative permeability of petroleum reservoirs. CRC Press Inc, Boca Raton, FL, 1986.

[77] Ulrich Hornung. Homogenization and porous media, volume 6. Springer, 1997.

[78] H. Huang, D. Thorne Jr., M. G. Schaap, and M. C. Sukop. Proposed approximation for contact angles in Shan-and-Chen-type multicomponent multiphase lattice Boltzmann models. Phys. Rev. E, 76(066701), 2007.

[79] F. Hussain, W. V. Pinczewski, Y. Cinar, J. Y. Arns, C. H. Arns, and M. L. Turner. Computation of relative permeability from imaged fluid distributions at the pore scale. Transport in Porous Media, pages 1–17, 2014.

[80] M. A. Ioannidis and I. Chatzis. A dual-network model of pore structure for vuggy carbonates. In SCA2000-09, International Symposium of the Society of Core Analysts, Abu Dhabi, UAE, 2000.

[81] Z Jiang, MIJ Dijke, KS Sorbie, and GD Couples. Representation of multiscale heterogeneity via multiscale pore networks. Water Resources Research, 49(9):5437–5449, 2013.

[82] M. E. Kainourgiakis, E. S. Kikkinides, G. C. Charalambopoulou, and A. K. Stubos. Simulated annealing as a method for the determination of the spatial distribution of a condensable adsorbate in mesoporous materials. Langmuir, 19(8):3333–3337, 2003.

[83] Q. Kang, D. Zhang, and S. Chen. Unified lattice Boltzmann method for flow in multiscale porous media. Phys. Rev. E, 66:056307, 2002.

[84] A. J. Katz and A. H. Thompson. Quantitative prediction of permeability in porous rock. Phys. Rev. B, 34(11):R8179–R8181, 1986.

[85] Arturo A. Keller, Martin J. Blunt, and Arturo Paul V. Roberts. Micromodel observation of the role of oil layers in three-phase flow. Transport in Porous Media, 26(3):277–297, 1997.

[86] W. E. Kenyon. Nuclear magnetic resonance as a petrophysical measurement. Nucl. Geophys., 6:153–171, 1992.

[87] W. E. Kenyon, P. Day, C. Straley, and J. Willemsen. Compact and consistent representation of rock NMR data from permeability estimation. In Proc. 61st Annual Technical Conference and Exhibition, New Orleans, 1986. SPE 15643.

[88] W. E. Kenyon, P. Day, C. Straley, and J. Willemsen. A three part study of NMR longitudinal relaxation properties of water saturated sandstones. SPE formation evaluation, 3(3):626–636, SPE 15643, 1988.

[89] A. R. A. Khaled and K. Vafai. The role of porous media in modelling flow and heat transfer in biological tissues. International Journal of Heat and Mass Transfer, 46(26):4989–5003, 2003.

[90] Ahmad Dehghan Khalili. Transport properties for heterogeneous carbonate rocks. PhD thesis, University of New South Wales, 2013.

[91] Sangtae Kim and William B. Russel. Modelling of porous media by renormalization of the Stokes equations. Journal of Fluid Mechanics, 154:269–286, 1985.

[92] P. R. King. The use of renormalization for calculating effective permeability. Transport in porous media, 4(1):37–58, 1989.

[93] Scott Kirkpatrick, D. Gelatt Jr., and Mario P. Vecchi. Optimization by simmulated annealing. science, 220(4598):671–680, 1983.

[94] M. A. Knackstedt, C. H. Arns, A. Ghous, T. J. Senden, A. P. Sheppard, R. M. Sok, V. Nguyen, and W. V. Pinczewski. 3D imaging and characterization of the pore space of carbonates core; implications to single and two phase flow properties. In 47th Annual Logging Symposium, Veracruz, Mexico, June 2006. Society of Petrophysicists & Well Log Analyst.

[95] M. A. Knackstedt, C. H. Arns, A. Limaye, A. Sakellariou, T. J. Senden, A. P. Sheppard, R. M. Sok, W. V. Pinczewski, and G. F. Bunn. Digital core laboratory: Properties of reservoir core derived from 3D images. In Asia Pacific Conference on Integrated Modelling for Asset Management, page SPE 87009, Kuala Lumpur, March 2004. SPE 87009.

[96] M. A. Knackstedt, C. H. Arns, T. J. Senden, and K. Gross. Structure and properties of clinical coralline implants measured via 3D imaging and analysis. Biomaterials, 27(13):2776–2786, 2006.

[97] M. A. Knackstedt and A. P. Roberts. Morphology and macroscopic properties of conducting polymer blends. Macromolecules, 29:1369–1371, 1996.

[98] M. A. Knackstedt, R. Sok, A. Sheppard, and C. H. Arns. 3D pore scale characterisation of carbonate core: Relating pore types and interconnectivity to petrophysical and multiphase flow properties. In International Petroleum Technology Conference. International Petroleum Technology Conference, 2007.

[99] R. Knight, A. Chapman, and M. Knoll. Numerical modelling of microscopic fluid distribution in porous media. Journal of applied physics, 68(3):994–1001, 1990.

[100] Josef Kozeny. Ueber kapillare leitung des wassers im boden. Sitzungsber. Akad. Wiss. Wien, 136:271–306, 1927.

[101] Arun T. A. Kumar, Paul D. Majors, and W. R. Rossen. Measurement of aperture and multiphase flow in fractures using NMR imaging. SPE Formation Evaluation, 12(02):101–108, 1997.

[102] Munish Kumar. Multiphase flow in reservoir cores using digital core analysis. PhD thesis, Australian National University, 2009.

[103] Munish Kumar, Tim Senden, Mark A. Knackstedt, Shane J. Latham, Val Pinczewski, Robert M. Sok, Adrian P. Sheppard, and Michael L. Turner. Imaging of pore scale distribution of fluids and wettability. Petrophysics, 50(4):311, 2009.

[104] Munish Kumar, Rob Sok, Mark A. Knackstedt, Shane Latham, Tim J. Senden, Adrian P. Sheppard, Trond Varslot, and Christoph H. Arns. Mapping fluid distributions in 3D at the pore scale: Quantifying the influence of wettability and saturation history on rock resistivity. In 50th Annual Logging Symposium, pages paper SSS:1–16, The Woodlands, Texas, June 2009. Society of Petrophysicists & Well Log Analyst.

[105] A. J. C. Ladd and R. Verberg. Lattice-boltzmann simulations of particle-fluid suspensions. Journal of Statistical Physics, 104(5-6):1191–1251, 2001.

[106] Jonas Latt, Bastien Chopard, Orestis Malaspinas, Michel Deville, and Andreas Michler. Straight velocity boundaries in the lattice boltzmann method. Physical Review E, 77(5):056703, 2008.

[107] M. Latva-Kokko and Daniel H. Rothman. Diffusion properties of gradient-based lattice Boltzmann models of immiscible fluids. Physical Review E, 71(5):056702, 2005.

[108] Pierre Le Doussal. Permeability versus conductivity for porous media with wide distribution of pore sizes. Phys. Rev. B, 39(7):R4816–R4819, 1989.

[109] I. Ligaarden, M. Krotkiewski, K. A. Lie, M. Pal, and D. Schmid. On the Stokes-Brinkman equations for modelling flow in carbonate reservoirs. In 12th European Conference on the Mathematics of Oil Recovery, 2010.

[110] Ajay Limaye. Volume exploration and presentation tool, 2006. Poster presentation, Vis 2006, Baltimore.

[111] C. Lin and M. H. Cohen. Quantitative methods for microgeometric modelling. Journal of Applied Physics, 53(6):4152–4165, 1982.

[112] W. B. Lindquist and A. Venkatarangan. Investigating 3D geometry of porous media from high resolution images. Phys. Chem. Earth (A), 25:593–599, 1999.

[113] M. D. Mantle, A. J. Sederman, and L. F. Gladden. Single-and two-phase flow in fixed-bed reactors: MRI flow visualisation and lattice-Boltzmann simulations. Chemical Engineering Science, 56(2):523–529, 2001.

[114] C. Manwart, U. Aaltosalmi, A. Koponen, R. Hilfer, and J. Timonen. Lattice-Boltzmann and finite-difference simulations for the permeability for three-dimensional porous media. Phys. Rev. E, 66:016702:1–11, 2002.

[115] N. S. Martys. Improved approximation of the Brinkman equation using a lattice Boltzmann method. Phys. Fluids, 13(6):1807–1810, 2001.

[116] N. S. Martys and Hudong Chen. Simulation of multicomponent fluids in complex three-dimensional geometries by the lattice Boltzmann method. Phys. Rev. E, 53(1):743–750, 1996.

[117] N. S. Martys and E. J. Garboczi. Length scales relating the fluid permeability and electrical conductivity in random two-dimensional model porous media. Phys. Rev. B, 46:6080–6090, 1992.

[118] N. S. Martys, S. Torquato, and D. P. Bentz. Universal scaling of fluid permeability for sphere packings. Phys. Rev. E, 50:403, 1994.

[119] Nicos S. Martys, Xiaowen Shan, and Hudong Chen. Evaluation of the external force term in the discrete Boltzmann equation. Phys. Rev. E, 58(5):6855–6857, 1998.

[120] S. Marčelja. Localized random wave description of continuous microemulsions. J. Physical Chem., 94:7259–7261, 1990.

[121] Calvin C. Mattax and Robert L. Dalton. Reservoir simulation. Journal of petroleum technology, 42(6):692–695, 1990.

[122] A. Mehmani, M. Prodanović, and F. Javadpour. Multiscale, multiphysics network modelling of shale matrix gas flows. Transport in porous media, 99(2):377–390, 2013.

[123] A. Mehmani, A. Tokan-Lawal, M. Prodanovic, and A. Sheppard. The effect of microporosity on transport properties in tight reservoirs. In North American Unconventional Gas Conference and Exhibition. Society of Petroleum Engineers, 2011.

[124] Ayaz Mehmani and Maša Prodanović. The effect of microporosity on transport properties in porous media. Advances in Water Resources, 63:104–119, 2014.

[125] A. Moctezuma-Berthier, S. Bekri, C. Laroche, and O. Vizika. A dual network model for relative permeability of bimodal rocks application in a vuggy carbonate. In Intl. Symp. of the Society of Core Analysts, 2003.

[126] A. Moctezuma-Berthier, O. Vizika, and P. M. Adler. Macroscopic conductivity of vugular porous media. Transport in Porous Media, 49:331–332, 2002.

[127] A. Moctezuma-Berthier, O. Vizika, J. F. Thovert, and P. M. Adler. One-and two-phase permeabilities of vugular porous media. transport in porous Media, 56(2):225–244, 2004.

[128] K. Mogensen, E. H. Stenby, and D. Zhou. Studies of waterflooding in low-permeable chalk by use of X-ray CT scanning. Journal of Petroleum Science and Engineering, 32(1):1–10, 2001.

[129] Carlo D. Montemagno and William G. Gray. Photoluminescent volumetric imaging: A technique for the exploration of multiphase flow and transport in porous media. Geophysical research letters, 22(4):425–428, 1995.

[130] Annette P. Mortensen, Robert J. Glass, Karl Hollenbeck, and Karsten H. Jensen. Visualization of microscale phase displacement processes in retention and outflow experiments: nonuniqueness of unsaturated flow properties. Water Resources Research, 37(6):1627–1640, 2001.

[131] P. E. Øren and W. V. Pinczewski. Fluid distribution and pore-scale displacement mechanisms in drainage dominated three-phase flow. Transport in Porous Media, 20(1-2):105–133, 1995.

[132] Pål Eric Øren and Stig Bakke. Process based reconstruction of sandstones and prediction of transport properties. Transport in Porous Media, 46(2):311–343, 2002.

[133] Stanley Osher and James A Sethian. Fronts propagating with curvature-dependent speed: algorithms based on hamilton-jacobi formulations. Journal of computational physics, 79(1):12–49, 1988.

[134] C. Pan, M. Hilpert, and C. T. Miller. Lattice-Boltzmann simulation of two-phase flow in porous media. Water Resources Research, 40(1), 2004.

[135] Chongxun Pan. Use of pore-scale modelling to understand flow and transport in porous media. PhD thesis, University of North Carolina, 2003.

[136] Chongxun Pan, Li-Shi Luo, and Cass T. Miller. An evaluation of lattice Boltzmann schemes for porous medium flow simulation. Computers & Fluids, 35:898–909, 2006.

[137] M. S. Paterson. The equivalent channel model for permeability and resistivity in fluid-saturated rock: A re-appraisal. Mechanics of Materials, 2(4):345–352, 1983.

[138] G. G. Pereira. Numerical pore-scale modelling of three-phase fluid flow: Comparison between simulation and experiment. Physical Review E, 59(4):4229, 1999.

[139] PetroWiki. Relative permeability models, 2013. available online: http://petrowiki.org/index.php?title=Relative_permeability_models&oldid=41069 (accessed on 25 March 2014).

[140] G. E. Pickup, K. D. Stephen, J. Ma, P. Zhang, and J. D. Clark. Multistage upscaling: Selection of suitable methods. Transport in porous media, 58(1-2):191–216, 2005.

[141] Mohammad Piri and Martin J. Blunt. Three-dimensional mixed-wet random pore-scale network modelling of two-and three-phase flow in porous media. i. model description. Physical Review E, 71(2):026301, 2005.

[142] Maurice G. Politis, Michael E. Kainourgiakis, Eustathios S. Kikkinides, and Athanasios K. Stubos. Application of simulated annealing on the study of multiphase systems.

[143] P. Popov, G. Qin, L. Bi, Y. Efendiev, R. E. Ewing, and J. Li. Multiphysics and multiscale methods for modelling fluid flow through naturally fractured carbonate karst reservoirs. SPE Reservoir Evaluation & Engineering, 12(02):218–231, 2009.

[144] Maša Prodanović and Steven L. Bryant. A level set method for determining critical curvatures for drainage and imbibition. Journal of colloid and interface science, 304(2):442–458, 2006.

[145] Maša Prodanović, Ayaz Mehmani, and Adrian P. Sheppard. Imaged-based multiscale network modelling of microporosity in carbonates. Geological Society, London, Special Publications, 406, 2014.

[146] Jafar Qajar. Reactive flow in carbonate cores via digital core analysis. PhD thesis, The University of New South Wales, 2012.

[147] Jafar Qajar, Nicolas Francois, Christoph Hermann Arns, et al. Microtomographic characterization of dissolution-induced local porosity changes including fines migration in carbonate rock. SPE Journal, 18(03):545–562, 2013.

[148] Y. H. Qian, D. d'Humières, and P. Lallemand. Lattice BGK models for Navier-Stokes equation. Europhysics Lett., 17(6):479, 1992.

[149] Y. H. Qian and Y. Zhou. Complete Galilean-invariant lattice BGK models for the Navier-Stokes equation. Europhys. Lett., 42(4):359–364, 1998.

[150] G. Qin, B. Gong, L. Bi, and X. Wu. Multi-scale and multi-physics methods for numerical modelling of fluid flow in fractured formations. In SPE EUROPEC/EAGE Annual Conference and Exhibition. SPE143590-MS, 2011.

[151] J. A. Quiblier. A new three-dimensional modelling technique for studying porous media. J. Colloid Interface Sci., 98:84–102, 1984.

[152] T. Ramstad, N. Idowu, C. Nardi, and P. E. Øren. Relative permeability calculations from two-phase flow simulations directly on digital images of porous rocks. Transport in porous media, 94(2):487–504, 2012.

[153] Ph. Renard and G. De Marsily. Calculating equivalent permeability: a review. Advances in Water Resources, 20(5):253–278, 1997.

[154] A. P. Roberts. Statistical reconstruction of three-dimensional porous media from two-dimensional images. Phys. Rev. E, 56:3203–3212, 1997.

[155] A. P. Roberts and E. J. Garboczi. Elastic properties of model porous ceramics. J. Amer. Ceramic Society, 83(12):3041–3048, 2000.

[156] A. P. Roberts and M. Knackstedt. Mechanical and transport properties of model foamed solids. J. Materials Sci. Letters, 14:1357–1359, 1995.

[157] A. P. Roberts and M. A. Knackstedt. Structure-property correlations in model composite materials. Phys. Rev. E, 54:2313–2328, 1996.

[158] A. P. Roberts and M. Teubner. Transport properties of heterogeneous materials derived from Gaussian random fields: Bounds and simulation. Phys. Rev. E, 51:4141–4154, 1995.

[159] Daniel H. Rothman and Jeffrey M. Keller. Immiscible cellular-automaton fluids. Journal of Statistical Physics, 52(3-4):1119–1127, 1988.

[160] N. Saad, A. S. Cullick, and M. M. Honarpour. Effective relative permeability in scale-up and simulation. In Rocky mountain rgional/low permeability reservoirs symposium, pages 451–464, 1995.

[161] R. B. Saeger, L. E. Scriven, and H. T. Davis. Flow, conduction, and a characteristic length in bicontinuous periodic media. Phys. Rev. A, 44:5087–5090, 1991.

[162] Muhammad Sahimi. Flow and transport in porous media and fractured rock: from classical methods to modern approaches. John Wiley & Sons, 2012.

[163] Arthur Sakellariou, Christoph H. Arns, Adrian P. Sheppard, Rob M. Sok, Holger Averdunk, Ajay Limaye, Anthony C. Jones, Tim J. Senden, and Mark A. Knackstedt. Developing a virtual materials laboratory. Materials Today, 10(12):44–51, 2007.

[164] Hamidreza Salimi and Johannes Bruining. Upscaling in partially fractured oil reservoirs using homogenization. In SPE/EAGE Reservoir Characterization & Simulation Conference, 2009.

[165] Marcel G. Schaap and Inma Lebron. Using microscope observations of thin sections to estimate soil permeability with the Kozeny–Carman equation. Journal of Hydrology, 251(3):186–201, 2001.

[166] Adrian E. Scheidegger. The physics of flow through porous media. Soil Science, 86(6):355, 1958.

[167] G. Schnaar and M. L. Brusseau. Characterizing pore-scale configuration of organic immiscible liquid in multiphase systems with synchrotron X-ray microtomography. Vadose Zone Journal, 5(2):641–648, 2006.

[168] L. M. Schwartz, N. Martys, D. P. Bentz, E. J. Garboczi, and S. Torquato. Cross-property relations and permeability estimation in model porous media. Phys. Rev. E, 48(6):4584–4591, 1993.

[169] Jean Serra. Image analysis and mathematical morphology, volume 1,2. Academic Press, Amsterdam, 1982.

[170] James Albert Sethian. Level set methods and fast marching methods: evolving interfaces in computational geometry, fluid mechanics, computer vision, and materials science, volume 3. Cambridge university press, 1999.

[171] Vahid Shabro, Masa Prodanovic, Christoph H. Arns, Steven L. Bryant, Carlos Torres-Verdin, and Mark A. Knackstedt. Pore scale modelling of two-phase flow. In J. Carrera, editor, XVIII International Conference on Water Resources, CIMNE, Barcelona, 2010.

[172] Vahid Shabro, Carlos Torres-Verdín, Farzam Javadpour, and Kamy Sepehrnoori. Finite-difference approximation for fluid-flow simulation and calculation of permeability in porous media. Transport in porous media, 94(3):775–793, 2012.

[173] Xiaowen Shan and Hudong Chen. Lattice Boltzmann model for simulating flows with multiple phases and components. Phys. Rev. E, 47(3):1815–1819, 1993.

[174] Xiaowen Shan and Hudong Chen. Simulation of nonideal gases and liquid-gas phase transitions by the lattice Boltzmann equation. Physical Review E, 49(4):2941, 1994.

[175] Adrian P. Sheppard, Rob M. Sok, and Holger Averdunk. Techniques for image enhancement and segmentation of tomographic images of porous materials. Physica A, 339(1-2):145–151, 2004.

[176] David L. Silverstein and Tomlinson Fort. Incorporating low hydraulic conductivity in a numerical model for predicting air-water interfacial area in wet unsaturated particulate porous media. Langmuir, 16(2):835–838, 2000.

[177] David L. Silverstein and Tomlinson Fort. Prediction of water configuration in wet unsaturated porous media. Langmuir, 16(2):839–844, 2000.

[178] E. H. Smith. The influence of small-scale heterogeneity on average relative permeability. RESERVOIR CHARACTERIZATION II Z, page 52, 1991.

[179] David Tunison Snow. A parallel plate model of fractured permeable media. PhD thesis, University of California, Berkeley, 1965.

[180] Robert M Sok, Trond Varslot, Abid Ghous, Shane Latham, Adrian P Sheppard, and Mark A Knackstedt. Pore scale characterization of carbonates at multiple scales: Integration of micro-ct, bsem, fibsem. Petrophysics, 51(6):379, 2010.

[181] W. E. Soll, M. A. Celia, and J. L. Wilson. Micromodel studies of three-fluid porous media systems: Pore-scale processes relating to capillary pressure-saturation relationships. Water resources research, 29(9):2963–2974, 1993.

[182] Michael A. A. Spaid and Frederick R. Phelan, Jr. Lattice Boltzmann methods for modelling microscale flow in fibrous porous media. Phys. Fluids, 9(9):2468–2474, 1997.

[183] P. Spanne, J. F. Thovert, C. J. Jacquin, W. B. Lindquist, K. W. Jones, and P. M. Adler. Synchroton computed microtomography of porous media: topology and transports. Phys. Rev. Lett., 73:2001–2004, 1994.

[184] D. Stoyan, W. S. Kendall, and J. Mecke. Stochastic Geometry and its Applications. John Wiley & Sons, Chichester, 1995.

[185] Sauro Succi. The Lattice Boltzmann Equation. Oxford University Press, 2001.

[186] Michael C. Sukop, Haibo Huang, Chen Luh Lin, Milind D. Deo, Kyeongseok Oh, and Jan D. Miller. Distribution of multiphase fluids in porous media: Comparison between lattice Boltzmann modelling and micro-x-ray tomography. Physical Review E, 77(2):026710, 2008.

[187] Michael C Sukop and Daniel T Thorne. Lattice Boltzmann modelling: an introduction for geoscientists and engineers. Springer, 2007.

[188] M. Teubner. Level surfaces of Gaussian random fields and microemulsions. Europhys. Lett., 14:403–408, 1991.

[189] D. T. Thorne and M. C. Sukop. Lattice Boltzmann model for the Elder problem. Developments in Water Science, 55:1549–1557, 2004.

[190] S. Torquato. Bulk properties of two-phase disordered media. i. cluster expansion for the effective dielectric constant of dispersions of penetrable spheres. J. Chem. Phys., 81(11):5079–5088, 1984.

[191] S. Torquato and G. Stell. Microstructure of two-phase random media. iii. the n-point matrix probability functions for fully penetrable spheres. J. Chem. Phys., 79:1505–1510, 1983.

[192] Salvatore Torquato. Random heterogeneous media: Microstructure and improved bounds on effective properties. Appl. Mech. Rev., 44:37–76, 1991.

[193] M. Turner, L. Knüfing, C. H. Arns, A. Sakellariou, T. J. Senden, A. P. Sheppard, R. M. Sok, A. Limaye, W. V. Pinczewski, and M. A. Knackstedt. Three-dimensional imaging of multiphase flow in porous media. Physica A, 339(1-2):166–172, 2004.

[194] Olav van Genabeek and Daniel H. Rothman. Macroscopic manifestations of microscopic flows through porous media: Phenomenology from simulation. Annu. Rev. Earth Planet. Sci., 24:63–87, 1996.

[195] J. B. Walsh and W. F. Brace. The effect of pressure on porosity and the transport properties of rock. Journal of Geophysical Research: Solid Earth (1978–2012), 89(B11):9425–9431, 1984.

[196] Stuart D. C. Walsh, Holly Burwinkle, and Martin O. Saar. A new partial-bounceback lattice-Boltzmann method for fluid flow through heterogeneous media. Computers & Geosciences, 35(6):1186–1193, 2009.

[197] H. Wang and S. M. Shaler. Computer simulated three dimensional microstructure of wood fibre composite material. J. Pulp Paper Sci., 24:314–319, 1998.

[198] Xian-Huan Wen and J. Jaime Gómez-Hernández. Upscaling hydraulic conductivities in heterogeneous media: An overview. Journal of Hydrology, 183(1):ix–xxxii, 1996.

[199] Wikipedia. Root-mean-square deviation — wikipedia, the free encyclopedia, 2014. available online: http://en.wikipedia.org/w/index.php?title=Root-mean-square_deviation&oldid=597789111 (accessed on 25 March 2014).

[200] Dorthe Wildenschild and Adrian P Sheppard. X-ray imaging and analysis techniques for quantifying pore-scale structure and processes in subsurface porous medium systems. Advances in Water Resources, 51:217–246, 2013.

[201] James O. Wilkes. Fluid Mechanics for Chemical Engineers with Microfluidics and CFD. Pearson Education, 2006.

[202] P. A. Witherspoon, J. S. Y. Wang, K. Iwai, and J. E. Gale. Validity of cubic law for fluid flow in a deformable rock fracture. Water Resources Research, 16(6):1016–1024, 1980.

[203] P. Z. Wong, J. Koplik, and J. P. Tomanic. Conductivity and permeability of rocks. Phys. Rev. B, 30(11):6606–6614, 1984.

[204] S. Yanici, J. Y. Arns, Y. Cinar, W. V. Pinczewski, and C. H. Arns. Percolation effects of grain contacts in partially saturated sandstones: Deviations from archies law. Transport in porous media, 96(3):457–467, 2013.

[205] C. L. Y. Yeong and S. Torquato. Reconstructing random media. Phys. Rev. E, 57:495–506, 1998.

[206] X. Zhang, A. G. Bengough, L. K. Deeks, J. W. Crawford, and I. M. Young. A novel three-dimensional lattice boltzmann model for solute transport in variably saturated porous media. Water resources research, 38(9):6–1, 2002.

[207] L. Zhong, A. Mayer, and R. J. Glass. Visualization of surfactant-enhanced nonaqueous phase liquid mobilization and solubilization in a two-dimensional micromodel. Water Resources Research, 37(3):523–537, 2001.

[208] Jiujiang Zhu and Jingsheng Ma. An improved gray lattice Boltzmann model for simulating fluid flow in multi-scale porous media. Advances in Water Resources, 56:61–76, 2013.

[209] Donald P. Ziegler. Boundary conditions for lattice Boltzmann simulations. Journal of Statistical Physics, 71(5-6):1171–1177, 1993.

[210] B. Zinszner and C. Meynot. Visualisation des propriétés capillaires des roches réservoir. Oil & Gas Science and Technology, 37(3):337–361, 1982.

[211] Qisu Zou and Xiaoyi He. On pressure and velocity boundary conditions for the lattice Boltzmann BGK model. Physics of Fluids (1994-present), 9(6):1591–1598, 1997.